공학박사 학위논문

Phase stability of $GdBa_2Cu_3O_{7-\delta}$ and fabrication of high performance GdBCO coated conductors by RCE-DR

$GdBa_2Cu_3O_{7-\delta}$ 의 상안정성 및 RCE-DR 공정을 통한 고성능 GdBCO 초전도 선재 제조

2021년 8월

서울대학교 대학원

재료공학부

박 인 성

Phase stability of $GdBa_2Cu_3O_{7-\delta}$ and fabrication of high performance GdBCO coated conductors by RCE-DR process

$GdBa_2Cu_3O_{7-\delta}$ 의 상안정성 및 RCE-DR 공정을 통한 고성능 GdBCO 초전도 선재 제조

지도교수 유 상 임

이 논문을 공학박사학위논문으로 제출함
2021년 8월

서울대학교 대학원
재료공학부
박 인 성

박인성의 박사학위논문을 인준함
2021년 08월

위 원 장 박 찬

부 위 원 장 유 상 임

위 원 장 호 원

위 원 문 승 현

위 원 하 홍 수

Abstract

Phase stability of $GdBa_2Cu_3O_{7-\delta}$ and fabrication of high performance GdBCO coated conductors by RCE-DR

Insung Park
Department of Materials Science and Engineering
The Graduate School
Seoul National University

After the discovery of $YBa_2Cu_3O_{7-\delta}$ (YBCO) and $REBa_2Cu_3O_{7-\delta}$ (REBCO, RE: rare earth elements), which have a higher critical temperature (T_c) than liquid nitrogen (77 K) in 1987, long-length REBCO coated conductors (CCs) have been successfully fabricated by various processes such as metal-organic chemical vapor deposition (MOCVD), pulsed laser deposition (PLD), metal-organic deposition (MOD), and RCE-DR (Reactive Co-Evaporation Deposition & Reaction. Because of its high current-carrying capacity, REBCO CC is considered to be appropriate for electric power applications such as cables, fault current limiters, transformers, superconducting electromagnets, and etc..

However, further improvement of in-field J_c is still required for real applications. Among all developed processes for REBCO CCs, the RCE-DR process is regarded as the most cost-effective one because of its high growth rate and high throughput. However, in-field J_c properties of GdBCO CCs produced by RCE-DR are relatively lower than those of REBCO CCs fabricated by other processes even though it exhibits the highest self-field J_c at 77 K. To improve in-field J_c properties, in this study, the phase stability of GdBCO and fabrication of high performance GdBCO CC by the RCE-DR process have been investigated. The major results are as follows.

First, in order to obtain high performance GdBCO CCs by the RCE-DR process, it is essential to accurately determine the phase stability of GdBCO for the nominal composition of Gd:Ba:Cu = 1:1:2.5 in low oxygen pressures pressures (PO_2) of 1–150 mTorr, which has never been reported yet, since this composition has been employed for the fabrication of GdBCO CCs via the RCE-DR process. The stability boundary of GdBCO for this composition was remarkably shifted to the lower temperature regions compared with that of the nominal composition for Gd:Ba:Cu = 1:2:3. Also, it was found for this composition that with increasing temperature at a given PO_2, three-phase equilibrium among GdBCO, Gd_2CuO_4, and Cu_2O above the GdBCO phase boundary temperature first changed into two-phase equilibrium between Gd_2CuO_4 and liquid and then changed into another two-phase equilibrium between Gd_2O_3 and liquid. As a result, the stability phase diagram of GdBCO for the nominal composition of Gd: Ba: Cu = 1: 1: 2.5 in low oxygen pressures could be constructed.

Second, on the basis of the stability phase diagram of GdBCO for the nominal composition of Gd: Ba: Cu = 1: 1: 2.5, which was previously contructed, the growth regions of the c-axis aligned biaxially textured GdBCO were investigated with increasing the undercooling temperature from the upper phase boundary of GdBCO in the PO_2 region of 10 - 150 mTorr. The results reveal that the undercooling temperatures for the c-axis aligned biaxially textured GdBCO growth are less than~ 20 ºC in the PO_2 of 50, 100, and 150 mTorr. Below the PO_2 of 10 mTorr, it is impossible to grow c-axis aligned biaxially textured GdBCO film since a-axis growth occurs together with c-axis growth. To achieve c-axis aligned biaxially textured GdBCO CCs fabricated by the RCE-DR process, the growth conditions of GdBCO film should be located in the above growth region.

Finally, the superconducting GdBCO matrix of GdBCO CCs fabricated by RCE-DR normally includes somewhat large Gd_2O_3 particles with the average particle size of ~ 120 nm, which may be responsible for greatly reduced J_c values in high fields like 19 T at 4.2 K. Therefore, to improve in-field J_c properties of GdBCO CCs by RCE-DR, we tried to refine the Gd_2O_3 second phase particles trapped in the GdBCO superconducting matrix. For this purpose, the fabrication conditions of GdBCO CCs were carefully determined on the stability phase diagram of GdBCO for the nominal composition of Gd: Ba: Cu = 1: 1: 2.5 which includes the growth regions of c-axis aligned biaxially textured GdBCO film. The Gd_2O_3 particles trapped in the GdBCO superconducting matrix could be refined by controlling the growth temperature of Gd_2O_3 in the liquid phase before the c-axis aligned biaxially textured growth of GdBCO film at 850 and 860 ℃ in the PO_2 of 100 and 150 mTorr, respectively.

With decreasing the growth temperature of Gd_2O_3 from 860 to 800 °C in the PO_2 of 20 and 30 mTorr, the average particle size of Gd_2O_3 was gradually decreased from a maximum of 137 ± 52 to a minimum of 73 ± 31 nm. For the samples of GdBCO growth conditions of 860 °C in the PO_2 of 150 mTorr, with refining the average particle size of Gd_2O_3, while self-field J_c value was monotonously decreased, minimum in-field J_c values were first increased and then decreased again. Furthermore, considering the J_c-B curves of all samples, the magnetic J_c values of the samples fabricated at various temperatures in the PO_2 of 30 mTorr for Gd_2O_3 growth and 100 mTorr at 850 °C for GdBCO growth were overall higher than those fabricated under other conditions. The self-field J_c values were mainly affected in-plane and out-of-plane textures of GdBCO matrix. On the other hand, both the variation of stacking fault (SF) density and interfacial pinning by refined Gd_2O_3 particles improve the in-field J_c values and pinning properties under the magnetic field. The highest performance GdBCO CCs were obtainable from the following: transport self-field J_c at 77 K is 4.82 MA/cm^2, in-field magnetic J_c for B//c at 77 K in 1 T is 0.22 MA/cm^2, and maximum pinning force density ($F_{p,max}$) is 2.6 GN/cm^3 at 77K, 0.4 T.

Keywords: $GdBa_2Cu_3O_{7-\delta}$ films, nominal composition, phase stability, reactive co-evaporation deposition and reaction (RCE-DR), coated conductors (CCs), Gd_2O_3, refinement, flux pinning, critical current density (J_c), pinning force density (F_p)

***Student Number*: 2015-20819**

Contents

List of Tables

List of Figures

[64, 66-68, 70, 71, 87])

Fig. 2.1. The XRD patterns of as-deposited amorphous film (a) and as-quenched films after annealing at (b) 692°C and (c) 696°C in the PO_2 of 1 mTorr for 2 h, at (d) 728°C and (e) 732°C in the PO_2 of 3 mTorr for 1 h, at (f) 772°C and (g) 776°C in the PO_2 of 10 mTorr for 30min, and at (h) 800°C and (i) 804°C in the PO2 of 20 mTorr for 30min.

Fig. 2.2. FE-SEM micrographs of as-quenched films after annealing at (a) 696°C and (b) 692°C in the PO_2 of 1 mTorr for 2 h, at (c) 820°C and (d) 816°C in the PO_2 of 30 mTorr for 30 min, and at (e) 868°C and (f) 864°C in the PO_2 of 150 mTorr for 5 min.

Fig. 2.3. The XRD patterns of as-quenched films after annealing at (a) 816°C and (b) 820°C in the PO_2 of 30 mTorr for 30min, at (c) 832°C and (d) 836°C in the PO_2 of 50 mTorr for 15 min, at (e) 852°C and (f) 856°C in the PO_2 of 100 mTorr, and at (g) 864°C and (h) 868°C in the PO_2 of 150 mTorr for 5 min.

Fig. 2.4. The XRD patterns of as-quenched films after annealing at (a) 776°C, (b) 780°C, (c) 800°C, (d) 808°C, (e) 820°C, and (f) 840°C in the PO_2 of 10 mTorr for 2h.

Fig. 2.5. The XRD patterns of as-quenched films after annealing at (a) 690°C, (b) 720°C, (c) 736°C, and (d) 760°C in the PO_2 of 1 mTorr for 15h, at (e) 772°C, (f) 800°C, (g) 820°C, and (h) 840°C in the PO_2 of 10 mTorr for 3h, and at (i) 850°C, (j) 860°C, (k) 868°C, (l) 880°C, and (m) 900°C in the PO_2 of 150 mTorr for 30 min.

Fig. 2.6. (a) Z-contrast STEM micrograph of as-quenched film after annealing

Chapter 1. General Introduction

1.1. High temperature superconductor (HTS)

Superconductors have zero electrical resistance at a temperature below the critical temperature (T_c). In 1911, the first superconducting phenomenon in which the electrical resistance of mercury becomes zero at a temperature of 4.2 K of liquid helium was discovered by H. K. Onnes [1] from Leiden University, Netherlands. Subsequently, a copper oxide-based superconductor was discovered in 1986 by J. G. Bednorz and K. A. Muller [2]. Then, in 1987 M. K. Wu et al. [3] reported the discovery of $YBa_2Cu_3O_{7-\delta}$ (YBCO) with a T_c higher than the boiling point of liquid nitrogen (77 K). Therefore, high performance $REBa_2Cu_3O_{7-\delta}$ (REBCO, RE: Y and rare earth elements – La, Nd, Sm, Eu, Gd, Dy, etc. [4]) superconductors have been investigated worldwidely. Then, bismuth (Bi) copper oxide-based superconductor Bi-Sr-Ca-Cu-O (BSCCO) [5], thallium (Tl) copper oxide-based superconductor Tl-Ba-Cu-O[6], mercury (Hg) copper oxide superconductors Hg-Ba-Ca-Cu-O [7], MgB_2 superconductors [8] and iron (Fe)-based superconductors [9] have also been discovered.

The first commercialized HTS was the BSCCO superconductor, which was commercialized earlier than YBCO because it was relatively easy to manufacture wire rods using the Powder-In-Tube method, and was called the first-generation HTS. However, because BSCCO wire uses a silver (Ag) tube, the manufacturing cost is higher than that of conventional copper wire or low-

temperature superconducting Nb-Ti wire, and its in-field J_c values are seriously degraded due to its low irreversible magnetic field (H_{irr}) caused by highly two-dimensional crystal structure. Therefore, its use in devices that generate high magnetic fields is limited to 30 K or less [5, 6]. Compared to the BSCCO wire, the second-generation(2G) HTS wire, which is called Coated Conductor (CC), with higher in-field J_c values, has been developed and commercialized. Fig.1.1 shows the structure of CCs in which a REBCO superconducting layer is deposited on a polycrystalline metal substrate having an IBAD-MgO layer.

Most of the superconducting wire applications, such as power or medical devices, require high critical current (I_c) in high external magnetic fields. In particular, the 2G HTS wire is used in various applications such as superconducting cables, current limiters, large motors, generators, nuclear magnetic resonance (NMR), and superconducting magnetic energy storage (SMES) as shown in Fig.1.2 [10]. For these applications, in-field J_c value must be higher at the operating temperature below the liquid nitrogen temperature. Since the I_c characteristics under a magnetic field can be improved by introducing a secondary phase, which is a magnetic flux pinning center, in the superconductor matrix, many studies are being conducted worldwidely.

1.1.1 $GdBa_2Cu_3O_{7-\delta}$ crystal structure

One of REBCO superconductors, $GdBa_2Cu_3O_{7-\delta}$ (GdBCO) is an HTS with a $T_{c,zero}$ value of ~95 K. [11] It is also regarded as one of the 2G HTS wires because of its high in-field J_c values. [12] The GdBCO crystal structure is

shown in Fig. 1.3. GdBCO superconductor has the lattice constants of a = 3.89 Å, b = 3.89 Å, c = 11.7 Å, and has a slightly distorted orthorhombic structure. According to Mossbauer's report, Gd^{3+} ions in $GdBa_2Cu_3O_{7-\delta}$ exist independently in the rest of the crystal structure due to its strong ionic properties. [13]

The crystal structure and superconducting properties are determined by the oxygen content of the $GdBa_2Cu_3O_{7-\delta}$ superconductor. The crystal structure is changed by the oxygen arrangement of the Cu-O bond located between the two Ba-O layers, and the superconducting carrier concentration varies according to the oxygen content, and thereby determining the superconducting properties. Fig. 1.4 [14] shows the change of superconductivity according to the oxygen content. In the oxygen arrangement of the Cu-O bond, there are no oxygen atoms in the a-axis direction, and oxygen atoms exist only in the b-axis direction. In the case of insufficient oxygen, the δ value of oxygen ninstoichiometry becomes greater than 0.6, and the lengths of the b-axis and a-axis become identical, so that the CuO plane is perfectly aligned to have a tetragonal structure also superconductivity disappears. On the other hand, if δ is less than 0.6, the length of the b-axis becomes longer, an incomplete oxygen deficiency occurs in the CuO chain, an orthorhombic structure occurs, and superconductivity appears below the critical temperature. [15-19]

It is known that in the GdBCO structure, the supercurrent travels along the ab plane. [18] Therefore, the grain boundary of randomly grown GdBCO grains becomes a weak link, which greatly reduces the J_c value. Therefore, a high J_c can be obtained only by manufacturing a GdBCO thin film having a biaxial

texture in which both the a-b axis and the c-axis are well aligned. [20]

1.2. Phase stability of REBCO in low oxygen pressures

In order to understand the growth mechanism of REBCO thin films and to optimize the process conditions, it is essential to study the REBCO phase stability in low oxygen pressure since thin film fabrication processes are typically prepared in reduced oxygen pressure. Most of the phase stability studies on REBCO are on YBCO, and for other REBCO, there are a few reports on LaBCO [21], PrBCO [22], NdBCO [23], DyBCO [24], YbBCO [25], and ErBCO[25]. Many researchers have tried to identify the phase stability of YBCO such as Bormann and Nölting [26], Hammond and Bormann [27], Lay and Renlund [28], Ahn and Beyers *et al*. [29, 30], Lindemer *et al.* [31], Kim and Gaskell [32], MacManus-Driscoll *et al.* [33].

However, Lindemer *et al.* explained that it is difficult to determine the phase stability of YBCO because the control of the oxygen partial pressure is difficult due to oxygen gas emissions from the YBCO powder under high temperature and low oxygen partial pressure conditions [31]. Also, MacManus-Driscoll *et al.* reported that phase segregation occurred during the decomposition of YBCO under low oxygen partial pressure conditions, making it difficult to obtain an equilibrium phase [33].

According to reports by J. W. Lee [34], J. H. Song [35], and T. H. Seok [36], it was revealed that the phase stability and decomposition products of REBCO using an amorphous thin film as a precursor can be accurately identified even

under a low partial pressure of oxygen. Furthemore, the phase stability of GdBCO, SmBCO, and YBCO has been experimentally and precisely determined, and these stability phase diagrams are for the stoichiometric composition of RE:Ba:Cu = 1:2:3 and can be described as log P_{O_2} vs $1/T$ (K) plots, which have thermodynamic meaning. However, for several reasons, fabrication of REBCO CC typically does not use the stoichiometric composition of RE: Ba: Cu = 1:2:3 but uses the non-stoichiometric composition such as the nominal composition of RE: Ba: Cu = 1: 1: 2.5. Therefore, in order to optimize and understand the process, it is essential to identify the phase stability according to the material and composition used.

1.3. Flux pinning of REBCO coted conductors (CCs)

Type II superconductors, such as REBCO, may have a vortex state in which a superconducting state and a normal state coexist under certain magnetic field conditions ($H_{c1} < H < H_{c2}$). In the vortex state, some of the magnetic fields penetrate inside the superconductor. The penetrated magnetic field exists as a quantized magnetic flux line (vortex) (each flux line is characterized by a vortex with a diameter of ~2λ of superconducting current, surrounding a normal core with a diameter of ~2ζ), and move by the Lorentz force ($F_L = J \times B$) generated by the external magnetic field and current as shown in Fig.1.5. [37] The vortex collides with the movement of electrons forming the Cooper pair, thereby lowering the critical current characteristic, and the non-superconducting region becomes larger, eventually breaking the superconducting state. To be applied to

electrical applications, it is important to understand the characteristics of these vortices to control vortex movement so that superconducting current can flow smoothly even under high-magnetic field conditions.

1.3.1. Artificial pinning centers (APCs) in REBCO CCs

To improve the performance of REBCO CC under magnetic fields, it is necessary to introduce second phases, such as APCs, into the REBCO superconducting matrix because the improvement of pinning properties due to naturally occurring defects, such as oxygen vacancies [38], cation disorder [39], dislocation [40], low angle boundaries [41], twin boundaries [42], anti-phase boundaries [43], stacking faults (SFs) [44, 45], and etc., is limited.

One of the common classifications of the APCs relates to the dimensions and shape in the superconducting matrix as shown in Fig. 1.6. [46] Zero-dimensional APCs (0D-APCs) are defects smaller than ξ, such as vacancies and cation disorder, or atomic substitutions at RE sites. [38, 39, 47, 48] One-dimensional APCs (1D-APCs) are linear defects (dislocations obtained by substrate decoration) and columnar defects incorporated by the addition of secondary phases or obtained by heavily ion irradiation. [40, 49-56] Two-dimensional APCs (2D-APCs) are planar defects such as interfaces in multilayers, small-angle grain boundaries, antiphase boundaries, stacking faults, and surfaces of large precipitates. [41-45, 52, 57-59] Lastly, three-dimensional APCs (3D-APCs) are nanoparticles and secondary phases of the scale of ξ of more. [60-71]

The superconducting layer of the 2G HTS wire shows anisotropic J_c behavior in which the critical current values in the horizontal (B//ab) and perpendicular (B//c) direction to the superconducting layer change when exposed to an external magnetic field. One of the columnar defects, so-called nanorods which are aligned c-axis within the superconducting matrix, causes a significant enhancement of in-field J_c values for B//c. However, since the orientation of the APCs in the superconducting matrix affects the angular dependence of J_c values, the improvement in isotropic J_c behavior is more important than the improvement in anisotropic J_c behavior such as 1D-APCs. On the other hand, 3D-APCs can fix in the entire direction of the magnetic fields with spherical shape nanoparticles compared to 1D-APCs. Also, mixed 1D+3D-APCs obtained by the simultaneous combination of columnar defects and nanoparticles in the superconducting matrix could enhance the in-field J_c values with isotropic J_c enhancement. [72-75]

In addition, the dimension of APCs can depend on the fabrication process due to different growth mechanisms. For example, a BMO_3 (M: Zr, Sn, Hf, etc.) compound could be formed as nanoparticles in the MOD process but nanorods in the PLD process. For *in-situ* annealing processes such as PLD and MOCVD, the formation of APCs can be directly affected by the growth conditions of the REBCO matrix, since the nucleation and growth of REBCO superconducting matrix and APC occur simultaneously. However, since the MOD and RCE-DR processes are *ex-situ* annealing processes, random orientation structures of APCs appear because APCs are included in the superconducting matrix and thus APCs can be pre-formed in the precursor before REBCO matrix growth.

1.4. Fabrication processes of REBCO films

The currently developed REBCO film fabrication process is divided into four major categories: pulsed laser deposition (PLD) [76], metal organic deposition (MOD) [77], metal organic chemical vapor deposition (MOCVD) [78], and co-evaporation process [79, 80]. In this chaper, the fabrication processes of REBCO films are introduced in the following subsections.

1.4.1. Metal organic deposition (MOD)

As a method for depositing a superconducting layer through a metal organic deposition (MOD) process, a TFA-MOD process using a precursor solution containing metal trifluoroacetates (TFA) is common. The MOD process does not require high vacuum equipment, is applied to the reel-to-reel process to facilitate large-area deposition, and has economic advantages due to the high rate of superconducting layer deposition compared to the initial amount of raw material.

In addition, when converting REBCO in the MOD process, BaF_2 is formed as an intermediate compound because of the formation of a phase that deteriorates superconducting properties such as $BaCO_3$ due to the reactivity of BaO to H_2O and CO_2. Due to the strong reactivity of Ba, Ba is first converted to BaF_2 and then converted to REBCO. In this process, the supply of water vapor and treatment of the generated HF gas are required for the emission of F,

which limits the speed of the conversion process to improve productivity. Therefore, the key to the future depends on whether it is possible to use other precursors that can effectively control Ba without using F.

Representatively, the American Superconductor Corporation (AMSC) in the United States produces superconducting wires by the MOD process. The superconducting layer is fabricated with doping the Dy_2O_3 nanoparticle within YBCO matrix by TFA-MOD process on textured substrate via RABiTS process [81].

1.4.2. Metal-organic chemical vapor deposition (MOCVD)

The metal organic chemical vapor deposition (MOCVD) process is one of the chemical vapor deposition (CVD) methods used to fabricate single or polycrystalline thin films. This involves a very complicated process to grow a crystalline layer and can be vaporized at a low temperature using a metal-organic compound precursor, and a thin film can be deposited on a relatively large area in the reaction chamber. Currently, 2G HTS wires with excellent productivity and characteristics are fabricated, but the price is high due to the organometallic compound precursor used as raw materials.

The ratio of the metal element that becomes a thin film material in the total weight of the raw material is small (The thickness of the film actually deposited is thinner than the raw material used). There is a limit to cost reduction of the raw material precursors, and long-term storage is insufficient since the stability of the precursor is poor. However, the growth rate of the thin film is fast, the

composition can be controlled, the step coverage is good, and it has the advantages of being able to deposit without damaging the substrate or surface.

The company that produces superconducting wire by the MOCVD process is Superpower inc. of the United States, which merged with Furukawa of Japan. Super power inc. deposits (Y, Gd) BCO on the IBAD template by MOCVD process. For critical current characteristics under a magnetic field, Zr and $BaZrO_3$ (BZO) are doped to show improved performance by flux pinning [82].

1.4.3. Pulsed laser deposition (PLD)

The pulsed laser deposition (PLD) process is one of the physical vapor deposition (PVD) methods. A pulsed laser is placed intensively on the target of superconducting materials in a vacuum chamber with a focal lens to form a plume. This is a method for depositing the target material in the form of a thin film by forming a plasma of the target material, vaporizing the target material, and attaching the substrate to a heater that can control the temperature.

The PLD process is advantageous for manufacturing high-performance HTS wires, but there is a certain limit to lowering the unit cost of the wires because expensive industrial PLD equipment must be used for manufacturing HTS wires. In general, a short-wavelength KrF excimer laser (λ=248nm) is used for the superconducting thin film deposition.

A representative company using PLD is Fujikura Ltd., Japan and produces GdBCO CC on IBAD template [83], and Bruker HTS GmbH, Germany produces YBCO CC [84, 85]. SuperOx, Russia uses the PLD process as a

"Dual-Chamber PLD system" to manufacture REBCO wires [86].

1.4.4. Reactive co-evaporation deposition & reaction (RCE-DR)

The co-evaporation process is a method for depositing REBCO superconducting films by evaporating RE, Ba, and Cu raw materials together. It is possible to obtain a very fast deposition rate by evaporating the raw material, but it is difficult to adjust the deposition rate of each raw material, so it is difficult to control the exact composition of the film.

The newly developed Reactive co-evaporation deposition & reaction (RCE-DR) process evaporates metal elements through e-beam and controls the deposition rate of each material through the quartz crystal microbalance (QCM) to achieve a desired ratio [80]. It is a core technology that can form REBCO superconducting wires with excellent properties at high speed through short *ex-situ* annealing within 2 minutes after obtaining an amorphous precursor film. Since raw metal is used, it is the most efficient process to use raw materials. Currently, this technology is recognized internationally as the only technology that can reduce the price of wires below 10 US$/km·A. The schematic of RCE-DR process is shown in Fig. 1.7 [80] and 1.8.

The company using the RCE-DR process is SuNAM Co., Ltd. in Korea. The superconducting wire is fabricated by converting GdBCO amorphous precursor on IBAD-MgO substrate into a GdBCO superconducting phase by simultaneous evaporation and deposition of each raw material. Since the heat treatment time (~ 2 min) is very short, it has the advantage of being able to

fabricate superconducting wires using an inexpensive SUS substrate instead of a relatively expensive Hastelloy substrate.

However, in-field J_c properties of GdBCO CCs fabricated by RCE-DR are relatively lower than those of REBCO CCs fabricated by other processes even though it exhibits the highest self-field J_c at 77 K. As mentioned in Chapter 1.3.1, as the characteristic of the RCE-DR process, APCs occur with random orientation structures in GdBCO superconducting matrix. Gd_2O_3 particle, which is preformed before the conversion of GdBCO, could act as APCs in GdBCO CCs fabricated by RCE-DR. By the way, in order to enhance the pinning properties with 3D-APCs, there have been many efforts to optimize the amount and size of the second phase. [63-71] As shown in Fig. 1. 9 and 1. 10, the particle size seems to relate to the amount of the second phase and in-field J_c. However, the GdBCO CCs via RCE-DR normally include somewhat large Gd_2O_3 second phase particles with an average particle size and amount of ~120 nm and 33mol%, respectively. [87] In other words, it is possible to enhance the pinning properties of GdBCO CCs via RCE-DR by optimizing the size and amount of Gd_2O_3 second phase particles.

Reference

[1] H. Kamerlingh Onnes, "The resistance of pure mercury at helium temperatures," *Commun. Phys. Lab. Univ. Leiden, b,* vol. 120, 1911.

[2] J. G. Bednorz and K. A. Müller, "Possible high T c superconductivity in the Ba−La−Cu−O system," *Zeitschrift für Physik B Condensed Matter,* vol. 64, no. 2, pp. 189-193, 1986.

[3] M.-K. Wu *et al.*, "Superconductivity at 93 K in a new mixed-phase Y-Ba-Cu-O compound system at ambient pressure," *Physical review letters,* vol. 58, no. 9, p. 908, 1987.

[4] P. H. Hor *et al.*, "Superconductivity above 90 K in the square-planar compound system A $Ba_2Cu_3O_{6+x}$ with A= Y, La, Nd, Sm, Eu, Gd, Ho, Er and Lu," *Physical review letters,* vol. 58, no. 18, p. 1891, 1987.

[5] H. Maeda, Y. Tanaka, M. Fukutomi, and T. Asano, "A new high-Tc oxide superconductor without a rare earth element," *Japanese Journal of Applied Physics,* vol. 27, no. 2A, p. L209, 1988.

[6] Z. Sheng *et al.*, "Superconductivity at 90 K in the Tl-Ba-Cu-O system," *Physical review letters,* vol. 60, no. 10, p. 937, 1988.

[7] A. Schilling, M. Cantoni, J. Guo, and H. Ott, "Superconductivity above 130 k in the hg–ba–ca–cu–o system," *Nature,* vol. 363, no. 6424, pp. 56-58, 1993.

[8] J. Nagamatsu, N. Nakagawa, T. Muranaka, Y. Zenitani, and J. Akimitsu, "Superconductivity at 39 K in magnesium diboride," *nature,* vol. 410, no. 6824, pp. 63-64, 2001.

[9] Y. Kamihara, T. Watanabe, M. Hirano, and H. Hosono, "Iron-based layered superconductor La $[O_{1-x} F_x]$ FeAs (x= 0.05− 0.12) with T_c= 26 K," *Journal of the American Chemical Society,* vol. 130, no. 11, pp. 3296-3297, 2008.

[10] Fujikura. "http://www.fujikura.com/solutions/superconductingwire."

[11] M. Murakami, N. Sakai, T. Higuchi, and S. Yoo, "Melt-processed light rare earth element-Ba-Cu-O," *Superconductor Science and Technology,* vol. 9, no. 12, p. 1015, 1996.

[12] C. Chu, "Superconductivity above 90 K," *Proceedings of the National Academy of Sciences of the United States of America,* vol. 84, no. 14, p. 4681, 1987.

[13] E. Alp *et al.*, "Magnetic isolation of Gd in superconducting $GdBa_2Cu_3O_{7-\delta}$," *Physical Review B,* vol. 36, no. 16, p. 8910, 1987.

[14] J. Rossat-Mignod, L. Regnault, C. Vettier, P. Burlet, J. Henry, and G. Lapertot, "Investigation of the spin dynamics in $YBa_2Cu_3O_{6+x}$ by inelastic neutron scattering," *Physica B: Condensed Matter,* vol. 169, no. 1-4, pp. 58-65, 1991.

[15] J. Sakai and S. Imai, "Evaluation of oxygen content in perovskite-type manganite/YBCO bilayered films," *Physica C: Superconductivity,* vol. 392, pp. 1342-1345, 2003.

[16] J. Routbort and S. Rothman, "Oxygen diffusion in cuprate superconductors," *Journal of applied physics,* vol. 76, no. 10, pp. 5615-5628, 1994.

[17] E. Lee *et al.*, "Raman scattering studies of $YBa_2Cu_3O_{7-x}$ thin films grown by chemical vapor deposition and metal-organic deposition," *Physica C: Superconductivity and its applications,* vol. 463, pp. 732-735, 2007.

[18] D. Thiery *et al.*, "Crystal structure of aluminium containing superconducting oxides: single crystal study of $GdBa_2Cu_{3-x}$ ALxO6.88 (x= 0.28) and $ErBa_2Cu_3$−yAl$_y$O$_{6.6}$ (y= 0.14)," *Zeitschrift für Physik B Condensed Matter,* vol. 80, no. 2, pp. 177-180, 1990.

[19] A. G. S. a. C. E. Housecroft, (Inorganic chemistry). 2005.

[20] E. M. Gyorgy, R. Van Dover, K. Jackson, L. Schneemeyer, and J. V. Waszczak, "Anisotropic critical currents in $Ba_2YCu_3O_7$ analyzed using

an extended Bean model," *Applied physics letters,* vol. 55, no. 3, pp. 283-285, 1989.

[21] T. Lindemer, E. Specht, C. MacDougall, G. Taylor, and S. Pye, "Nonstoichiometry and decomposition of $La_{1+z}Ba_{2-z}Cu_3O_y$ and $La_4BaCu_5O_{13-w}$," *Physica C: Superconductivity,* vol. 216, no. 1-2, pp. 99-110, 1993.

[22] T. Lindemer and E. Specht, "Nonstoichiometry and decomposition of $Pr_{1+z}Ba_{2-z}Cu_3O_y$ and comparison with Y123, La123 and Nd123," *Physica C: Superconductivity,* vol. 268, no. 3-4, pp. 271-278, 1996.

[23] T. Lindemer, E. Specht, P. Martin, and M. Flitcroft, "Nonstoichiometry, decomposition and T_c of $Nd_{1+z}Ba_{2-z}Cu_3O_y$," *Physica C: Superconductivity,* vol. 255, no. 1-2, pp. 65-75, 1995.

[24] H. Ishizuka, Y. Idemoto, and K. Fueki, "Oxygen nonstoichiometry and high-temperature conductivity of $DyBa_2Cu_3O_{7-\delta}$," *Physica C: Superconductivity,* vol. 195, no. 1-2, pp. 145-156, 1992.

[25] J. Nelstrop and J. MacManus-Driscoll, "Phase stability of erbium barium cuprate, $ErBa_2Cu_3O_{7-x}$ and ytterbium barium cuprate, $YbBa_2Cu_3O_{7-x}$," *Physica C: Superconductivity,* vol. 377, no. 4, pp. 585-594, 2002.

[26] R. Bormann and J. Nölting, "Stability limits of the perovskite structure in the Y-Ba-Cu-O system," *Applied physics letters,* vol. 54, no. 21, pp. 2148-2150, 1989.

[27] R. Hammond and R. Bormann, "Correlation between the in situ growth conditions of YBCO thin films and the thermodynamic stability criteria," *Physica C: Superconductivity and its Applications,* vol. 162, pp. 703-704, 1989.

[28] K. W. Lay and G. M. Renlund, "Oxygen pressure effect on the Y_2O_3—BaO—CuO liquidus," *Journal of the American Ceramic Society,* vol. 73, no. 5, pp. 1208-1213, 1990.

[29] B. T. Ahn, V. Lee, R. Beyers, T. Gür, and R. Huggins, "Quaternary

phase relations near $YBa_2Cu_3O_{6+x}$ at 850° C in reduced oxygen pressures," *Physica C: Superconductivity,* vol. 167, no. 5-6, pp. 529-537, 1990.

[30] R. Beyers and B. Alm, "Thermodynamic considerations in superconducting oxides," *Annual Review of Materials Science,* vol. 21, no. 1, pp. 335-372, 1991.

[31] T. Lindemer, F. Washburn, C. MacDougall, R. Feenstra, and O. Cavin, "Decomposition of $YBa_2Cu_3O_{7-x}$ and $YBa_2Cu_4O_8$ for $PO_2 \leq 0.1$ MPa," *Physica C: Superconductivity,* vol. 178, no. 1-3, pp. 93-104, 1991.

[32] J. S. Kim and D. R. Gaskell, "Stability Diagram for the system $YBa_2Cu_3O_{7-x}$," *Journal of the American Ceramic Society,* vol. 77, no. 3, pp. 753-758, 1994.

[33] J. MacManus-Driscoll, J. Bravman, and R. Beyers, "Phase equilibria in the YBaCuO system and melt processing of Ag clad $Y_1Ba_2Cu_3O_{7-x}$ tapes at reduced oxygen partial pressures," *Physica C: Superconductivity,* vol. 241, no. 3-4, pp. 401-413, 1995.

[34] J.-W. Lee, S.-M. Choi, J.-H. Song, J.-H. Lee, S.-H. Moon, and S.-I. Yoo, "Stability phase diagram of $GdBa_2Cu_3O_{7-\delta}$ in low oxygen pressures," *Journal of Alloys and Compounds,* vol. 602, pp. 78-86, 2014.

[35] J.-h. Song, "Phase stability and flux pinning control of $SmBa_2Cu_3O_{7-\delta}$ superconducting thin films," Seoul national university, 2014.

[36] T.-H. Seok, I. Park, and S.-I. Yoo, "Stability diagram of $YBa_2Cu_3O_{7-\delta}$ in low oxygen pressures," *IEEE Transactions on Applied Superconductivity,* vol. 27, no. 4, pp. 1-5, 2016.

[37] H. Yamasaki, K. Ohki, H. Yamada, K. Develos-Bagarinao, Y. Nakagawa, and Y. Mawatari, "Flux-pinning mechanisms in high current density superconducting $YBa_2Cu_3O_7$ films," *Transactions of the Materials Research Society of Japan,* vol. 20, pp. 77-83, 2012.

[38] T. Hylton and M. Beasley, "Flux-pinning mechanisms in thin films of $YBa_2Cu_3O_x$," *Physical Review B,* vol. 41, no. 16, p. 11669, 1990.

[39] V. Maroni, Y. Li, D. Feldmann, and Q. Jia, "Correlation between cation disorder and flux pinning in the $YBa_2Cu_3O_7$ coated conductor," *Journal of Applied Physics,* vol. 102, no. 11, p. 113909, 2007.

[40] B. Dam *et al.*, "Origin of high critical currents in $YBa_2Cu_3O_{7-\delta}$ superconducting thin films," *Nature,* vol. 399, no. 6735, p. 439, 1999.

[41] D. Agassi, D. Christen, and S. Pennycook, "Flux pinning and critical currents at low-angle grain boundaries in high-temperature superconductors," *Applied physics letters,* vol. 81, no. 15, pp. 2803-2805, 2002.

[42] B. Roas, L. Schultz, and G. Saemann-Ischenko, "Anisotropy of the critical current density in epitaxial $YBa_2Cu_3O_x$ films," *Physical review letters,* vol. 64, no. 4, p. 479, 1990.

[43] C. Jooss, R. Warthmann, and H. Kronmüller, "Pinning mechanism of vortices at antiphase boundaries in $YBa_2Cu_3O_{7-\delta}$," *Physical Review B,* vol. 61, no. 18, p. 12433, 2000.

[44] M. Kramer, "Processing controlled stacking faults in $YBa_2Cu_3O_{7-\delta}$ and their effect on flux pinning," *Applied physics letters,* vol. 58, no. 10, pp. 1086-1088, 1991.

[45] Y. Jia *et al.*, "Microstructure dependence of the c-axis critical current density in second-generation YBCO tapes," *Journal of Applied Physics,* vol. 110, no. 8, p. 083923, 2011.

[46] K. Matsumoto and P. Mele, "Artificial pinning center technology to enhance vortex pinning in YBCO coated conductors," *Superconductor Science and Technology,* vol. 23, no. 1, p. 014001, 2009.

[47] M. Daeumling, J. Seuntjens, and D. Larbalestier, "Oxygen-defect flux pinning, anomalous magnetization and intra-grain granularity in $YBa_2Cu_3O_{7-\delta}$," *Nature,* vol. 346, no. 6282, p. 332, 1990.

[48] S. Foltyn *et al.*, "Materials science challenges for high-temperature superconducting wire," *Nature materials,* vol. 6, no. 9, p. 631, 2007.

[49] R. Schalk, K. Kundzins, H. Weber, E. Stangl, S. Proyer, and D. Bäuerle,

"STM observation of dislocation chains suitable for flux pinning in $YBa_2Cu_3O_{7-x}$ films," *Physica C: Superconductivity and its applications,* vol. 257, no. 3-4, pp. 341-354, 1996.

[50] F. Klaassen, G. Doornbos, J. Huijbregtse, R. Van der Geest, B. Dam, and R. Griessen, "Vortex pinning by natural linear defects in thin films of $YBa_2Cu_3O_{7-\delta}$," *Physical Review B,* vol. 64, no. 18, p. 184523, 2001.

[51] J. Huijbregtse *et al.*, "Vortex pinning by natural defects in thin films of $YBa_2Cu_3O_{7-\delta}$," *Superconductor Science and Technology,* vol. 15, no. 3, p. 395, 2002.

[52] V. Pan *et al.*, "Supercurrent transport in $YBa_2Cu_3O_{7-\delta}$ epitaxial thin films in a dc magnetic field," *Physical review B,* vol. 73, no. 5, p. 054508, 2006.

[53] L. Civale, "Vortex pinning and creep in high-temperature superconductors with columnar defects," *Superconductor Science and Technology,* vol. 10, no. 7A, p. A11, 1997.

[54] J. MacManus-Driscoll *et al.*, "Strongly enhanced current densities in superconducting coated conductors of $YBa_2Cu_3O_{7-x}$+$BaZrO_3$," *Nature materials,* vol. 3, no. 7, p. 439, 2004.

[55] A. Xu *et al.*, "Strongly enhanced vortex pinning from 4 to 77 K in magnetic fields up to 31 T in 15 mol.% Zr-added (Gd,Y)-Ba-Cu-O superconducting tapes," *Apl Materials,* vol. 2, no. 4, p. 046111, 2014.

[56] S. Miura, Y. Yoshida, Y. Ichino, K. Matsumoto, A. Ichinose, and S. Awaji, "Characteristics of high-performance $BaHfO_3$-doped $SmBa_2Cu_3O_y$ superconducting films fabricated with a seed layer and low-temperature growth," *Superconductor Science and Technology,* vol. 28, no. 6, p. 065013, 2015.

[57] W. Kwok, U. Welp, G. Crabtree, K. Vandervoort, R. Hulscher, and J. Liu, "Direct observation of dissipative flux motion and pinning by twin boundaries in $YBa_2Cu_3O_{7-\delta}$ single crystals," *Physical review letters,* vol. 64, no. 8, p. 966, 1990.

[58] E. Talantsev, N. Strickland, S. Wimbush, J. Storey, J. Tallon, and N. Long, "Hole doping dependence of critical current density in $YBa_2Cu_3O_{7-\delta}$ conductors," *Applied Physics Letters,* vol. 104, no. 24, p. 242601, 2014.

[59] A. Puichaud, S. Wimbush, and R. Knibbe, "Enhanced low-temperature critical current by reduction of stacking faults in REBCO coated conductors," *Superconductor Science and Technology,* vol. 30, no. 7, p. 074005, 2017.

[60] A. Llordes *et al.*, "Nanoscale strain-induced pair suppression as a vortex-pinning mechanism in high-temperature superconductors," *Nature materials,* vol. 11, no. 4, p. 329, 2012.

[61] P. Mele *et al.*, "High pinning performance of $YBa_2Cu_3O_{7-x}$ films added with Y_2O_3 nanoparticulate defects," *Superconductor Science and Technology,* vol. 28, no. 2, p. 024002, 2014.

[62] M. Miura *et al.*, "Tuning nanoparticle size for enhanced functionality in perovskite thin films deposited by metal organic deposition," *NPG Asia Materials,* vol. 9, no. 11, p. e447, 2017.

[63] W. Zhang *et al.*, "Control of flux pinning in MOD YBCO coated conductor," *IEEE transactions on applied superconductivity,* vol. 17, no. 2, pp. 3347-3350, 2007.

[64] Y. Yoshida *et al.*, "Controlled nanoparticulate flux pinning structures in $RE_{1+x}Ba_{2-x}Cu_3O_y$ films," *Physica C: Superconductivity and its applications,* vol. 445, pp. 637-642, 2006.

[65] X. Obradors *et al.*, "Epitaxial $YBa_2Cu_3O_{7-x}$ nanocomposite films and coated conductors from $BaMO_3$ (M= Zr, Hf) colloidal solutions," *Superconductor Science and Technology,* vol. 31, no. 4, p. 044001, 2018.

[66] P. Mele *et al.*, "Insertion of nanoparticulate artificial pinning centres in $YBa_2Cu_3O_{7-x}$ films by laser ablation of a Y_2O_3-surface modified target," *Superconductor Science and Technology,* vol. 20, no. 7, p. 616,

2007.

[67] N. Long *et al.*, "Enhanced in-field critical currents of YBCO second-generation (2G) wire by Dy additions," *Superconductor Science and Technology,* vol. 18, no. 12, p. S405, 2005.

[68] L. Lei, G. Zhao, H. Xu, N. Wu, and Y. Chen, "Influences of Y_2O_3 nanoparticle additions on the microstructure and superconductivity of YBCO films derived from low-fluorine solution," *Materials Chemistry and Physics,* vol. 127, no. 1-2, pp. 91-94, 2011.

[69] M. Z. Khan *et al.*, "Improving the flux pinning with artificial BCO nanodots and correlated dislocations in YBCO films grown on IBAD-MgO based template," *IEEE Transactions on Applied Superconductivity,* vol. 29, no. 5, pp. 1-5, 2019.

[70] J. Gutierrez *et al.*, "Strong isotropic flux pinning in solution-derived $YBa_2Cu_3O_{7-x}$ nanocomposite superconductor films," *Nature materials,* vol. 6, no. 5, pp. 367-373, 2007.

[71] X. Cui, B. Tao, Z. Tian, J. Xiong, X. Zhang, and Y. Li, "Enhancement of flux pinning of TFA-MOD YBCO thin films by embedded nanoscale Y_2O_3," *Superconductor Science and Technology,* vol. 19, no. 8, p. 844, 2006.

[72] H. Zhou *et al.*, "Thickness dependence of critical current density in $YBa_2Cu_3O_{7-\delta}$ films with $BaZrO_3$ and Y_2O_3 addition," *Superconductor Science and Technology,* vol. 22, no. 8, p. 085013, 2009.

[73] P. Mele *et al.*, "Incorporation of double artificial pinning centers in $YBa_2Cu_3O_{7-d}$ films," *Superconductor Science and Technology,* vol. 21, no. 1, p. 015019, 2007.

[74] A. K. Jha *et al.*, "Tailoring the vortex pinning strength of YBCO thin films by systematic incorporation of hybrid artificial pinning centers," *Superconductor Science and Technology,* vol. 28, no. 11, p. 114004, 2015.

[75] T. Horide *et al.*, "J_c improvement by double artificial pinning centers

of $BaSnO_3$ nanorods and Y_2O_3 nanoparticles in $YBa_2Cu_3O_7$ coated conductors," *Superconductor Science and Technology,* vol. 26, no. 7, p. 075019, 2013.

[76] H. Kutami *et al.*, "Progress in research and development on long length coated conductors in Fujikura," *Physica C: Superconductivity,* vol. 469, no. 15-20, pp. 1290-1293, 2009.

[77] M. W. Rupich *et al.*, "Advances in second generation high temperature superconducting wire manufacturing and R&D at American Superconductor Corporation," *Superconductor Science and Technology,* vol. 23, no. 1, p. 014015, 2009.

[78] V. Selvamanickam *et al.*, "High performance 2G wires: From R&D to pilot-scale manufacturing," *IEEE transactions on applied superconductivity,* vol. 19, no. 3, pp. 3225-3230, 2009.

[79] H. Ha *et al.*, "Critical current density of SmBCO coated conductor on IBAD-MgO substrate fabricated by co-evaporation," *Physica C: Superconductivity and its applications,* vol. 463, pp. 493-496, 2007.

[80] J.-H. Lee, H. Lee, J.-W. Lee, S.-M. Choi, S.-I. Yoo, and S.-H. Moon, "RCE-DR, a novel process for coated conductor fabrication with high performance," *Superconductor Science and Technology,* vol. 27, no. 4, p. 044018, 2014.

[81] M. W. Rupich *et al.*, "Second generation wire development at AMSC," *IEEE transactions on applied superconductivity,* vol. 23, no. 3, pp. 6601205-6601205, 2012.

[82] T. Aytug *et al.*, "Enhanced flux pinning in MOCVD-YBCO films through Zr additions: systematic feasibility studies," *Superconductor Science and Technology,* vol. 23, no. 1, p. 014005, 2009.

[83] M. Igarashi *et al.*, "Remarkable progress in fabricating RE123 coated conductors by IBAD/PLD technique at Fujikura," in *Journal of Physics: Conference Series*, 2010, vol. 234, no. 2: IOP Publishing, p. 022016.

[84] A. Usoskin *et al.*, "Large-area HTS-coated stainless steel tapes with

high critical currents," *IEEE transactions on applied superconductivity,* vol. 11, no. 1, pp. 3385-3388, 2001.

[85] A. Usoskin *et al.*, "Processing of long-length YBCO coated conductors based on stainless steel tapes," *IEEE transactions on applied superconductivity,* vol. 17, no. 2, pp. 3235-3238, 2007.

[86] S. Lee *et al.*, "Development and production of second generation high Tc superconducting tapes at SuperOx and first tests of model cables," *Superconductor Science and Technology,* vol. 27, no. 4, p. 044022, 2014.

[87] S.-M. Choi *et al.*, "Characteristics of high-J_c GdBCO coated conductors fabricated by the RCE-DR process," *IEEE transactions on applied superconductivity,* vol. 23, no. 3, pp. 8001004-8001004, 2012.

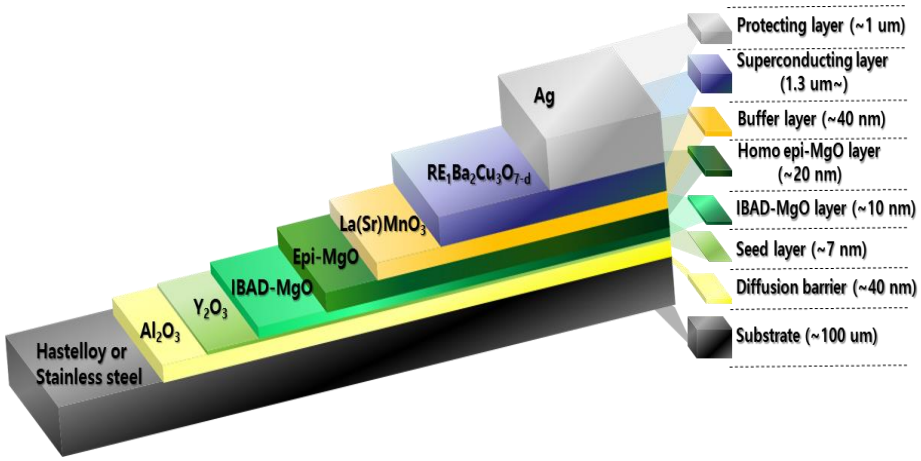

Fig.1.1 A schematic of the architecture for REBCO CCs by RCE-DR

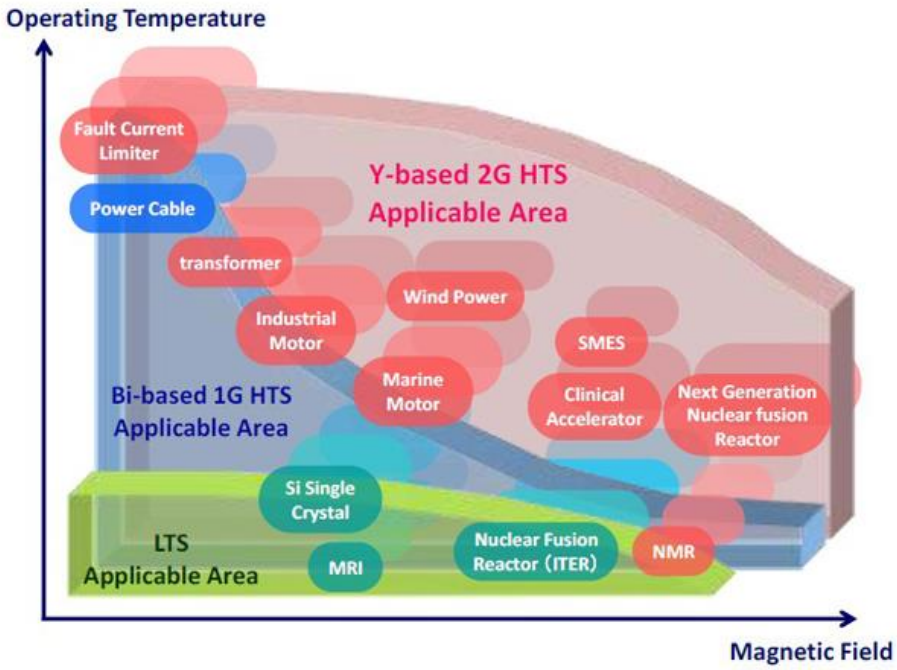

Fig.1.2 Electric applications of superconducting materials as a function of magnetic field [10].

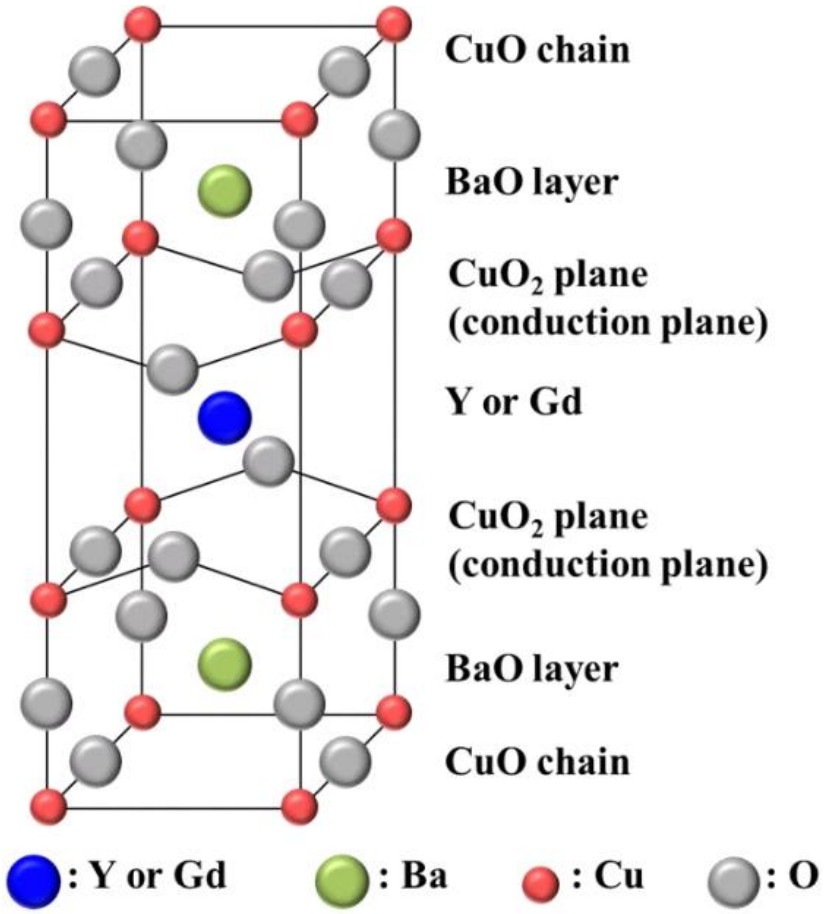

Fig.1.3. Crystallographic structure of YBCO and REBCO (RE = rare earth elements)

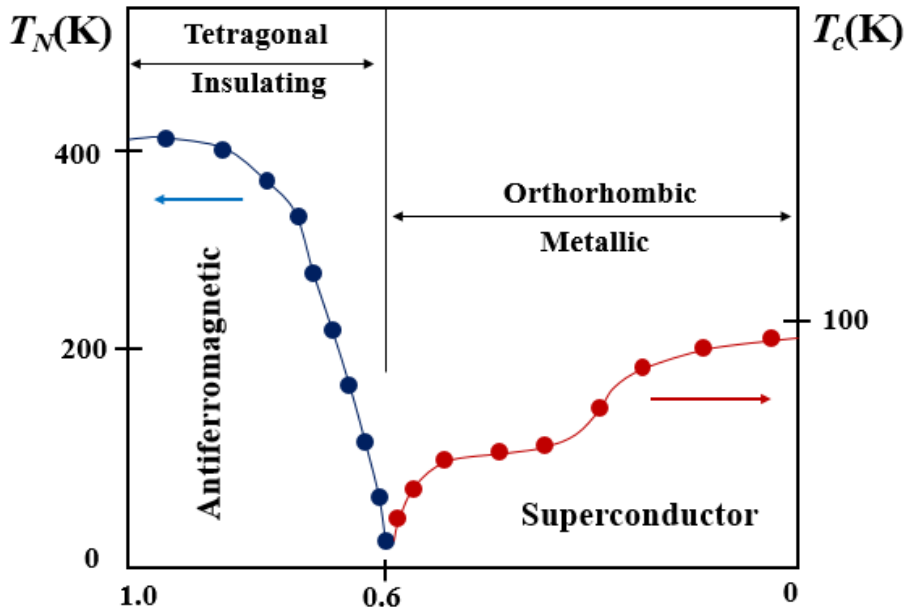

Fig.1.4. Changes in characteristics for δ $REBa_2Cu_3O_{7-\delta}$ superconductor (Data from ref. [14])

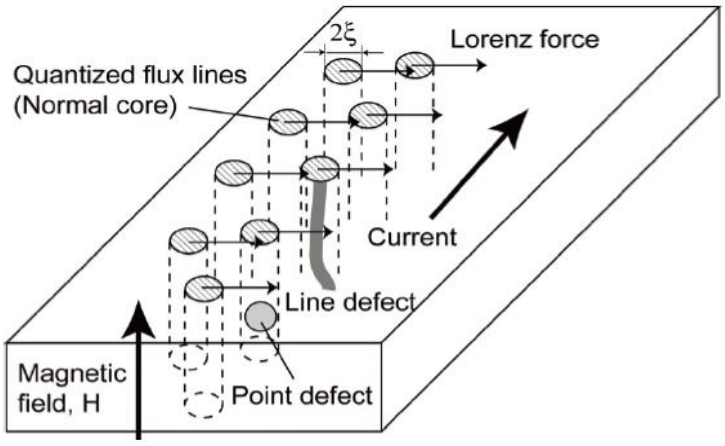

Fig. 1.5. A schematic of quantized flux lines and flux pinning. [37]

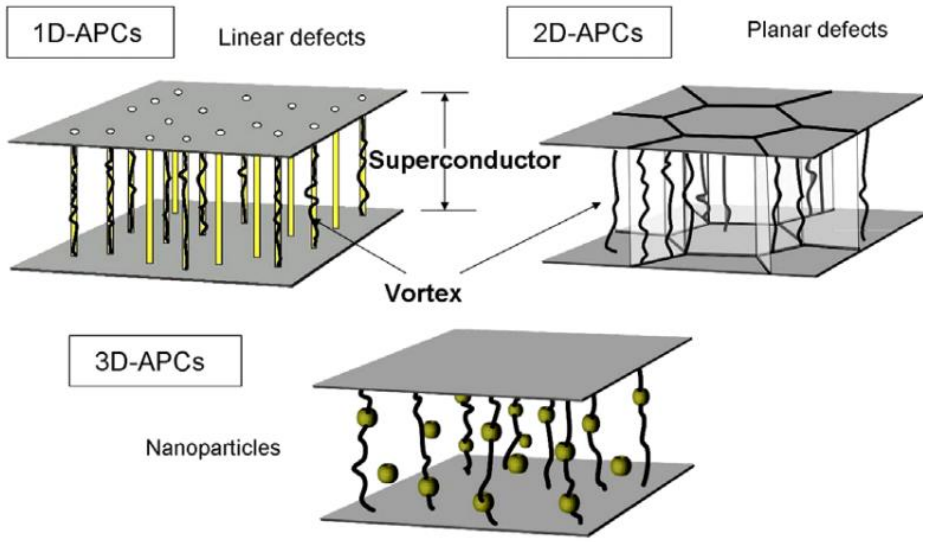

Fig. 1.6. A schematic of the dimensionality of artificial pinning centers (APCs). [46]

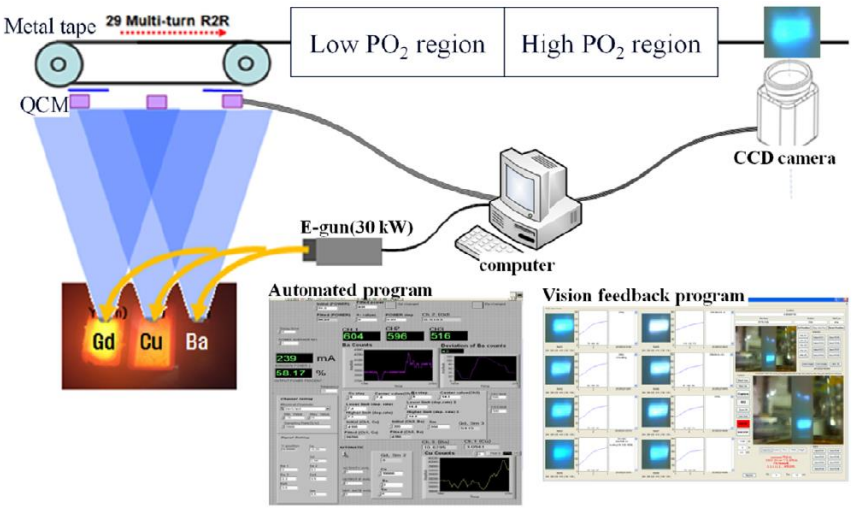

Fig. 1.7. A schematic of the RCE-DR process and the program of the automated deposition control. [80]

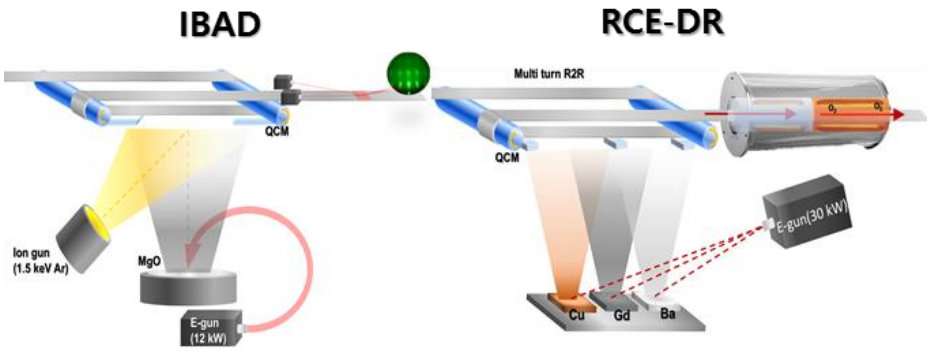

Fig. 1.8. A schematic of the IBAD and RCE-DR process.

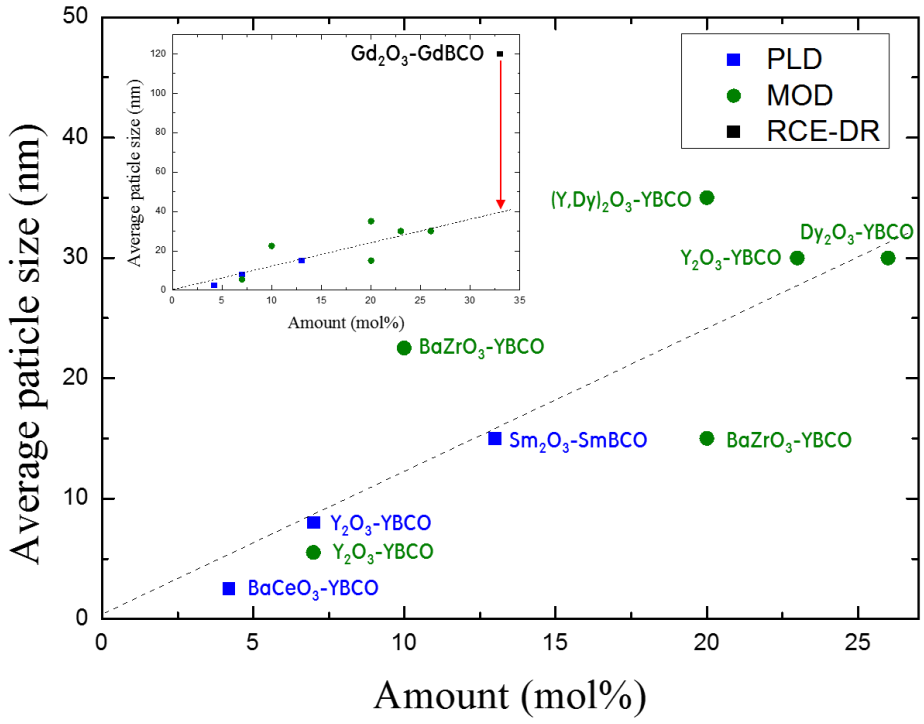

Fig. 1.9. Summarization of previous reports on optimized second phase particle size and amount. (Data from ref. [63-71])

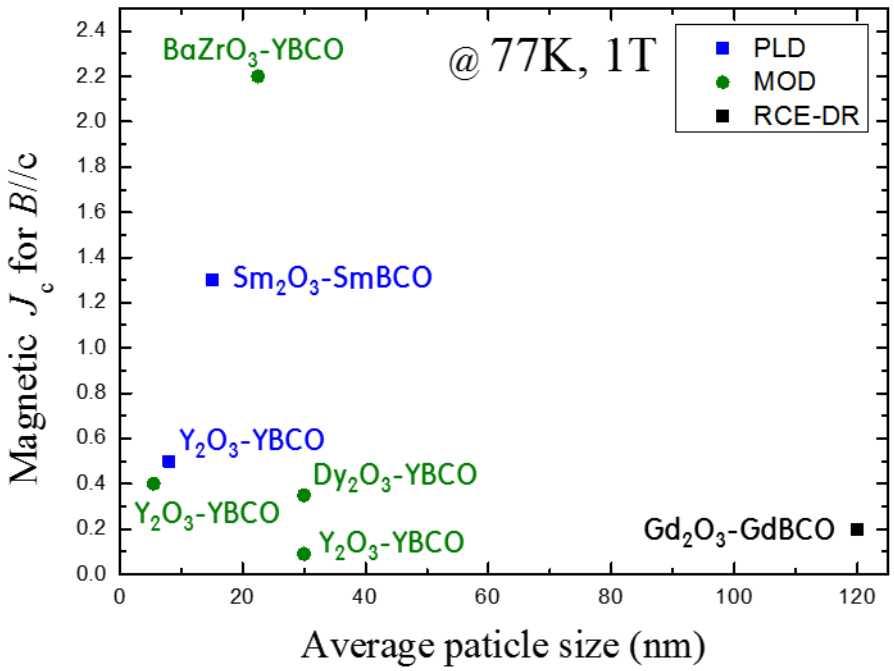

Fig. 1.10. The plot of magnetic J_c versus average particle size from previous reports for optimized second phase particle size and amount. (Data from ref [64, 66-68, 70, 71, 87])

Chapter 2. Stability phase diagram of $GdBa_2Cu_3O_{7-\delta}$ for the nominal composition of Gd:Ba:Cu=1:1:2.5 in low oxygen pressures

2.1. Introduction

Since REBCO films have been fabricated in a reduced oxygen atmosphere, the phase stability of REBCO in low oxygen pressures plays a key role of the basic guideline for optimizing the processing parameters in various fabrication methods. We have recently reported the stability phase diagram of $GdBa_2Cu_3O_{7-\delta}$ (GdBCO) [1] of which the cation ratio is Gd:Ba:Cu = 1:2:3 in low oxygen pressures. In order to obtain high performance GdBCO CCs by the RCE-DR process, however, it is essential to accurately determine the phase stability of GdBCO for the nominal composition of Gd:Ba:Cu = 1:1:2.5 in low oxygen pressures, which has never reported yet, since this composition has been employed for the fabrication of GdBCO CCs via the RCE-DR process [2]. Information on the phase stability of GdBCO is essential not only for optimizing the processing parameters of the RCE-DR process but also for understanding the growth mechanism of the GdBCO film.

In our previous paper [1], we reported that using the amorphous precursor film was appropriate for the determination of the phase stability diagram of GdBCO in low oxygen pressures ranging from 1 to 150 mTorr for the nominal

composition of Gd:Ba:Cu = 1:2:3. Likewise, for the nominal composition of Gd:Ba:Cu = 1:1:2.5, using amorphous precursor films on $LaAlO_3$ (LAO) (001) substrates, we tried to accurately determine the phase stability diagram of GdBCO and stable phases in low oxygen pressures ranging from 1 to 150 mTorr in this study.

2.2. Experimental

Gd-Ba-Cu-O amorphous precursor films were deposited on the LAO single crystal substrates by Nd: YAG (λ = 355 nm) PLD. The GdBCO target for PLD was prepared by conventional solid state reaction using Gd_2O_3 (High Purity Co., 99.9%), $BaCO_3$ (High Purity Co., 99.95%), and CuO (High Purity Co., 99.9%) as the starting materials. The precursor powders were weighed to have the nominal composition of Gd:Ba:Cu = 1:1:2.5, ball-milled for 24 h, and calcined four times at 880°C for 12 h in air with an intermediate grinding. As-calcined powder was pressed into 1 inch-diameter pellet and consolidated further by CIP (cold-isostatic press) with 2 ton/cm^2. As-pressed powder was sintered at 940°C for 12 h in air. To prepare amorphous precursor films for the nominal composition of Gd:Ba:Cu = 1:1:2.5, the PLD conditions of substrate temperature, working oxygen pressure, energy density, laser frequency, and target-to-substrate distance were 200°C, 400 mTorr, 2 J/cm^2, 5 Hz, and 6 cm, respectively.

To determine the phase stability of GdBCO, the amorphous precursor films were annealed at various high temperatures in the PO_2 regime ranging from 1

to 150 mTorr, and then rapidly cooled by using the reel-to-reel tube furnace. Details of the reel-to-reel tube furnace and heat treatment path for the determination of the phase boundary of GdBCO and stable phases are described in our previous reports [1, 3]. As it was mentioned in our previous report [3], a prolonged annealing period was required in relatively lower PO_2 to obtain equilibrium phases. Since we should concern about a chemical reaction between substrate and liquid phase due to prolonged annealing, it was necessary to experimentally determine the annealing time appropriate for each PO_2.

X-ray diffraction (XRD) (Bruker, D8-Advance) was performed for the phase analysis of samples, and microstructures were observed by using a field emission scanning electron microscope (FE-SEM) (ZEISS, MERLIN Compact). In addition, an analytical transmission electron microscope (TEM, JEOL, JEM-2100F) was employed to analyze the cross-sectional microstructures of samples.

2.3. Results and discussion

2.3.1. $GdBa_2Cu_3O_{7-\delta}$ phase boundaries in the PO_2 region of 1–150 mTorr

Fig. 2. 1 shows the XRD patterns of samples annealed below and above the GdBCO phase boundary in the PO_2 regime ranging from 1 to 20 mTorr. As shown in Fig. 1(a), since there are only two peaks of the LAO substrate, it is clear that as-deposited film is amorphous. Figs. 1(b)–(i) represent the XRD

patterns of as-quenched films after annealing at 692–800°C. The annealing time was 2 h for 1 mTorr, 1 h for 3 mTorr, 30min for 10 and 20 mTorr. The peaks of GdBCO (00*l*) disappear at 696°C compared with GdBCO (00*l*) peaks at 692°C in the PO_2 of 1 mTorr as shown in Figs. 1 (b) and (c). An obvious difference in the surface morphology between 692°C and 696°C can also be observed in Figs. 2 (a) and (b). Therefore, the GdBCO stability boundary is surely located at 694 ± 2°C for PO_2 of 1 mTorr. Similarly, referring to Figs. 1(d)-(i) and Figs. 2(c)-(d), it is obvious that each GdBCO boundary points for PO_2 of 3 mTorr, 10 mTorr, and 20 mTorr are located at 730 ± 2°C, 774 ± 2°C, and 802 ± 2°C, respectively. Figs. 3 (a)–(h) represent the XRD patterns of as-quenched films after annealing at 816–868°C in the PO_2 regime ranging from 30 to 150 mTorr for 30min (30 mTorr), 15 min (50 mTorr), and 5min (100, 150 mTorr). It can be seen that the GdBCO boundary points for PO_2 of 30 mTorr, 50 mTorr, 100 mTorr, and 150 mTorr are located at 818 ± 2°C, 834 ± 2°C, 854 ± 2°C, and 866 ± 2°C, respectively.

According to the XRD patterns in Fig. 2. 1 and Fig. 2. 3, Gd_2O_3, Cu_2O, $BaCuO_2$, and $BaCu_2O_2$ phases are observed both below and above the GdBCO phase boundary. Assuming that the ternary eutectic point in the Gd_2O_2-BaO-CuO ternary system is located at the position similar to that in the Y_2O_3-BaO-CuO system [1, 4], the $BaCu_2O_2$ and $BaCuO_2$ phases are considered as by-products solidified from the ternary liquid phase during rapid cooling. A wavy surface morphology shown in the FE-SEM micrographs of Figs. 2 (a), (c), and (d) above the GdBCO phase stability boundary is believed to represent the rapidly solidified region of the liquid phase existed at the annealing

temperatures before rapid cooling.

2.3.2. Stable equilibria phases above and below the $GdBa_2Cu_3O_{7-\delta}$ stability line

According to the stability phase diagram of GdBCO for the nominal composition of Gd: Ba: Cu = 1:2:3 [1], three phases of Gd_2O_3 + $GdBa_6Cu_3O$ (Gd163) + L_2 are in equilibrium below the PO_2 regime of ~ 13 mTorr. To identify the stable phases above the stability line of GdBCO for the nominal composition of Gd:Ba:Cu = 1:1:2.5, precursor films were annealed at 776–840°C in the PO_2 of 10 mTorr for 2 h by the following heat treatment path in the reel-to-reel tube furnace. At a given annealing temperature, the amorphous precursor was first moved to the furnace zone in the PO_2 of ~$1x10^{-5}$ Torr and held for 5 min, subsequently moved to the furnace zone in the PO_2 of 10 mTorr and held for 2 h, and finally moved back to come out of the tube furnace for rapid cooling. Fig. 2. 4 shows the XRD patterns of as-quenched films after annealing, and red-dotted line is the (105) main peak position of the Gd163 phase. As shown in Fig. 2. 4, the Gd163 phase seems to exist in the XRD patterns of Figs. 4 (e) and (f). If the Gd163 phase is really stable one, it must also be detected in Figs. 4 (a) and (b) since the region is just above the GdBCO phase boundary. However, it is undetectable. Therefore, the peak matched with red-dotted line in Figs. 4 (e) and (f) is considered to originate from unknown phase due to the chemical reaction between the liquid phase and the substrate.

On the other hand, to determine the stable phases below the phase boundary

of GdBCO, we tried to anneal amorphous precursor films and rapidly cool them in a given PO_2 by following heat treatment path. In a given PO_2, the amorphous precursor film was moved to the furnace zone of an aimed annealing temperature and finally moved back to come out of the tube furnace for rapid cooling. Fig. 2. 5 shows the XRD patterns of as-quenched samples after annealing at the temperature region of 690–760°C in PO_2 of 1 mTorr for 15 h, 772–840°C in PO_2 of 10 mTorr for 3 h, and 850–900°C in PO_2 of 150 mTorr for 30 min. In Figs. 5 (e), (f), (i), (j), and (k), the (103) peak of the Gd_2CuO_4 phase located at the red-dotted line are observable, and the (400) peak of the Gd_2O_3 phase located at the blue-dotted line are observable in Figs. 5 (c), (d), (g), (h), (l), and (m) from as-quenched samples. From the XRD patterns of as-quenched samples annealed at various temperatures in PO_2 of 1, 3, 10, 30, and 150 mTorr (not presented here), we were able to find that the stability line of $Gd_2O_3 + Cu_2O \leftrightarrow Gd_2CuO_4$ extended to the PO_2 regime of 10–150 mTorr, which is in accordance with our prediction that the stability boundary of Gd_2CuO_4 in relatively higher PO_2 regime, reported by W. Zhang *et al.* [5], may be extended to lower PO_2 region.

In Figs. 5 (a) and (b), however, it is difficult to observe the XRD peaks of the Gd_2CuO_4 or Gd_2O_3 phases. If a small amount of Gd_2CuO_4 or Gd_2O_3 existed in samples, it might be hardly detectable on the XRD patterns. Thus, we performed the scanning transmission electron microscopy (STEM)-energy dispersive X-ray spectroscopy (EDS) elemental mapping on these samples. As shown in Fig. 2. 6, round-shaped particle is believed to be the Gd_2CuO_4 phase, unobservable by XRD in Fig. 2. 5 (b), since Gd, Cu, and O are detectable

without Ba in red line area. In addition, the existence of Ba, Cu, and O at the outside of this particle suggest that the particle might be surrounded by liquid phase.

For further identification, we also tried to obtain the fast Fourier transform (FFT) patterns of this particle. Fig. 2. 7 (a) is the micrograph of high resolution transmission electron microscopy (HR-TEM), and Figs. 7 (b) and (c) are the fast fourier transform (FFT) patterns which correspond to (1) and (2) in Fig. 2. 7 (a), respectively. Calculating the *d*-spacing, the FFT patterns of Figs. 7 (b) and (c) match with the Gd_2CuO_4 and $BaCu_2O_2$ phases, respectively, which is in a good agreement with the spectral images shown in Fig. 2. 6 and the XRD pattern in Fig. 2. 5 (a).

2.3.3. Stability phase diagram of $GdBa_2Cu_3O_{7-\delta}$ for the nominal composition of Gd:Ba:Cu = 1:1:2.5 in PO_2 regime of 1–150 mTorr

Based on our experimental data, one can see that the GdBCO phase is formed by reaction of $Gd_2O_3 + L_1 \rightarrow Gd_2CuO_4 + L_2 \rightarrow GdBCO + Gd_2CuO_4 + Cu_2O$ in Fig. 2. 8(As shown in Fig. 2. 9, the black stability boundary line of GdBCO for this composition is remarkably shifted to the lower temperature regions compared with the red one of the nominal composition of Gd:Ba:Cu = 1:2:3 [1]. Though the stability line of GdBCO can be expressed by thermodynamic equation for the composition of Gd:Ba:Cu = 1:2:3, it is impossible to express the stability line for the composition of Gd:Ba:Cu = 1:1:2.5 by any

thermodynamic equation because it is the phase boundary between Gd_2CuO_4 + L_2 and GdBCO + Gd_2CuO_4 + Cu_2O. Interestingly, it is remarkable that Gd_2CuO_4 + L_2 is stable at the temperature region of gray shadow below the Gd_2O_3 + L_1 stable region in Fig. 2. 8 although the Gd_2CuO_4 phase is unobservable in Figs. 1 and 3. It can be suggested that Gd_2O_3 + L_1 might be preformed via the heat treatment path for the determination of the GdBCO phase boundary, and then Gd_2O_3 might react with L_1 to form Gd_2CuO_4 + L_2 at the surface of Gd_2O_3 particle with a core-shell structure in the stable zone of Gd_2CuO_4 + L_2. Below the GdBCO stability boundary, the Gd_2CuO_4 shell might be used up to react with L_2 and form GdBCO, and the inner Gd_2O_3 core could be trapped within GdBCO and thus detected by XRD.

On the basis of all our experimental results, the stability diagram could be constructed as shown in Fig. 2. 8, which describes the stability phase diagram of GdBCO for the nominal composition of Gd: Ba: Cu = 1:1:2.5 in PO_2 regime of 1-150 mTorr. As previously mentioned, the orange-dotted line is the extended stability line of Gd_2CuO_4. It is reported that Gd_2CuO_4 decomposes into Gd_2O_3 plus Cu_2O above that stability line [5].

2.4. Summary

In this study, we tried to determine the stability boundary of GdBCO and stable phases for the nominal composition of Gd:Ba:Cu = 1:1:2.5 in the low PO_2 regime of 1-150 mTorr by performing the XRD, FE-SEM, and TEM analyses of annealed samples. Based on our experimental data, we could

accurately construct the stability phase diagram of GdBCO for this composition in the low PO_2 regime of 1-150 mTorr. In conclusion, compared with the stability line of GdBCO for the nominal composition of Gd:Ba:Cu = 1:2:3, the GdBCO stability boundary is remarkably shifted to lower temperature region for this composition. Moreover, with decreasing temperature in a given PO_2, it is clear that GdBCO is formed by the following reactions of $Gd_2O_3 + L_1 \rightarrow Gd_2CuO_4 + L_2 \rightarrow GdBCO + Gd_2CuO_4 + Cu_2O$, which is also quite different from the peritectic recombination reaction of $Gd_2O_3 + L_1 \rightarrow GdBCO$ or Gd163 $+ L_3 \rightarrow$ GdBCO for the nominal composition of Gd:Ba:Cu = 1:2:3.

References

[1] J.-W. Lee, S.-M. Choi, J.-H. Song, J.-H. Lee, S.-H. Moon, and S.-I. Yoo, "Stability phase diagram of $GdBa_2Cu_3O_{7-\delta}$ in low oxygen pressures," *Journal of Alloys and Compounds,* vol. 602, pp. 78-86, 2014.

[2] J.-H. Lee, H. Lee, J.-W. Lee, S.-M. Choi, S.-I. Yoo, and S.-H. Moon, "RCE-DR, a novel process for coated conductor fabrication with high performance," *Superconductor Science and Technology,* vol. 27, no. 4, p. 044018, 2014.

[3] T.-H. Seok, I. Park, and S.-I. Yoo, "Stability diagram of $YBa_2Cu_3O_{7-\delta}$ in low oxygen pressures," *IEEE Transactions on Applied Superconductivity,* vol. 27, no. 4, pp. 1-5, 2016.

[4] T. Aselage and K. Keefer, "Liquidus relations in Y–Ba–Cu oxides," *Journal of Materials Research,* vol. 3, no. 6, pp. 1279-1291, 1988.

[5] W. Zhang and K. Osamura, "Oxygen pressure dependence of Cu_2O-CuO-Gd_2O_3 phase diagram," *Metallurgical Transactions B,* vol. 22, no. 5, pp. 705-710, 1991.

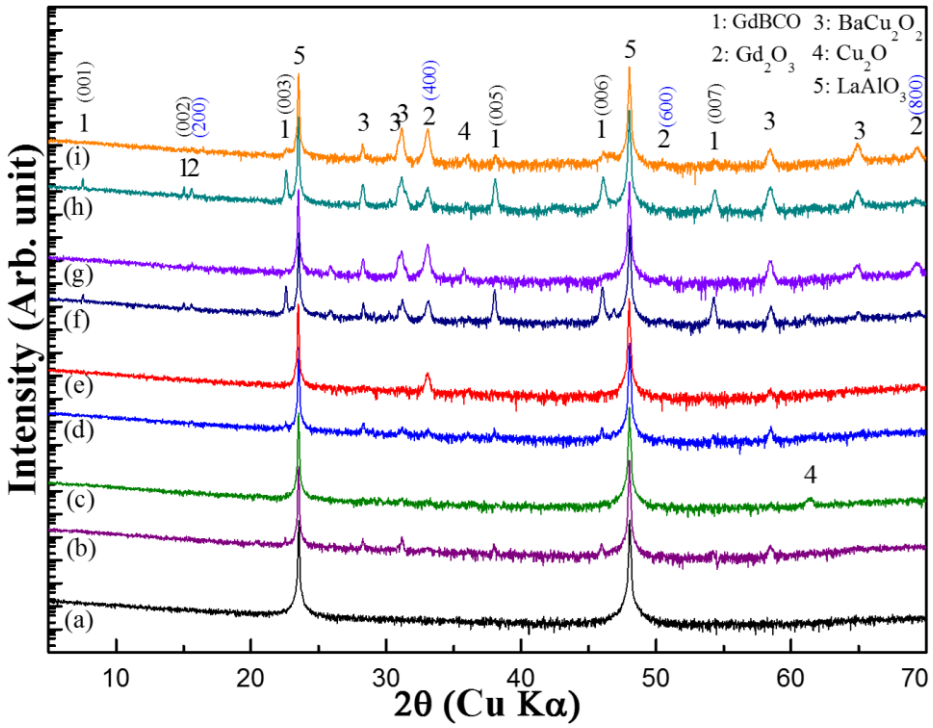

Fig. 2. 1. The XRD patterns of as-deposited amorphous film (a) and as-quenched films after annealing at (b) 692°C and (c) 696°C in the PO_2 of 1 mTorr for 2 h, at (d) 728°C and (e) 732°C in the PO_2 of 3 mTorr for 1 h, at (f) 772°C and (g) 776°C in the PO_2 of 10 mTorr for 30min, and at (h) 800°C and (i) 804°C in the PO_2 of 20 mTorr for 30min.

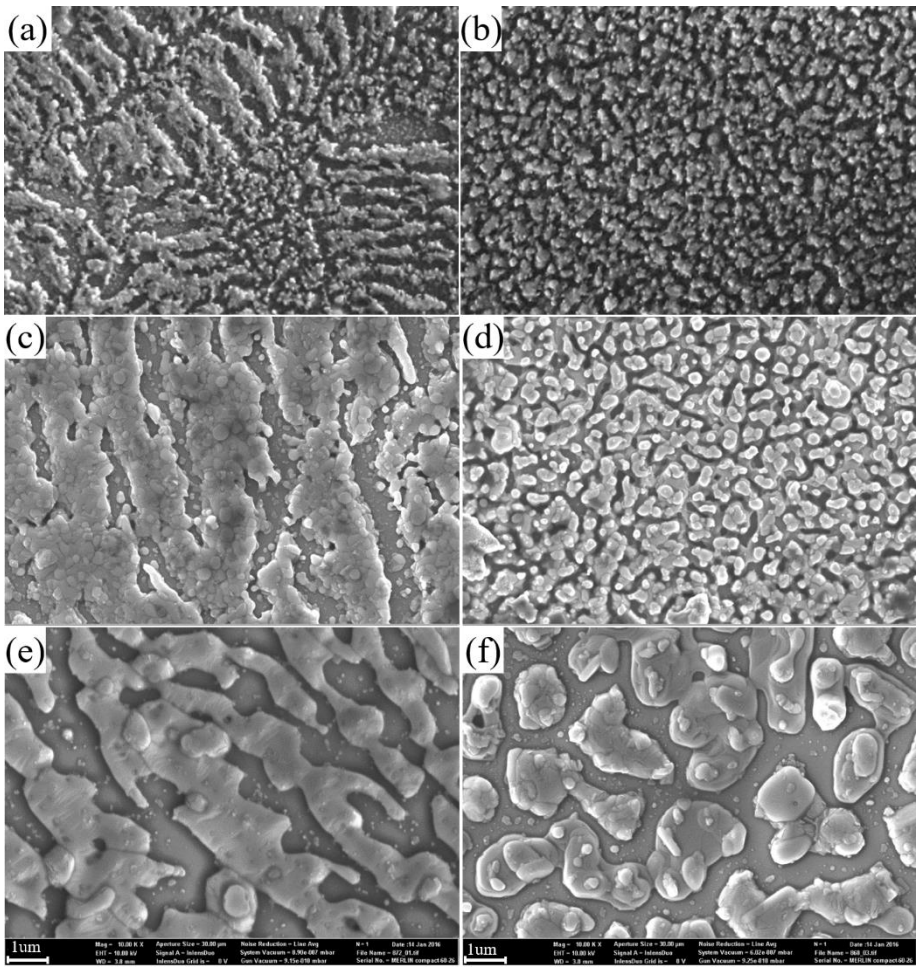

Fig. 2. 2. FE-SEM micrographs of as-quenched films after annealing at (a) 696°C and (b) 692°C in the PO_2 of 1 mTorr for 2 h, at (c) 820°C and (d) 816°C in the PO_2 of 30 mTorr for 30 min, and at (e) 868°C and (f) 864°C in the PO_2 of 150 mTorr for 5 min.

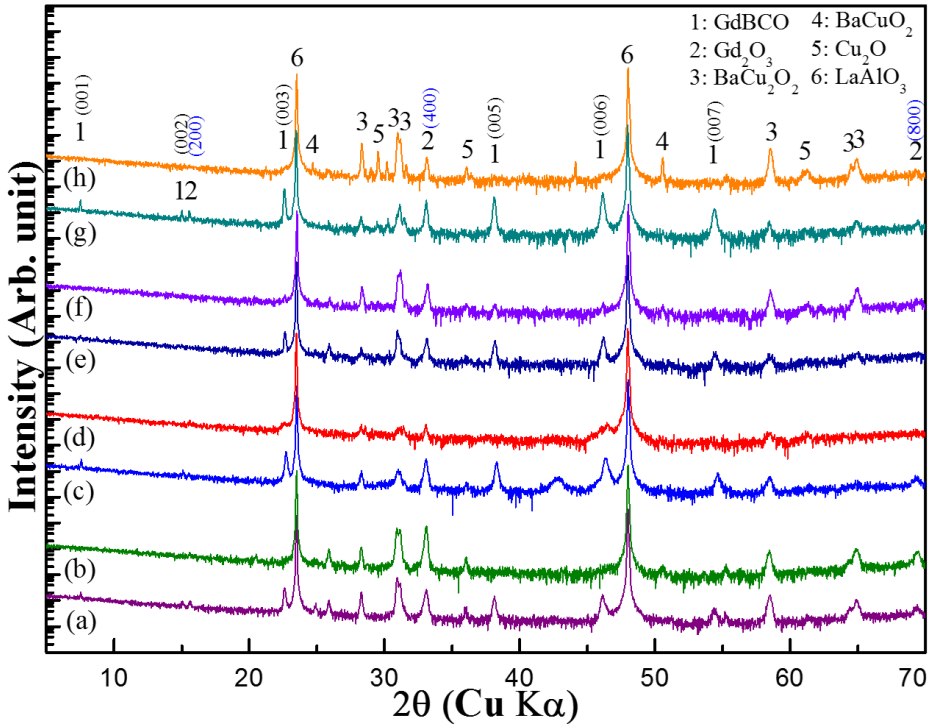

Fig. 2. 3. The XRD patterns of as-quenched films after annealing at (a) 816℃ and (b) 820℃ in the PO_2 of 30 mTorr for 30min, at (c) 832℃ and (d) 836℃ in the PO_2 of 50 mTorr for 15 min, at (e) 852℃ and (f) 856℃ in the PO_2 of 100 mTorr, and at (g) 864℃ and (h) 868℃ in the PO_2 of 150 mTorr for 5 min.

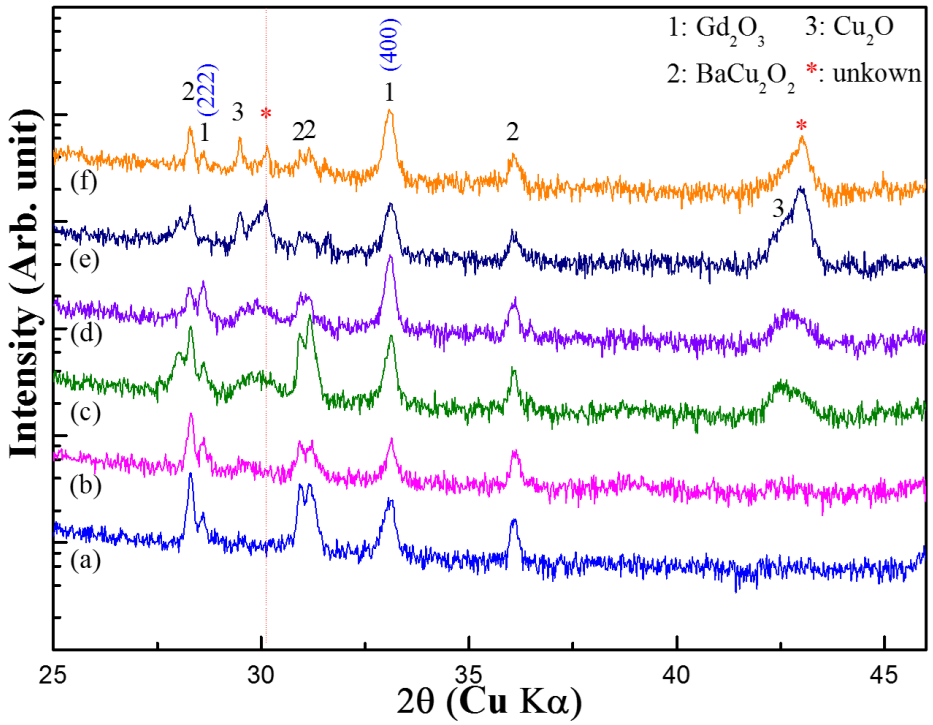

Fig. 2. 4. The XRD patterns of as-quenched films after annealing at (a) 776°C, (b) 780°C, (c) 800°C, (d) 808°C, (e) 820°C, and (f) 840°C in the PO_2 of 10 mTorr for 2h.

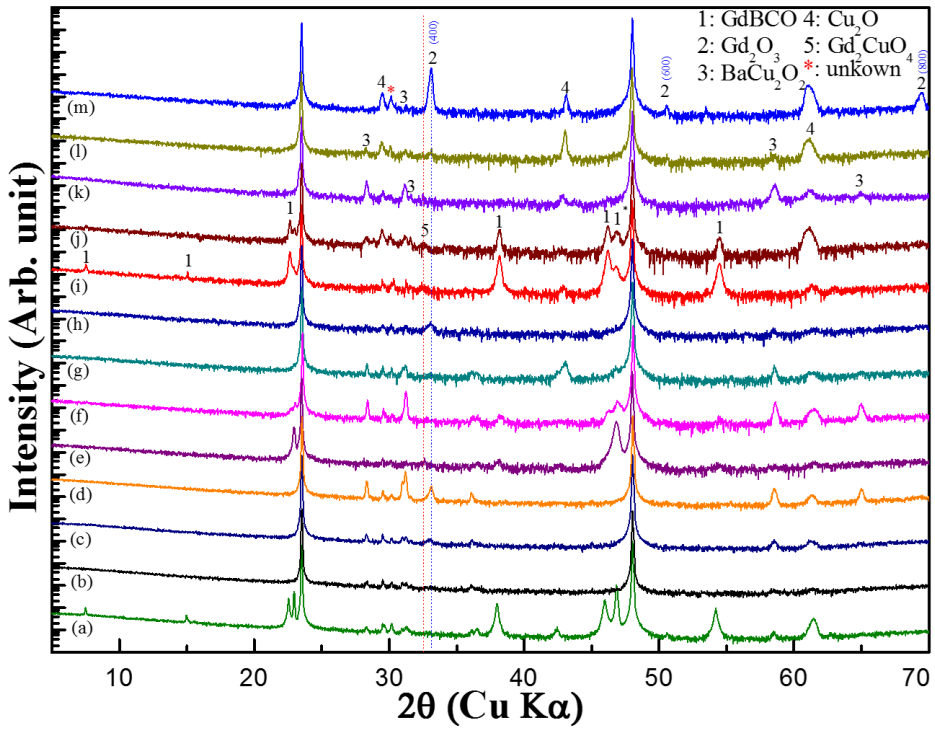

Fig. 2. 5. The XRD patterns of as-quenched films after annealing at (a) 690°C, (b) 720°C, (c) 736°C, and (d) 760°C in the PO_2 of 1 mTorr for 15h, at (e) 772°C, (f) 800°C, (g) 820°C, and (h) 840°C in the PO_2 of 10 mTorr for 3h, and at (i) 850°C, (j) 860°C, (k) 868°C, (l) 880°C, and (m) 900°C in the PO_2 of 150 mTorr for 30 min.

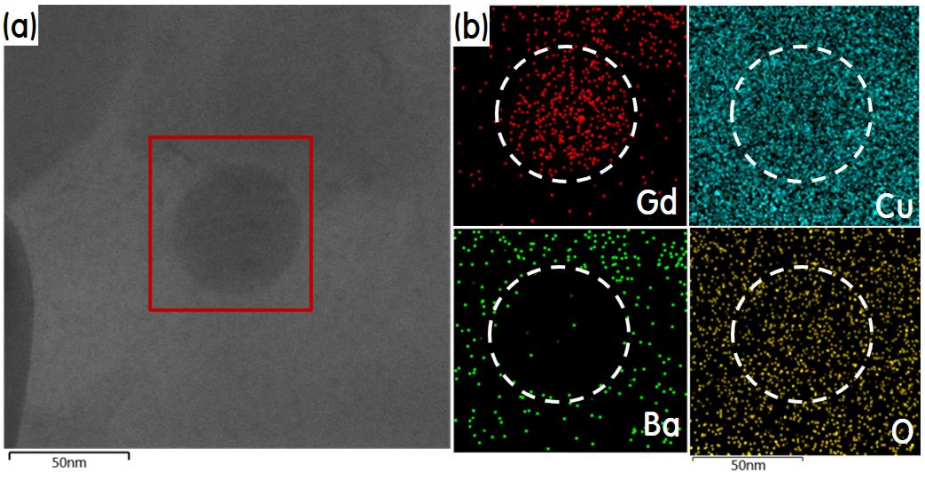

Fig. 2. 6. (a) Z-contrast STEM micrograph of as-quenched film after annealing at 720°C in the PO_2 of 1 mTorr for 15h, (b) Gd, Ba, Cu, and O spectral images analysed for the red line area in Fig. 2. 6. (a).

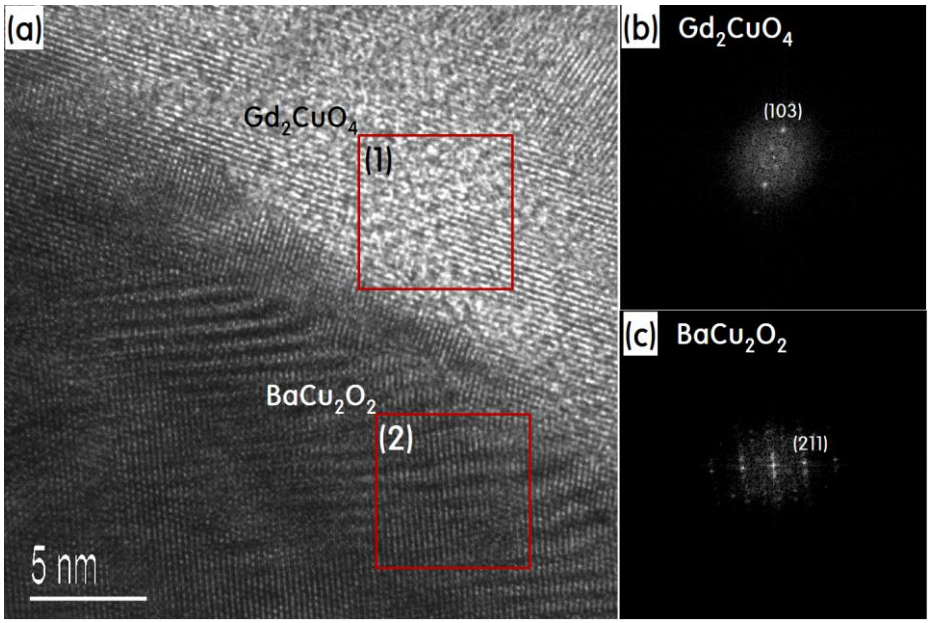

Fig. 2. 7. (a) HR-TEM micrograph of as-quenched film after annealing at 720°C in the PO_2 of 1 mTorr for 15h, and (b) and (c) FFT patterns of the square area (1) and (2) in Fig. 2. 7. (a), respectively.

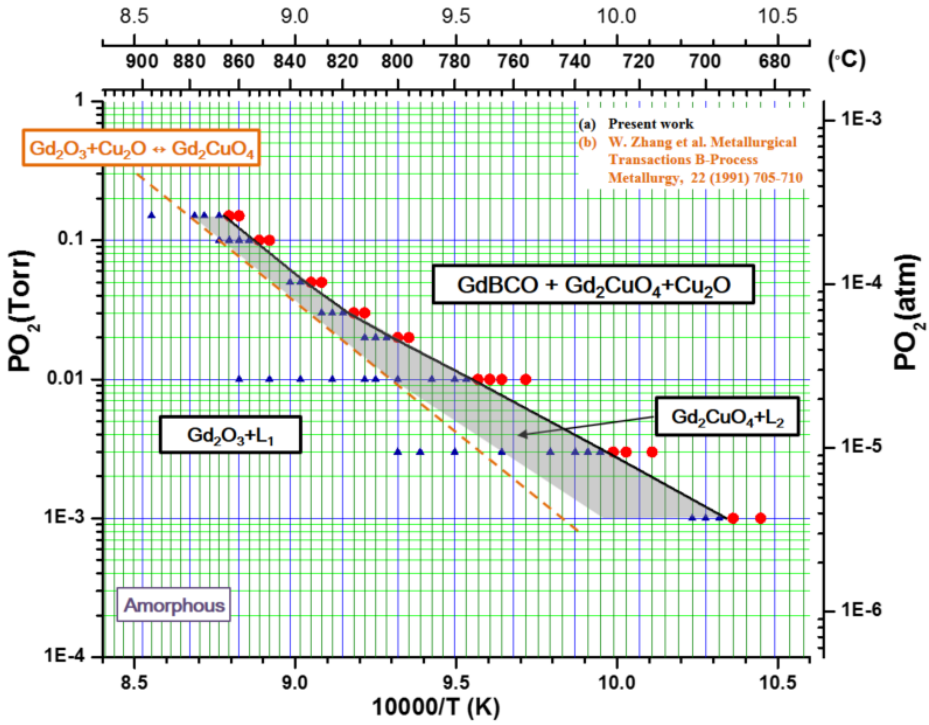

Fig. 2. 8. The stability phase diagram of GdBCO for the nominal composition of Gd:Ba:Cu = 1:1:2.5 in low oxygen (●: GdBCO stable, ▲: GdBCO unstable, gray shadow: Gd_2CuO_4 + L_2, orange dotted line: stability line of Gd_2CuO_4 determined by W. Zhang [5])

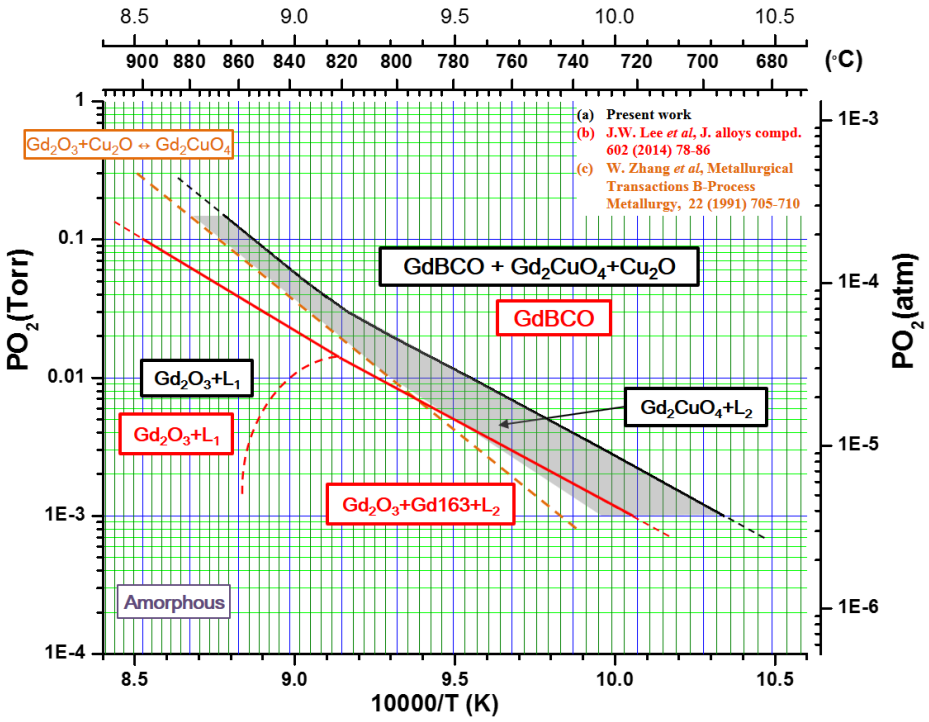

Fig. 2. 9. The stability phase diagram of GdBCO for the nominal composition of Gd:Ba:Cu = 1:1:2.5 in low oxygen is represented together with that for the nominal composition of Gd:Ba:Cu=1:2:3 from ref. [1] for a comparison. (orange dotted line: stability line of Gd_2CuO_4 determined by W. Zhang [5])

Chapter 3. The growth condition of c-axis aligned biaxially textured GdBCO film based on the stability phase diagram

3.1. Introduction

In order to manufacture a REBCO-based superconductor having a critical temperature of 90K or higher and a high critical current, it is important to control the crystal orientation [1-11]. For fabrication by the sintering or melting method, which is a common ceramic manufacturing method, the ionic radius of the rare earth element is large, which can be easily replaced by barium sites, and the critical temperature is greatly reduced [12-17]. For this purpose, if the melting method is performed by controlling the oxygen partial pressure, the replacement of the rare earth element with the Ba site can be effectively suppressed, and REBCO having excellent superconductivity can be manufactured. At this time, the process of forming REBCO superconductors through the reaction with the liquid phase in RE211 or RE422 requires a high temperature of around 1000 degrees, and the growth rate of the superconductor is very slow, so a heat treatment time of tens of hours or more is required. To solve this problem, it was possible to shorten the manufacturing time and lower the temperature of the system by forming a REBCO superconductor through RE_2O_3 + Liquid reaction in a lower oxygen partial pressure region [18].

However, until now, process conditions for obtaining a superconducting film having excellent biaxial orientation have not been established. This method aims to develop process technology and conditions for forming a GdBCO superconductor with good biaxial orientation.

3.2. Experimental

The amorphous precursor films were fabricated by a RCE-DR equipment of SuNAM. The GdBCO precursor layer was deposited on $LaSrMnO_3$-buffered IBAD (ion-beam assisted deposition)-MgO template on SUS substrate. Details on the architecture and the RCE-DR processing parameters have been previously reported by Lee *et al*. [18] . The amorphous precursor film with the nominal composition of Gd:Ba:Cu = 1:1:2.5 was consecutively deposited by electron beam evaporation. For the conversion from amorphous phase to superconducting phase, the conversion process was performed using a 6-zone reel-to-reel tube furnace shown in Fig. 3. 1, in which the oxygen partial pressure of each 3 zone can be controlled differently.

The GdBCO conversion conditions of temperature and PO_2 were carefully controlled. The annealing temperature was varied from the based on the phase boundary temperature to -30 ºC at each PO_2 regime. Since relatively low PO_2 and temperature lead to low reaction kinetics, in order to obtain equilibrium phases, the sample held for 10 ~ 20 min at the given PO_2 of 10, 20, and 50 mTorr. To analyze the phases and phase boundaries of samples, X-ray diffraction (XRD) was performed on the amorphous precursor and the GdBCO

films using an X-ray diffractometer (Bruker, D8 advance) with Cu-Kα radiation.

3.3. Results and discussion

The annealing path for the PO_2 of 150 mTorr with phase stability diagram is shown in Fig. 3. 2. The annealing process conditions are listed in the table 3. 1. Also, the annealing time is carried out by setting the growth conditions of GdBCO at 150 mTorr and setting the starting point and the endpoint passing section to about 104 sec (1 m/min) as considering the length of the furnace. As shown in Fig. 3.3, c-axis (00l) peaks are well-grown overall samples, however, below the temperature of 846 ºC, there are not only c-axis peaks but also a-axis peaks. In particular, it can be seen that a-axis growth occurred in the blue circle in Fig. 3.3. It means that a-axis growth occurs between the phase boundary of 866 ± 2 ºC and 848.5 ± 2.5 ºC, and a-axis growth occurs at lower temperatures.

Fig. 3.4 represent the XRD patterns annealed in the PO_2 of 100 mTorr. In the same way, c-axis growth with a-axis growth occurred below the temperature of 829 ºC. As a result, the c-axis growth region is between 854 ± 2 ºC and 831.5 ± 2.5 ºC at the PO_2 regime of 100 mTorr. Unlike the previous results of 100 and 150 mTorr, when the reel-to-reel speed was set to 104 seconds at the beginning and end without hold, the growth of GdBCO growth did not occur properly. It can be seen that the lower the oxygen partial pressure, the lower the phase boundary temperature relatively, causing a kinetically slow reaction rate, and thus the GdBCO phase was not properly formed. To solve this, two methods

were carried out. The first is to set the reel-to-reel non-continuous at the GdBCO growth point, thereby increasing the conversion time relatively. The second is increasing the heat treatment time with the reel-to-reel passing continuously as a whole at a slow rate at a slower rate. As shown in Fig. 3.5, as a result of the first method, even when hold for 3 minutes, the GdBCO phase was not formed properly, so it was increased to 10 minutes. At this time, it was confirmed that the GdBCO phase was formed. As a result of GdBCO formation using the second method, when the furnace passage time was increased from 104 seconds to 164 seconds and 256 seconds using reel-to-reel, it was not formed properly, but GdBCO was formed when reel-to-reel was stopped at GdBCO conversion point. It was confirmed through the method of holding and heat treatment using the first method.

Fig. 3. 6 and 3.7 describe the XRD patterns of the samples annealed in the PO_2 of 50, 20 mTorr, respectively. An a-axis growth occurred below the temperature 809 ºC for 50 mTorr and 787 ºC for 20 mTorr. That is, c-axis growth region is between 834 ± 2 ºC and 811.5 ± 2.5 ºC at the PO_2 regime of 50 mTorr and 802 ± 2 ºC and 889.5 ± 2.5 ºC at the PO_2 regime of 20 mTorr. For the condition of PO_2 at 10 mTorr, the sample hold for 20 min at GdBCO conversion region in reel-to-reel tube furnace as considering relatively low temperature and oxygen pressure. As shown in Fig. 3.8, as a result of annealing at 769 ºC, which is 5 ºC lower than the phase boundary temperature at 10 mTorr, the a-axis was significantly grown as high intensity of a-axis growth was detected. The possibility that the phase boundary was wrong could not be excluded, so the XRD pattern of the sample heat-treated at 10 ºC higher temperature (779 ºC)

than the phase boundary was confirmed. As a result, when GdBCO phase was undetectable and but Gd_2O_3 phase was detected, it was confirmed once again that the phase boundary was accurately determined at 10 mTorr. It means a-axis growth occurred at a temperature just below the phase boundary in the PO_2 of 10 mTorr. The process conditions with c-axis growth without a-axis growth are listed in Table. 3.2. Also, the overall result is represented with the stability phase diagram for the nominal composition of Gd:Ba:Cu = 1:1:2.5 in Fig. 3.9[19].

3.4. Summary

In the case of GdBCO CCs fabrication process, in order to fabricate high-performance GdBCO superconducting wire, it is necessary to grow GdBCO with c-axis by avoiding a-axis growth because the c-axis growth of the GdBCO superconducting layer affects the biaxially textured growth of the superconducting wire. Thus, we tried to identify the growth region of c-axis aligned biaxially textured GdBCO by the increasing undercooling temperature in the PO_2 region of 10 - 150 mTorr. The c-axis aligned biaxially textured GdBCO growth region is below the undercooling temperature of ~ 20 ºC in the PO_2 of 50, 100, and 150 mTorr. Below the PO_2 of 10 mTorr, it is impossible to grow c-axis aligned biaxially textured GdBCO CCs since both c-axis and a-axis growth occur together. To achieve c-axis aligned GdBCO CCs fabricated by RCE-DR process, it is highly recommended that annealing condition for GdBCO growth should be positioned yellow region in the stability phase diagram in Fig. 3.9[19].

Reference

[1] D. Dimos, P. Chaudhari, J. Mannhart, and F. LeGoues, "Orientation Dependence of Grain-Boundary Critical Currents in $YBa_2Cu_3O_{7-\delta}$ Bicrystals," *Physical Review Letters,* vol. 61, no. 2, p. 219, 1988.

[2] B. Moeckly, S. Russek, D. Lathrop, R. Buhrman, J. Li, and J. W. Mayer, "Growth of $YBa_2Cu_3O_7$ thin films on MgO: The effect of substrate preparation," *Applied physics letters,* vol. 57, no. 16, pp. 1687-1689, 1990.

[3] Y. Iijima, N. Tanabe, O. Kohno, and Y. Ikeno, "In-plane aligned $YBa_2Cu_3O_{7-\delta}$ thin films deposited on polycrystalline metallic substrates," *Applied Physics Letters,* vol. 60, no. 6, pp. 769-771, 1992.

[4] B. Kim *et al.*, "Effect of Mg (OH) 2 on $YBa_2Cu_3O_7$ thin film on MgO substrate studied by atomic force microscope," *Journal of Vacuum Science & Technology B: Microelectronics and Nanometer Structures Processing, Measurement, and Phenomena,* vol. 12, no. 3, pp. 1631-1634, 1994.

[5] G. Watson, S. Holt, R.-P. Zhao, A. Katsaros, N. Savvides, and S. Myhra, "Environmental degradation of $YBa_2Cu_3O_{7-x}$ thin films. Analysis by atomic force microscopy," *Physica C: Superconductivity,* vol. 243, no. 1-2, pp. 123-133, 1995.

[6] C. Wang, K. Do, M. Beasley, T. Geballe, and R. Hammond, "Deposition of in-plane textured MgO on amorphous Si_3N_4 substrates by ion-beam-assisted deposition and comparisons with ion-beam-assisted deposited yttria-stabilized-zirconia," *Applied Physics Letters,* vol. 71, no. 20, pp. 2955-2957, 1997.

[7] Y. Iijima, K. Kakimoto, and K. Takeda, "Ion beam assisted growth of fluorite type oxide template films for biaxially textured HTSC coated

conductors," *IEEE transactions on applied superconductivity,* vol. 11, no. 1, pp. 3457-3460, 2001.

[8] T. Aytug *et al.*, "Single buffer layers of $LaMnO_3$ or $La_{0.7}Sr_{0.3}MnO_3$ for the development of $YBa_2Cu_3O_{7-\delta}$ coated conductors: A comparative study," *Journal of materials research,* vol. 17, no. 9, pp. 2193-2196, 2002.

[9] T. Muroga *et al.*, "CeO/sub 2/buffer layers deposited by pulsed laser deposition for TFA-MOD $YBa_2Cu_3O_{7-x}$ superconducting tape," *IEEE transactions on applied superconductivity,* vol. 13, no. 2, pp. 2532-2534, 2003.

[10] P. N. Arendt and S. R. Foltyn, "Biaxially textured IBAD-MgO templates for YBCO-coated conductors," *MRS bulletin,* vol. 29, no. 8, pp. 543-544, 2004.

[11] R. Hühne, S. Fähler, L. Schultz, and B. Holzapfel, "Thin biaxially textured MgO and TiN films prepared by ion-beam assisted pulsed laser deposition for coated conductor applications," *Physica C: Superconductivity and its applications,* vol. 426, pp. 893-898, 2005.

[12] K. Miyachi, K. Sudoh, Y. Ichino, Y. Yoshida, and Y. Takai, "The effect of the substitution of Gd for Ba site on $Gd_{1+x}Ba_{2-x}Cu_3O_{6+\delta}$ thin films," *Physica C: Superconductivity,* vol. 392, pp. 1261-1264, 2003.

[13] K. Zhang *et al.*, "Solubility and superconductivity in RE $(Ba_{2-x}RE_x)Cu_3O_{7+\delta}$ systems (RE= Nd, Sm, Eu, Gd, Dy)," *Journal of Physics C: Solid State Physics,* vol. 20, no. 34, p. L935, 1987.

[14] A. Hu, H. Zhou, N. Sakai, and M. Murakami, "Modulation of the peak effect in melt-processed $(Sm_{1-x}Eu_x)Ba_2Cu_3O_{7-\delta}$ superconductors with compositional fluctuation," *Applied physics letters,* vol. 81, no. 25, pp. 4796-4798, 2002.

[15] H. Wu, M. Kramer, K. Dennis, and R. McCallum, "Precipitation from $Gd_{(1+x)}Ba_{(2-x)}Cu_3O_7$ superconductor in low oxygen partial pressure," *IEEE transactions on applied superconductivity,* vol. 7, no. 2, pp. 1731-

1734, 1997.

[16] M. Kramer, S. Yoo, R. McCallum, W. Yelon, H. Xie, and P. Allenspach, "Hole filling, charge transfer and superconductivity in $Nd_{1+x}Ba_{2-x}Cu_3O_{7+\delta}$," *Physica C: Superconductivity,* vol. 219, no. 1-2, pp. 145-155, 1994.

[17] M. Izumi *et al.*, "Structural properties of the superconductor $LaBa_2Cu_{3-y}O_{7-z}$ in the solid solution system $La_{1+x}Ba_{2-x}Cu_{3-y}O_{7-z}$," *Physical Review B,* vol. 40, no. 10, p. 6771, 1989.

[18] J.-H. Lee, H. Lee, J.-W. Lee, S.-M. Choi, S.-I. Yoo, and S.-H. Moon, "RCE-DR, a novel process for coated conductor fabrication with high performance," *Superconductor Science and Technology,* vol. 27, no. 4, p. 044018, 2014.

[19] I. Park, W.-J. Oh, J.-H. Lee, S.-H. Moon, and S.-I. Yoo, "Stability phase diagram of Gd $Ba_2Cu_3O_{7-\delta}$ for the nominal composition of Gd: Ba: Cu= 1: 1: 2.5 in low oxygen pressures," *IEEE Transactions on Applied Superconductivity,* vol. 28, no. 4, pp. 1-5, 2018.

Table. 3. 1. The condition of annealing process

(ºC)

Temp. / PO_2	Phase Boundary	-5ºC	-10ºC	-15 ºC	-20 ºC	-25 ºC	-30 ºC
150 mTorr	866 ± 2	861	856	851	846	841	836
100 mTorr	854 ± 2	849	844	839	834	829	824
50 mTorr	834 ± 2	829	824	819	814	809	804
20 mTorr	802 ± 2	797	792	787	782	777	-
10 mTorr	774 ± 2	769	-	-	-	-	-

Table. 3. 2. The summary of phase boundary and c-axis growth boundary

(ºC)

PO_2 / Temp.	150 mTorr	100 mTorr	50 mTorr	20 mTorr	10 mTorr
Phase boundary	866 ± 2	854 ± 2	832 ± 2	802 ± 2	774 ± 2
c-axis growth	848.5 ± 2.5	831.5 ± 2.5	809.5 ± 2.5	789.5 ± 2.5	774

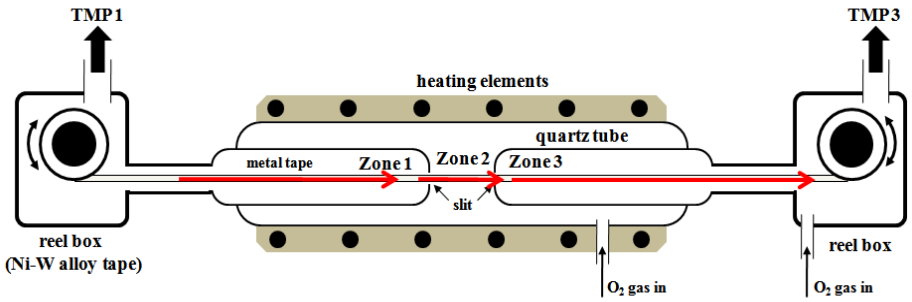

Fig. 3. 1. The schematic of reel-to-reel tube furnace apparatus.

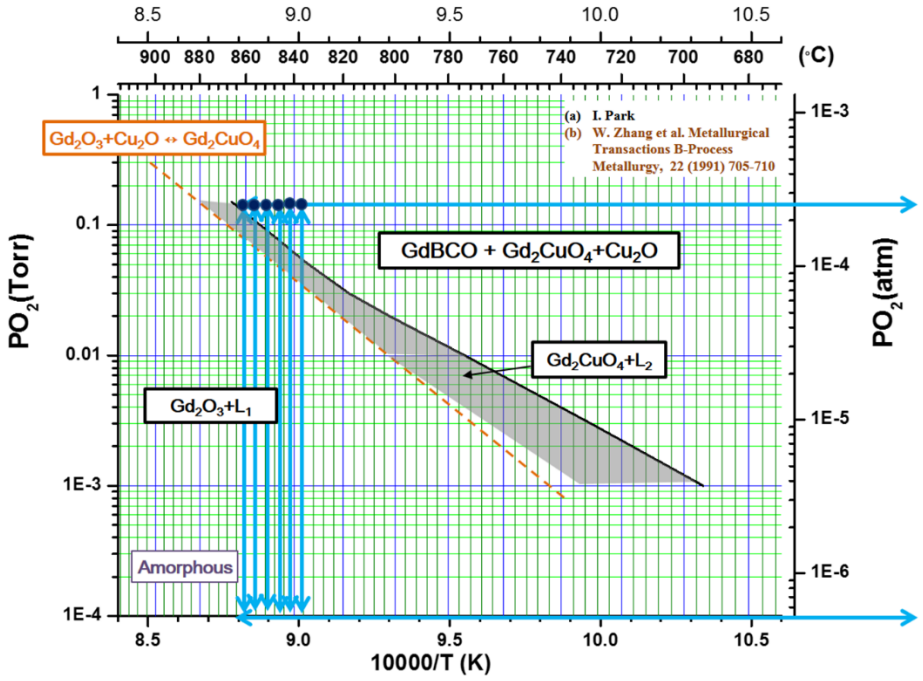

Fig. 3. 2. The annealing path in the *P*O2 of 150 mTorr

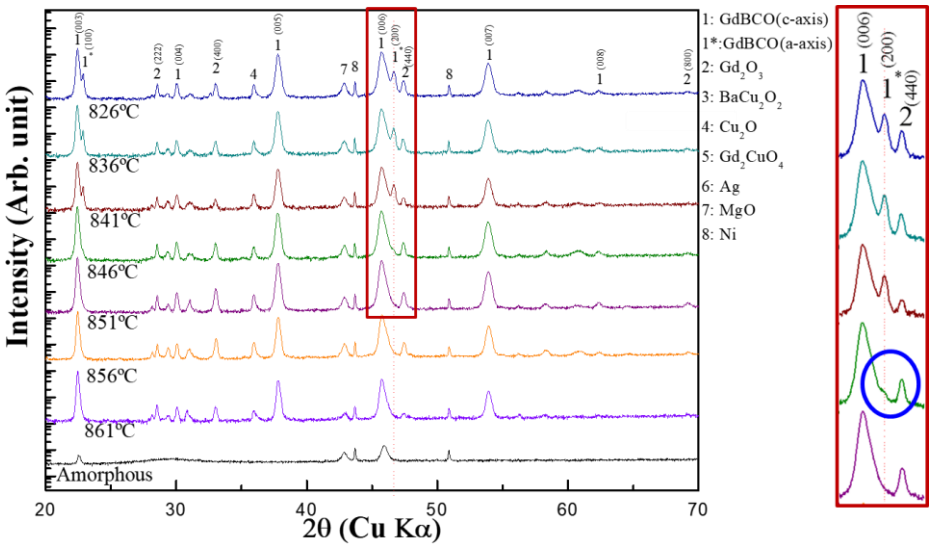

Fig. 3. 3. The XRD patterns of each sample annealed in the PO_2 of 150 mTorr (left) and magnified the red box (right).

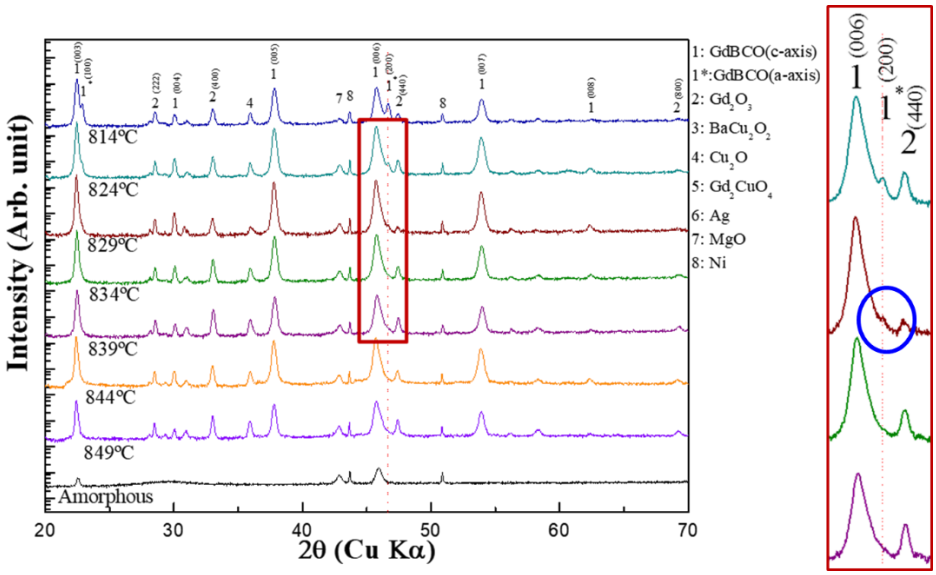

Fig. 3. 4. The XRD patterns of each sample annealed in the PO_2 of 100 mTorr (left) and magnified the red box (right).

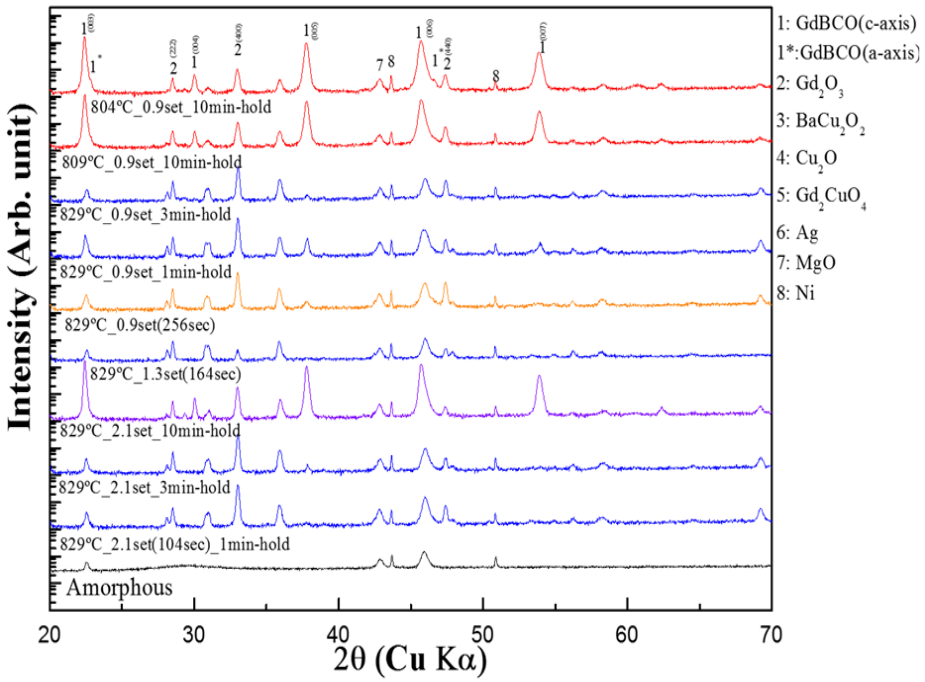

Fig. 3. 5. The XRD patterns of each sample annealed different annealing time in the PO_2 of 50 mTorr.

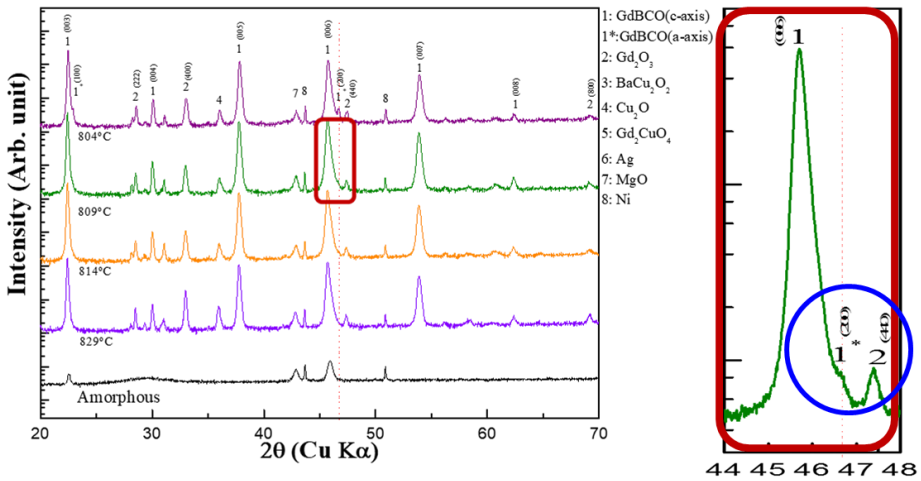

Fig. 3. 6. The XRD patterns of each sample annealed in the PO_2 of 50 mTorr (left) and magnified the red box (right).

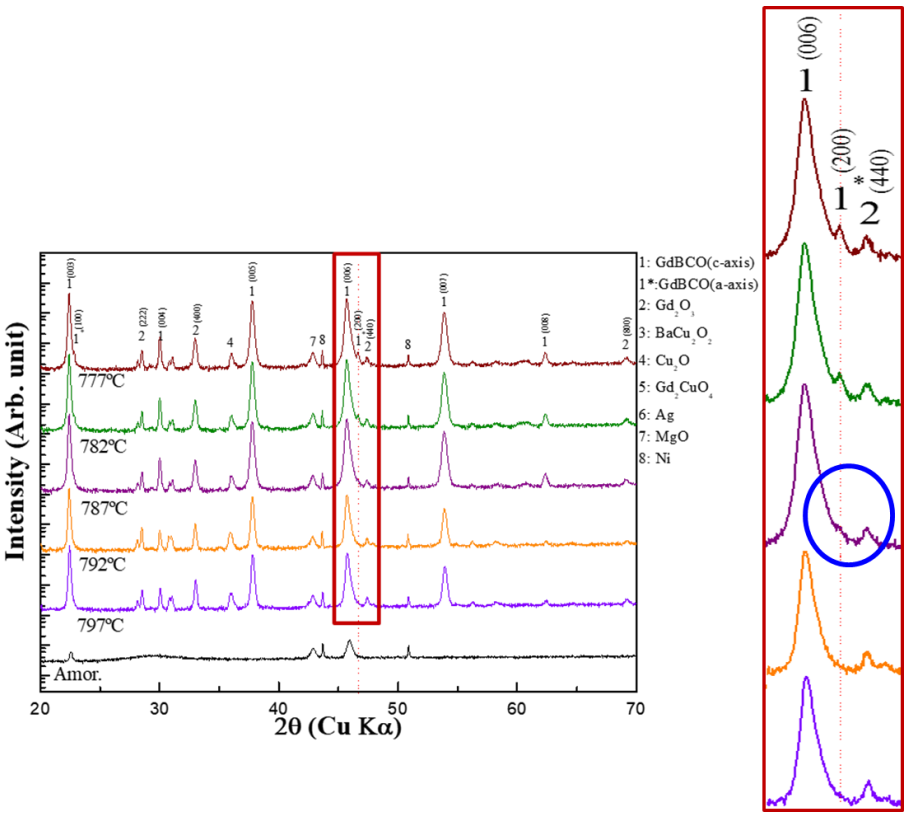

Fig. 3. 7. The XRD patterns of each sample annealed in the PO_2 of 20 mTorr (left) and magnified the red box (right).

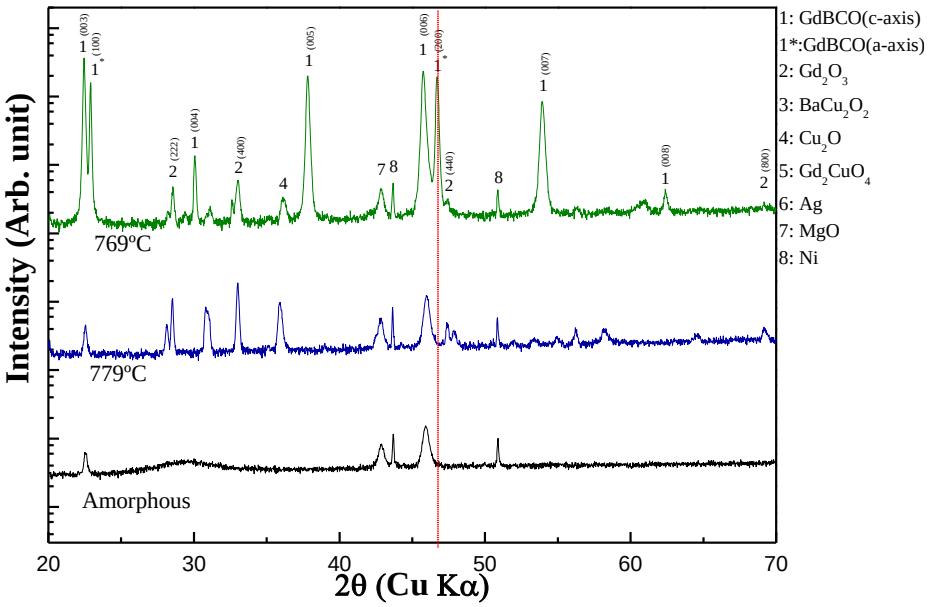

Fig. 3. 8. The XRD patterns of each sample annealed in the PO_2 of 10 mTorr.

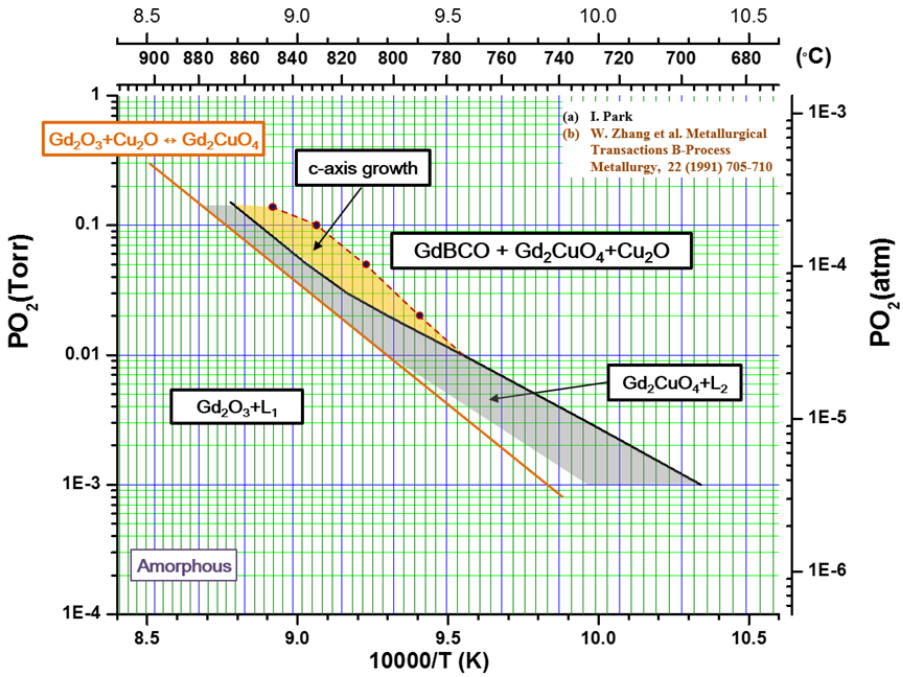

Fig. 3. 9. Stability phase diagram of GdBCO for the nominal composition of 1:1:2.5[19] with c-axis growth region.

Chapter 4. Fabrication of high performance GdBCO Coated Conductors by the RCE-DR process

4.1. Introduction

A long-length 2nd generation high-temperature superconductors (HTS) on the basis of $REBa_2Cu_3O_{7-\delta}$ (REBCO, RE = Y and rare earth elements) cuprates, normally called as coated conductors (CCs), have been fabricated by various technologies such as pulsed laser deposition (PLD) [1], metal-organic chemical vapor deposition (MOCVD) [2], metal-organic deposition (MOD) [3], and co-evaporation [4, 5] processes. Due to high current carrying capacity and low operating cost, REBCO CCs are considered to be suitable for superconducting electric power applications [6]. However, further improvement of in-field J_c values of REBCO CCs is still highly required [7]. Among all these processes, the RCE-DR process is known as the most cost-effective one because of its high throughput due to the high growth rate of REBCO layer [5].

According to the report by C. Senatore *et al*. [8], compared with REBCO CCs fabricated by PLD, MOD, and MOCVD processes, GdBCO CCs fabricated by the RCE-DR process shows relatively lower in-field Jc value at 4.2 K in 19 T even though it exhibits the highest self-field J_c at 77 K. Therefore, as listed in Table. 4.1, for the enhancement of pinning properties of GdBCO CC

via RCE-CR, there have been many efforts such as doping [9], post-annealing [10-12], proton irradiation [13], initial composition control [14], and the growth temperature of GdBCO control [15].

Also, as mentioned previously in Chapter 1, efforts to improve the pinning properties by optimizing the size and amount of second phase particles trapped within the REBCO superconducting matrix have been attempted in all fabrication processes, and it is known that this method is effective. Fig. 1.9 and 1. 10 represent the optimal amount of second phases, which act as 3D-APCs without 1D-APCs such as columnar defects and its average particle size and in-field magnetic J_c values at 77 K in 1 T. [16-24] The particle size seems to relate to the amount of the second phase and in-field J_c values. However, the GdBCO CCs via RCE-DR normally include somewhat large Gd_2O_3 second phase particles with an average particle size of ~120 nm and 33mol%. [25] In other words, it is possible to enhance the pinning properties of GdBCO CCs via RCE-DR by optimizing the size and amount of Gd_2O_3 second phase particles.

In our previous studies, though we tried to refine the Gd_2O_3 particle, we could not achieve appropriate process conditions due to without considering of undercooling temperature for GdBCO growth lead to the randomly oriented growth of GdBCO [15], and contamination of amorphous precursor by air exposure [26]. However, in this work, by avoiding these problems, we could successfully fabricate high performance GdBCO CCs.

In this work, without additional process, further enhancement on electrical properties was expected by refining Gd_2O_3 particles, which is formed inevitably in RCE-DR by controlling the process condition especially growth temperature

of Gd_2O_3 since Gd_2O_3 average particle size in GdBCO matrix is relatively large. With decreasing the growth temperature of Gd_2O_3 from 860 to 800 ℃ in the oxygen pressure of 20 and 30 mTorr, the average particle size of Gd_2O_3 was gradually decreased from a maximum of 137 ± 52 to a minimum of 73 ± 31 nm. The self-field J_c values were principally affected in-plane and out-of-plane. On the other hand, the stacking faults and interfacial pinning by refined Gd_2O_3 particles mainly act as pinning centers and affect J_c values under the magnetic field.

4.2. Experimental

The fabrication of GdBCO CCs was used through the RCE-DR process. The fabricated GdBCO CCs have layer structure of GdBCO superconducting layer / $LaSrMnO_3$ buffer layer / IBAD-MgO template / Hastelloy substrate. The details of the architecture and the RCE-DR process reported by Lee, *et al*. [5]. To compare the results of each experimental set and to avoid interference by other external factors such as substrate and template conditions, degree of vacuum, etc., the experiment was performed at once using a substrate about 600m long by controlling the partial oxygen pressure and temperature, and the amorphous precursor film with the nominal composition of Gd:Ba:Cu = 1:1:2.5 was consecutively deposited by electron beam evaporation.

According to our previous study on the stability phase diagram of $GdBa_2Cu_3O_{7-\delta}$ (Gd123) for the nominal composition of Gd:Ba:Cu = 1:1:2.5 [27], the Gd123 phase is grown by the peritectic recombination of Gd_2O_3 plus

liquid, and excessive Gd_2O_3 phase are trapped in Gd123 during the Gd123 growth. On the basis of this stability phase diagram, we selected the growth temperatures of Gd_2O_3 particles in the liquid from 800 to 860 ºC and from 820 to 860 ºC in the given oxygen pressure of 20 and 30 mTorr, respectively, and the subsequent growth of GdBCO film was performed at the same conditions of 860 ºC in 150 mTorr oxygen pressure. Additionaly, we selected the growth temperatures of Gd_2O_3 particles in the liquid from 820 to 850 ºC in the given oxygen pressure of 30 mTorr, and subsequent growth of GdBCO film was performed at the same conditions of 850 ºC in 100 mTorr oxygen pressure. As-grown GdBCO films were oxygen-annealed at 500 ºC for 8h.

In this work, the sample IDs are firstly classified in to 30-150 mTorr, 20-150 mTorr, and 30-100 mTorr depending on the partial oxygen pressure, and the first and second PO_2 represent the growth conditions of Gd_2O_3 and GdBCO, respectively. Secondly, the sample IDs are denoted as 860-860C, 850-860C, 840-860C, 830-860C, 820-860C, 810-860C, 800-860C, 850-850C, 840-850C, 830-850C, and 820-850C with the first and second temperature referring to the growth temperature of Gd_2O_3 and GdBCO, respectively. We conducted a total of 3 different sets of experiments depending on the condition of partial oxygen pressure.

To analyze the phases of samples, X-ray diffraction (XRD) was performed on the amorphous precursor and the GdBCO CCs using an X-ray diffractometer (Bruker, D8 advance) with Cu-Kα radiation. Analyses of in-plane (φ-scan) and out-of-plane (ω-scan) textures for GdBCO (103) and GdBCO (005) reflections, respectively, were performed using an X-ray diffractometer (PANalytical,

X'pert Pro). The critical temperatures (T_c) of all samples were measured by a four probe *R-T* measurement system, and the I_c values were measured with the conventional *I-V* measurement system. The microstructures of GdBCO CCs were observed by field emission scanning electron microscopy (FE-SEM) (ZEISS, MERLIN Compact). FE-SEM and TEM specimens were prepared by focused ion beam (FIB) (SII Nanotechnology, SMI3050SE). Spherical aberration corrected transmission electron microscopy (Cs corrected TEM) (Thermo Fisher, Themis Z) was used for the microstructural analysis, acquiring high-angle annular dark-field scanning transmission electron microscopy (HAADF-STEM) images and volume rendered views of 3D reconstructed tomographic. The angular dependency of in-field J_c values was measured for GdBCO CCs with the physical property measurement system (PPMS) (Quantum Design, PPMS-14) at 65 and 77 K after laser patterning a micro-bridge (~100 μm) in the specimens. The field dependency of magnetic J_c values for *B*//c was measured for GdBCO CCs with the superconducting quantum interference device (SQUID)-vibrating sample magnetometer (VSM) (Quantum Design, MPMS 3) at 20, 40, 65 and 77 K. The value of magnetic J_c was calculated by the equation of $J_c = 20\Delta M/[a(1-(a/3b))]$ in the modified Bean's critical state model [28], where a and b are width and length of the film measured in centimeter (b > a), and ΔM is the width of the magnetization hysteresis loop measured in emu/cm^3.

4.3. Results and discussion

4.3.1. Determination of the process path based on the stability phase diagram

For the fabrication of high performance 2nd generation high temperature superconductors, bi-axially textured growth is paramount [29]. So that, based on our previous report of stability phase diagram of GdBCO for the nominal ccomposition of Gd:Ba:Cu = 1:1:2.5 [26], by XRD analysis, the bi-axially textured growth region was determined and it is represented in Figure 4.1 with yellow shadow region.

Using this stability phase diagram with bi-axially textured growth region, as mentioned before we conducted 3 different process route set as 30-150 mTorr, 20-150 mTorr, 30-100 mTorr. For the set of 20-150 mTorr, compared to the set of 30-150 mTorr, the phase boundary, which is not converted to GdBCO, is about 820 ºC in 30 mTorr and about 800 ºC in 20 mTorr as shown in Figure 1, so that available process condition of Gd_2O_3 growth temperature is wider than 30-150 mTorr set. It is also expected that Gd_2O_3 particles trapped in the GdBCO matrix would be refined as the growth temperature of Gd_2O_3 is lowered from 820 ºC to 800 ºC.

In addition, for the set of 30-100 mTorr, to determine the characteristic differences from GdBCO growth conditions, the growth conditions of GdBCO was changed from 850 ºC, 5 ºC lower than the phase boundary at PO_2 of 100 mTorr, rather than 860 ºC at PO_2 of 150 mTorr, which is typical conditions for

GdBCO fabrication process in RCE-DR.

4.3.2. Process conditions for PO_2 of 30 mTorr for Gd_2O_3 and 150 mTorr for GdBCO

Fig. 4. 2 shows the XRD patterns of the amorphous precursor and as-grown GdBCO films. As shown in Fig. 2(a), the precursor film is amorphous since a characteristic broad peak near $2\theta = 30^{o}$ is observed and other peaks are from MgO and Hastelloy substrate. From Figs. 4. 2(b)-(f), we can see that all as-grown GdBCO samples are well aligned along the c-axis without forming randomly oriented grains which had been observed for the GdBCO film grown at 840 ºC in the same oxygen pressure. [15] Also, it can be seen that all samples commonly include the second phases of Gd_2O_3 and CuO. Unlike our previous report [26], the $BaCu_2O_2$ phase is undetectable because amorphous precursor samples were not exposed to air in this study. In accordance with our expectation, no appreciable difference between samples in their XRD patterns is observable since the growth conditions of GdBCO film were unaltered.

To evaluate I_c and J_c values in self-field at 77.3K, we measured the *I-V* curves in liquid nitrogen as shown in Fig. 4. 3. Since the distance between voltage taps is 5 cm, and the black dashed line in Fig. 4. 3 indicates the criterion of 1μV/cm for the determination of I_c values. Sample 860-860C shows the highest I_c value of 717A/12mm-width. In addition, with decreasing the growth temperature of Gd_2O_3, I_c values are monotonously decreased to 495A/12mm-width. In Table I, the superconducting properties and textures of our samples

are summarized. Though the *R-T* curves of samples are represented Fig. 4. 4, their $T_{c,\,zero}$ values of samples are almost identical, as listed in Table. 4.2. Their resistivity values at room temperature are in the region of 388.5–481.2 μΩ·cm.

Figs. 4. 5(a)-(e) show the cross-sectional FE-SEM micrographs observed using a back-scattered electron (BSE) detector to distinguish the second phases of Gd_2O_3 and CuO from the GdBCO matrix. We can observe bright and dark particles dispersed randomly in the GdBCO matrix. According to the elemental analysis in our previous reports [25, 26], the bright and dark particles are Gd_2O_3 and CuO phases, respectively. Fig. 4.6 displays two different volume rendered views of 3D reconstructed tomographic of sample 820-860C, and both second phases of Gd_2O_3 and CuO are not perfect spherical shape. In addition, the average particle sizes of Gd_2O_3, which were estimated by calculating the diameter of a circle having the same circumference as the particle, are plotted as a function of the growth temperature of Gd_2O_3 in Fig. 4. 5 (f). Samples 860-860C, 850-860C, 840-860C, 830-860C, and 820-860C have the average Gd_2O_3 particle sizes of 125 ± 41, 116 ± 42, 103 ± 42, 97 ± 32, and 73 ± 31 nm, and the average CuO particle sizes of 194 ± 114, 185 ± 80, 179 ± 79, 160 ± 74, 149 ± 82 nm, respectively, implying that the average particle sizes of both Gd_2O_3 and CuO gradually decrease with decrease in the growth temperature of Gd_2O_3. Moreover, the number of smaller Gd_2O_3 particles is increased by lowering the growth temperature of Gd_2O_3. These results suggest that with lowering the growth temperature of Gd_2O_3, its nucleation rate is increased while its growth rate is decreased. Further, with lowering the growth temperature of Gd_2O_3, the areal fractions of the Gd_2O_3 phase were slightly decreased while those of the

CuO phase were almost unaltered within the GdBCO matrix though not presented here, suggesting that the areal fraction of GdBCO superconducting matrix was slightly increased.

Although the areal fractions of the Gd_2O_3 particle are slightly decreased with decreasing its growth temperature, its three-dimensional interfacial area within the GdBCO matrix is continuously increases if the continuous decrease of its average particle size in Fig. 4. 5. (f) is taken into account. In other words, the increasing effect due to dominate the decreasing effect due to the slight decrease of its areal fraction. If we only consider the slight increase in the areal fraction of the GdBCO matrix and the increase in the interfacial are between Gd_2O_3 particles and GdBCO matrix with lowering the growth temperature of Gd_2O_3, a gradual increase in self-field J_c is expected. However, the self-field J_c in Table 4. 2 are opposite to this expectation. Therefore, the gradual degradation of self-field J_c with lowering the growth temperature of Gd_2O_3 may be attributed to the gradual degradation of both in-plane ($\Delta\varphi$) and out-of-plane ($\Delta\omega$) alignments as listed in Table 4. 1.

4.3.3. Process conditions for PO_2 of 20 mTorr for Gd_2O_3 and 150 mTorr for GdBCO

This section describes the set of 20-150 mTorr. This set represents growth conditions of GdBCO at 860 ºC in 150 mTorr oxygen pressure, and growth conditions of Gd_2O_3 in 20 mTorr with the variable of temperature from 800 ºC to 860 ºC. Fig. 4.7 shows *I-V* curves of the samples, which were measured under

liquid nitrogen (77K) atmosphere without magnetic field (self-field). The same as previous section, due to 5 cm distance of voltage taps, the red horizontal line in Fig. 4.7 implies the criterion of 1uV/cm for determining the critical current (I_c) values. Similar to the set of 30-150 mTorr, as lowering the growth temperature of Gd_2O_3, the tendency of critical current values is decrease. Though the sample 840-860 (572A/12mm-width) is lower than 830-860 (598A/12mm-width), it could be neglected with a small difference of around 4%. The *R-T* curves of samples are represented in Fig. 4.8, since there is no significant difference as $T_{c,\,zero}$ and resistivity at room temperature values are in the region of 92.9 - 93.4 K and 440.2-567.3 μΩ·cm, respectively.

To check the phases and the FWHM of (003) peak of GdBCO, the XRD pattern of samples was analyzed as shown in Fig. 4. 9. For sample 860-860C, 850-860C, 840-860C, 830-860C, and 820-860C, there are no notable differences of phases, and the (00*l*) peaks of GdBCO are well grown with bi-axially textured growth without a-axis growth. However, unexpectedly, for the sample 800-860C and 810-860C, the XRD patterns show not only c-axis growth but also a-axis growth as shown in Fig. 4. 9 (g) and (h). In theta-2theta (θ-2θ) scans, there are two a-axis (*h*00) peaks in the 20º - 60º region, one is (100) positioned at 23.2º, and the other is (200) positioned at 47.5º. Since the peak of (200) overlaps (440) peak of Gd_2O_3 as marked red dotted line in Fig. 4. 9, the a-axis growth is identified through the peak of (100) located 23.2º. Unexpected a-axis growth could be occured due to differences in the rate of increase in oxygen pressure and temperature for the substrate by a uniquely designed furnace of RCE-DR equipment [5, 26]. For example, when the sample

passed Gd_2O_3 growth zone under a process condition of 800 ºC at 20 mTorr, subsequently the atmosphere is changed to 860 ºC in 150 mTorr, but the oxygen partial pressure changes rapidly, while the temperature of the substrate rises relatively slowly. For this reason, unexpected a-axis growth occurs, and leading to relatively sharp drop in self-field I_c value. The FWHM values of (003) reflection from the XRD patterns in Fig. 4. 9 are 0.267, 0.284, 0.312, 0.275, and 0.316 for sample of 860-860C, 850-860C, 840-860C, 830-860C, and 820-860C, respectively. For the samples 810-860C and 800-860C, due to the a-axis growth, the values of FWHM were excluded.

Fig. 4. 10 (a) - (g) show the cross-sectional micrograph for analyzing the change in particle size and shape according to the growth temperature of Gd_2O_3. FE-SEM with a back-scattered electron (BSE) detector that can distinguish each phase of Gd_2O_3 and CuO from GdBCO matrix was used for these micrographs. As previously mentioned, there are two distinguishable particles randomly scattered in GdBCO matrix, and the dark and bright particles are Gd_2O_3 and CuO, respectively. The average particle size of Gd_2O_3 and CuO are 137 ± 52 and 183 ± 71 nm for 860-860C, 113 ± 58 and 177 ± 56 nm for 850-860C, 106 ± 31 and 171 ± 61 nm for 840-860C, 94 ± 50 and 159 ± 56 nm for 830-860C, 85 ± 52 and 157 ± 52 nm for 820-860C, 74 ± 33 and 130 ± 44 nm for 810-860C, and 77 ± 37 and 153 ± 47 nm for 800-860C. For the samples 810-860C and 800-860C, which have a-axis growth, the amount of CuO in GdBCO matrix are relatively small than other samples. In addition, overall Gd_2O_3 average particle size tendency is more refined as growth temperature of Gd_2O_3 decreases as shown in Fig. 4. 10 (h).

4.3.4. Process conditions for PO_2 of 30 mTorr for Gd_2O_3 and 100 mTorr for GdBCO

This section 3.3 describe about the set of 30-100 mTorr. Considering the other sets of 30-150, 20-150 mTorr, the process window of 30-100 mTorr set is small, but different characteristics are expected because of different growth conditions of GdBCO. The $T_{c,zero}$ values are in the range 93.1 - 93.6 K and resistivity at room temperature are in the range of 377.8-505.1 μΩ·cm as shown in 4.11. Similar to the set of 20-150 mTorr.

Fig. 4.12 displays the *I-V* curves for 12mm-width GdBCO CC samples. It should be noted in Fig. 4. 12 is that unlike other 20-150 and 30-150 mTorr sets, it does not follow the trend, and the self-field I_c value is rather higher despite the low growth temperature of Gd_2O_3. A discussion of this part is described in section 4. 3. 2 along with the other 20-150 and 30-150 mTorr sets. θ-2θ scans of samples represent in Fig. 4. 13. The XRD patterns show bi-axially textured GdBCO growth without forming other phases and a-axis growth. FWHM values of the sample 850-850C, 840-850C, 830-850C, and 820-850C are 0.222, 0.211, 0.215, and 0.229, respectively. These values are relatively lower than the values from the samples of other sets.

For the analysis of the particles, the micrographs were observed as illustrated Fig. 4. 14. As mentioned before, the bright particle Gd_2O_3 and dark particle CuO are randomly strewed in GdBCO matrix. The average Gd_2O_3 particle size of sample 850-850C, 840-850C, 830-850C, and 820-850C are 118 ± 56, 107 ± 47, 98 ± 33, and 77 ± 33 nm, respectively. Also, average particle sizes of CuO

are 160 ± 69 nm for sample 850-850C, 160 ± 72 nm for sample 840-850C, 129 ± 75 nm for sample 830-850C, and 99 ± 56 nm for 820-850C. The same with previous results, the tendency of average particle size of Gd_2O_3 is more refined as the growth temperature of Gd_2O_3 decreased as shown in Fig. 4. 14 (e). Comparing with overall samples from each process set, the average particle size of Gd_2O_3 could be refined around 70 nm.

4.3.5. Electrical properties under the magnetic field

This section describes all three different sets of 30-150, 20-150, and 30-100 mTorr. Fig. 4. 15 represents plots of the self-field I_c values in each process set as a function of Gd_2O_3 growth temperature. As mentioned in section 4. 3. 2, the tendency of self-field I_c value decreases by lowering Gd_2O_3 growth temperature for the sets of 30-150, 20-150 mTorr, but the set of 30-100 mTorr does not follow that trend. According to our previous section 4. 3. 2 for the set of 30-150 mTorr, the self-field I_c value is affected by the texture of GdBCO matrix. Accordingly, both in-plane ($\Delta\varphi$) and out-of-plane ($\Delta\omega$) scans are analyzed, and these are comprehensively shown in Fig. 4. 16 for all sets of 30-150, 20-150, and 30-100 mTorr. In the case of 30-150, 20-150 mTorr sets, the values of $\Delta\varphi$ and $\Delta\omega$ gradually increase as the growth temperature of Gd_2O_3 decreases. However, for the set of 30-100mTorr, the tendency is erratic, which is the same as the tendency of self-field I_c values. In particular, for the sample 30-100 mTorr_830-850C with the highest self-field I_c value, it shows the lowest value in $\Delta\varphi$ and $\Delta\omega$. Overall, comparing Fig. 4. 15 and 4. 16, the degradation of self-

field I_c value might be attributed by degradation $\Delta\varphi$ and $\Delta\omega$ alignments.

Fig. 4. 17 shows the angular dependence of in-field J_c values, measured at 77 K in 1 and 5 T, at 65 K in 3 and 7 T, for five different GdBCO CC samples. With decreasing growth temperature of Gd_2O_3 from 860 to 820 ºC, in-field J_c values are first increased and then decreased. With increasing the external field, the difference becomes negligible. Interestingly, from Table 4.1, one can see that, with decreasing the growth temperature of Gd_2O_3 from 860 to 820 ºC, while J_c values in self-field are monotonously decreased, minimum in-field J_c values are first increased and then decreased again. The monotonous decrease of self-field J_c may be attributed to the gradual degradation of both in-plane and out-of plane textures as shown in Table 4.1. However, the enhancement in in-field J_c values must be related to more effective flux pinning.

According to our previous study [12], higher stacking fault (SF) density within the GdBCO matrix gives rise to broader (00*l*) peaks in the XRD pattern, and further the SF density greatly affects the angular dependency of in-field J_c values. The FWHM values of (003) reflections in Fig. 4. 2 are listed in Table 4. 1. From the Table 4. 2, one can see that the FWHM values of (003) reflections are first slightly increased with decreasing the growth temperature of Gd_2O_3 from 860 to 840 ºC, and then decreased with further down to 820 ºC, indirectly representing the variation of the SF density. Interestingly, the variation of in-field $J_{c,\,min}$ values match with that of the FWHM values, suggesting that in-field $J_{c,\,min}$ values are sensitive to the SF density. Furthermore, the difference in the angular dependency of in-field J_c values in Fig. 4. 17 might originate mainly from the difference in the SF density. However, the variation of the angular

dependency of in-field J_c values is unexplainable only by the variation of the SF density, indirectly indicated by the variation of FWHM values in Table I, for instance, $J_{c,\,min}$ values of 860-860C sample are much lower than those of 820-860C sample even though 860-860C sample exhibits much higher FWHM value compared with 820-860C sample. Thus, we consider that the interfacial pinning between Gd_2O_3 particles and GdBCO matrix is somewhat responsible for this discrepancy since the relative interfacial area ratio increases as the average Gd2O3 particles are refined. The interfacial area ratio is estimated by assuming the Gd_2O_3 particle is spherical and calculating the surface area of the sphere, and listed in Table 4. 3. To confirm this point, as shown in Fig. 4. 18, TEM analysis was conducted for the samples 860-860C, 840-860C, and 820-860C, which are the set of 30-150 mTorr, and 830-850C the set of 30-100 mTorr. It is clearly observable that the SFs as a distinctive streak perpendicular to the c-axis of a white dotted line are randomly distributed in GdBCO matrix. The average linear stacking fault density was characterized by analyzing the number of SF on five different cross-sectional TEM micrographs (488 x 488 nm^2 for the sample 830-850C, 627 x 627 nm^2 for the sample 860-860C, 840-860C, and 820-860C) for each sample. The average linear SF densitys are 0.40 ($\pm$ 0.05) x 10^6 /cm, 0.44 ($\pm$ 0.04) x 10^6 /cm, 0.35 ($\pm$ 0.06) x 10^6 /cm, and 0.30 ($\pm$ 0.04) x 10^6 /cm for the sample 860-860C, 840-860C, 820-860C, and 830-850C, respectively. the average linear SF density is proportional to FWHM values of (003) reflection, and it is in good agreement with the previous report [12]. Additionally, in order to identify the stacking fault, we performed the STEM analysis for the sample 830-850C with high resolution HAADF micrographs as

shown in Fig. 4.19. In Fig. 4. 19 (c) and (d), the black streak, which can be seen as stacking fault, is different from ordinary Gd123 and has a CuO plane added shape and is identified as Gd125 or Gd125.

In Fig. 4. 17, we measured angular dependence of J_c with transport, where there is a difference in the values of $J_{c,\,min}$ and J_c for B//c, but there is no order difference in the values of each sample. Accordingly, J_c under the magnetic field is described with J_c-B curves instead of the angular dependence of J_c as shown in Fig. 4. 20. To determine the critical current density under the magnetic field, magnetic J_c for H//c was analyzed at 77, 65, 40, and 20 K via SQUID-VSM for half of the samples, and the log-log plots of J_c-B for B//c are shown in Fig. 10 (a)-(d). Also, for ease of comparison, the values of J_c under each magnetic field are represented in Table 4. 3.

The samples from the set of 30-100 mTorr show higher J_c values than other samples at almost all temperatures and magnetic fields, while 800-860C sample from 20-150 mTorr set shows very low values in all regions due to the strong a-axis growth in GdBCO matrix. Overall, comparing with the self-field J_c at 77K measured by transport and magnetic J_c at 77K, 0.01 T, a higher self-field J_c value shows high magnetic J_c at 0.01T since there is a plateau region ($J_c \approx$ constant) at the relatively low magnetic field. The difference values between self-field J_c and magnetic J_c come from the different measuring methods because transport J_c shows generally higher value than magnetic J_c. For both samples of 820-860C from the sets of 30-150, 20-150 mTorr with relatively low J_c values in a low magnetic field, at the higher magnetic field at 77, 65 K, it has a tendency to reverse the value of the samples showing high J_c values in

relatively low magnetic fields. Furthermore, although there are only up to 7 T data, the J_c values in higher magnetic fields at 20, 40 K are expected to be reversed as well. In the case of the set of 30-150 mTorr, angular dependence of J_c was confirmed in the previous data, and that the same tendency was observed in the case of 20-150 mTorr set by understanding the trend of the J_c-B curves. This implies that the effect of interfacial pinning refined Gd_2O_3 particles in the magnetic field is higher than SF. Also, for the set of 30-100 mTorr, considering the FWHM values of (003) peak of GdBCO, the SF density is almost the same. It means that the in-field J_c value of samples of 30-100 mTorr set is comparable to the effect of relative interfacial area ratio without SF density. Comparing between the sample 820-850C and 830-850C, the self-field Jc value of sample 830-850C is higher, but the in-field J_c value is lower than sample 820-850C.

Consequently, the variation in the critical current density value under the magnetic field is mainly attributed to changes in SF density and increased interfacial pinning by refined Gd_2O_3 particles while lowering the growth temperature of Gd_2O_3. Consequently, we believe that improved pinning properties can be understood as increased interfacial pinning from refined Gd_2O_3 particles and the stacking faults by added CuO plane.

The exponent α, which has a relationship with $J_c \propto H^{-\alpha}$ in the power-law region, are not reamarkable change (~1.0 at 77K and ~0.8 at 65K) and still larger than the samples fabricated other methods such as MOD [30] and PLD [31], however comparing with each set, the samples from 30-100 mTorr set show relatively lower values. In Fig. 20 (e)- (h), the pinning force density (F_p) for the samples calculated by the relationship of $F_p = J_c \times B$ are shown as a

function of the magnetic field at 20, 40, 65, 77 K for B//c. For the samples from the set of 30-100 mTorr, the maximum pinning force densities seem to move slightly higher magnetic field and show higher values in every temperature region.

4.3. Summary

In order to fabricate high-performance GdBCO CCs fabricated by the RCE-DR process, we tried to refine the Gd_2O_3 particle inclusions in GdBCO superconducting matrix. The Gd_2O_3 growth temperature was controlled while GdBCO growth conditions were fixed. As lowering the growth temperature of Gd_2O_3 from 860 ℃ to 800 ℃ at 20 and 30 mTorr, the average particle size of Gd_2O_3 gradually decreased from 137 ± 52 to at least 73 ± 31 nm. As the average particle size of Gd_2O_3 was refined, the J_c value at the self-field, 77 K was monotonously reduced. Furthermore, given the J_c-B curves of the entire sample, the samples fabricated with varying temperatures in the PO_2 of 30 mTorr for Gd_2O_3 growth and 100 mTorr for GdBCO growth were generally higher than those fabricated under different conditions. The highest performance GdBCO CCs were obtainable from the following: transport self-field J_c at 77K is 4.82 MA/cm^2 for the sample 830-850C of 30-100 mTorr set, in-field magnetic J_c for B//c at 77K 1T is 0.22 MA/cm^2, $F_{p,max}$ is 2.6 GN/cm^3 at 77K, 0.4T for the sample 820-850C of 30-100 mTorr set.

The self-field J_c values were principally affected in-plane and out-of-plane textures. Whereas the variation in the critical current density value under the

magnetic field is mainly attributed to changes in SF density and increased interfacial pinning by refined Gd_2O_3 particles while lowering the growth temperature of Gd_2O_3. Consequently, we believe that improved pinning properties can be understood as increased interfacial pinning from refined Gd_2O_3 particles and the stacking faults by added CuO plane.

References

[1] H. Kutami *et al.*, "Progress in research and development on long length coated conductors in Fujikura," *Physica C: Superconductivity,* vol. 469, no. 15-20, pp. 1290-1293, 2009.

[2] V. Selvamanickam *et al.*, "High performance 2G wires: From R&D to pilot-scale manufacturing," *IEEE transactions on applied superconductivity,* vol. 19, no. 3, pp. 3225-3230, 2009.

[3] M. W. Rupich *et al.*, "Advances in second generation high temperature superconducting wire manufacturing and R&D at American Superconductor Corporation," *Superconductor Science and Technology,* vol. 23, no. 1, p. 014015, 2009.

[4] H. Ha *et al.*, "Critical current density of SmBCO coated conductor on IBAD-MgO substrate fabricated by co-evaporation," *Physica C: Superconductivity and its applications,* vol. 463, pp. 493-496, 2007.

[5] J.-H. Lee, H. Lee, J.-W. Lee, S.-M. Choi, S.-I. Yoo, and S.-H. Moon, "RCE-DR, a novel process for coated conductor fabrication with high performance," *Superconductor Science and Technology,* vol. 27, no. 4, p. 044018, 2014.

[6] D. Larbalestier, A. Gurevich, D. M. Feldmann, and A. Polyanskii, "High-T_c superconducting materials for electric power applications," *Materials For Sustainable Energy: A Collection of Peer-Reviewed Research and Review Articles from Nature Publishing Group,* pp. 311-320, 2011.

[7] S. Foltyn *et al.*, "Materials science challenges for high-temperature superconducting wire," *Materials For Sustainable Energy: A Collection of Peer-Reviewed Research and Review Articles from Nature Publishing Group,* pp. 299-310, 2011.

[8] C. Senatore, C. Barth, M. Bonura, M. Kulich, and G. Mondonico,

"Field and temperature scaling of the critical current density in commercial REBCO coated conductors," *Superconductor Science and Technology,* vol. 29, no. 1, p. 014002, 2015.

[9] W.-J. Oh *et al.*, "Enhanced Pinning Properties of Sm-Doped GdBCO CCs by the RCE-DR Process," *IEEE Transactions on Applied Superconductivity,* vol. 29, no. 5, pp. 1-4, 2019.

[10] W.-J. Oh *et al.*, "The Post-Annealing Effect on the Pinning Properties of $GdBa_2Cu_3O_{7-\delta}$ Coated Conductors via RCE-DR," *IEEE Transactions on Applied Superconductivity,* vol. 28, no. 4, pp. 1-5, 2018.

[11] J.-W. Lee, S.-M. Choi, W.-J. Oh, J.-H. Lee, S.-H. Moon, and S.-I. Yoo, "Enhanced Pinning Properties of $GdBa_2Cu_3O_{7-d}$ Coated Conductors via a Post-Annealing Process," *IEEE Transactions on Applied Superconductivity,* vol. 26, no. 3, pp. 1-6, 2016.

[12] W.-J. Oh, I. Park, K. Chung, J.-H. Lee, S.-H. Moon, and S.-I. Yoo, "Effect of post-annealing on the pinning properties of $GdBa_2Cu_3O_{7-\delta}$ coated conductors prepared by RCE-DR," *Superconductor Science and Technology,* vol. 33, no. 8, p. 085007, 2020.

[13] N. Haberkorn, J. Kim, S. Suárez, J.-H. Lee, and S. Moon, "Influence of random point defects introduced by proton irradiation on the flux creep rates and magnetic field dependence of the critical current density J_c of co-evaporated $GdBa_2Cu_3O_{7-\delta}$ coated conductors," *Superconductor Science and Technology,* vol. 28, no. 12, p. 125007, 2015.

[14] J. MacManus-Driscoll *et al.*, "Strong pinning in very fast grown reactive co-evaporated $GdBa_2Cu_3O_{7-\delta}$ coated conductors," *APL Materials,* vol. 2, no. 8, p. 086103, 2014.

[15] S.-M. Choi, J.-W. Lee, J.-H. Lee, S.-H. Moon, and S.-I. Yoo, "The Effect of Growth Temperature on $GdBa_2Cu_3O_{7-\delta}$ Coated Conductors Fabricated by the RCE-DR Process," *IEEE Transactions on Applied Superconductivity,* vol. 25, no. 3, pp. 1-5, 2014.

[16] W. Zhang *et al.*, "Control of flux pinning in MOD YBCO coated

conductor," *IEEE transactions on applied superconductivity,* vol. 17, no. 2, pp. 3347-3350, 2007.

[17] Y. Yoshida *et al.*, "Controlled nanoparticulate flux pinning structures in $RE_{1+x}Ba_{2-x}Cu_3O_y$ films," *Physica C: Superconductivity and its applications,* vol. 445, pp. 637-642, 2006.

[18] X. Obradors *et al.*, "Epitaxial $YBa_2Cu_3O_{7-x}$ nanocomposite films and coated conductors from BaMO3 (M= Zr, Hf) colloidal solutions," *Superconductor Science and Technology,* vol. 31, no. 4, p. 044001, 2018.

[19] P. Mele *et al.*, "Insertion of nanoparticulate artificial pinning centres in $YBa_2Cu_3O_{7-x}$ films by laser ablation of a Y_2O_3-surface modified target," *Superconductor Science and Technology,* vol. 20, no. 7, p. 616, 2007.

[20] N. Long *et al.*, "Enhanced in-field critical currents of YBCO second-generation (2G) wire by Dy additions," *Superconductor Science and Technology,* vol. 18, no. 12, p. S405, 2005.

[21] L. Lei, G. Zhao, H. Xu, N. Wu, and Y. Chen, "Influences of Y2O3 nanoparticle additions on the microstructure and superconductivity of YBCO films derived from low-fluorine solution," *Materials Chemistry and Physics,* vol. 127, no. 1-2, pp. 91-94, 2011.

[22] M. Z. Khan *et al.*, "Improving the flux pinning with artificial BCO nanodots and correlated dislocations in YBCO films grown on IBAD-MgO based template," *IEEE Transactions on Applied Superconductivity,* vol. 29, no. 5, pp. 1-5, 2019.

[23] J. Gutierrez *et al.*, "Strong isotropic flux pinning in solution-derived $YBa_2Cu_3O_{7-x}$ nanocomposite superconductor films," *Nature materials,* vol. 6, no. 5, pp. 367-373, 2007.

[24] X. Cui, B. Tao, Z. Tian, J. Xiong, X. Zhang, and Y. Li, "Enhancement of flux pinning of TFA-MOD YBCO thin films by embedded nanoscale Y_2O_3," *Superconductor Science and Technology,* vol. 19, no. 8, p. 844,

2006.

[25] S.-M. Choi *et al.*, "Characteristics of high-J_c GdBCO coated conductors fabricated by the RCE-DR process," *IEEE transactions on applied superconductivity,* vol. 23, no. 3, pp. 8001004-8001004, 2012.

[26] I. Park, W. Oh, J. Lee, S. Moon, and S. Yoo, "Refinement of Gd_2O_3 inclusions in the $GdBa_2Cu_3O_{7-\delta}$ films fabricated by the RCE-DR process," *Progress in Superconductivity and Cryogenics,* vol. 20, no. 4, pp. 46-49, 2018.

[27] I. Park, W.-J. Oh, J.-H. Lee, S.-H. Moon, and S.-I. Yoo, "Stability phase diagram of $GdBa_2Cu_3O_{7-\delta}$ for the nominal composition of Gd: Ba: Cu= 1: 1: 2.5 in low oxygen pressures," *IEEE Transactions on Applied Superconductivity,* vol. 28, no. 4, pp. 1-5, 2018.

[28] E. M. Gyorgy, R. Van Dover, K. Jackson, L. Schneemeyer, and J. V. Waszczak, "Anisotropic critical currents in $Ba_2YCu_3O_7$ analyzed using an extended Bean model," *Applied physics letters,* vol. 55, no. 3, pp. 283-285, 1989.

[29] D. Dimos, P. Chaudhari, J. Mannhart, and F. LeGoues, "Orientation Dependence of Grain-Boundary Critical Currents in $YBa_2Cu_3O_{7-\delta}$ Bicrystals," *Physical Review Letters,* vol. 61, no. 2, p. 219, 1988.

[30] M. Miura *et al.*, "Introduction of pinning center to enhance I_c under magnetic fields in REBCO coated conductors fabricated by advanced TFA-MOD process," *Physica C: Superconductivity,* vol. 468, no. 15-20, pp. 1643-1646, 2008.

[31] N. Chikumoto, S. Lee, K. Nakao, and K. Tanabe, "Development of inside-plume PLD process for the fabrication of large I_c (B) REBCO tapes," *Physica C: Superconductivity,* vol. 469, no. 15-20, pp. 1303-1306, 2009.

Table 4.1. Previous reports for improvement of pinning properties of GdBCO CCs via RCE-DR

Process	Procesing parameters	Substrate	$J_{c,sf}$ (MA/cm²) At 77K (magnetic J_c)	$J_{c,min}$ (MA/cm²) (magnetic $J_{c,B//c}$)		$F_{p,max}$ (GN/cm³) at 77 K	Ref.
				at 77K in 1 T	at 77K in 5 T		
Normal (Initial)	PO_2:30-150 mTorr Temp.:870-870℃	LMO/IBAD-MgO templates/**Hastelloy or SUS**	**3.7**	**0.3 (0.2)**			[25]
Compositi on control	PO_2:30-100 mTorr Temp.:870-870℃ 1:0.88:3.04 1:1.25:3.42 1:1.09:5.32	LMO/IBAD-MgO templates/**Hastelloy**	**1.5** **2.4** **3.2**	**~ 0.27** **~ 0.85** **~ 0.4**	- **0.08** -	**2.7 at 0.8T** **9.3 at 1.8T** **4.2 at 0.6T**	[14]
Growth Temp. Control	PO_2:30-150 mTorr 840 ℃ 860 ℃ 880 ℃	LMO/IBAD-MgO templates/SUS	**3.2** **2.9** **1.9**	**0.6** **0.36** **0.2**		**2.8 at 0.4T**	[15]
Irradiation	PO_2:30-150 mTorr Temp.:860-860℃ Pristine Proton dose 6×10^{16} cm^{-2}	LMO/IBAD-MgO templates/SUS	**(3.6, 2.2)**	**(0.25, 0.22)**		.	[13]
Post-annealing (300 mTorr)	PO_2:30-150 mTorr Temp.:870-870℃ Pristine 880 ℃, 5min	LMO/IBAD-MgO templates/**Hastelloy**	**3.7** -	**0.3 (0.2)** **0.5 (0.3)**		- **3.2 at 1T**	[11]
	PO_2:30-150 mTorr Temp.:860-860℃ Pristine 880 ℃, 5 min 880 ℃, 15 min 880 ℃, 30 min	LMO/IBAD-MgO templates/SUS	**(3.11, 2.27, 2.38, 2.02)**	**0.43, 0.36, 0.4, 0.33**	**0.029, 0.049, 0.059, 0.048**		[10]
	PO_2:30-150 mTorr Temp.:860-860℃ Pristine 750℃, 5min 500℃, 1h	LMO/IBAD-MgO templates/SUS		**0.43** **0.48** **0.37**	**0.024** **0.03** **0.04**		[12]
Doping	PO_2:30-150 mTorr Temp.:860-860℃ GdBCO Sm-doped GdBCO	LMO/IBAD-MgO templates/SUS	**4.16** **2.73**	**0.32** **0.41**	**0.019** **0.035**		[9]

Table 4.2. Summary of superconducting properties, in-plane & out-of-plane textures, and FWHN values of (003) reflections for our samples

Sample	$T_{c,zero}$ (K)	$J_{c,\ 77K,\ sf}$ (MA/cm²)	$J_{c,\ min}$ (MA/cm²)				In-plane texture ($\Delta\varphi$) (degree)	Out-of-plane texture ($\Delta\omega$) (degree)	FWHM values of (003) reflection (degree)
			77K, 1T	77K, 5T	65K, 3T	65K, 7T			
860-860C	93.8	4.15	0.326	0.025	0.366	0.126	3.27	1.45	0.293
850-860C	94.0	3.97	0.417	0.027	0.446	0.133	3.35	1.59	0.297
840-860C	94.0	3.79	0.431	0.035	0.456	0.154	3.44	2.05	0.312
830-860C	93.9	3.64	0.390	0.034	0.433	0.152	3.48	2.15	0.288
820-860C	93.5	2.86	0.383	0.033	0.414	0.151	3.55	2.26	0.245

Table 4.3. Summary of electrical properties, FWHM values of (003) reflections, average linear SF density, average particle size, and relative interfacial area ratio for the samples

Sample ID		**Transport $J_{c,sf}$** (MA/cm^2) **at 77K**	**Magnetic J_c** (MA/cm^2) for B//c								**FWHM** values of (003) reflections (degree)	**Average linear SF density** (10^6/cm)	**Gd_2O_3 average particle size (nm)**	**Relative Gd_2O_3 interfacial area ratio**
			77K				**65K**							
			0.01T	0.1T	1T	1.5T	0.01T	0.1T	1T	3T				
30-150 mTorr	860-860C	4.15	2.56	1.58	0.12	0.03	4.65	3.53	0.50	0.04	0.293	0.40 (± 0.05)	125±41	1.00
	840-860C	3.79	2.46	1.57	0.15	0.05	4.37	3.40	0.51	0.04	0.312	0.44 (± 0.04)	103±42	1.21
	820-860C	2.87	2.02	1.32	0.13	0.05	3.70	2.91	0.46	0.05	0.245	0.35 (± 0.06)	73±31	1.71
20-150 mTorr	860-860C	3.84	2.60	1.67	0.11	0.02	4.76	3.60	0.51	0.02	0.267	-	137±52	1.00
	840-860C	3.31	2.43	1.65	0.13	0.04	4.73	3.75	0.54	0.03	0.312	-	106±31	1.29
	820-860C	2.94	2.38	1.62	0.15	0.05	4.20	3.31	0.53	0.06	0.316	-	85±52	1.61
30-100 mTorr	850-850C	4.25	3.02	1.59	0.15	0.05	5.16	3.56	0.55	0.08	0.222	-	118±56	1.00
	830-850C	4.82	3.37	1.96	0.19	0.07	5.74	4.04	0.67	0.11	0.215	0.30 (± 0.04)	98±33	1.20
	820-850C	4.74	3.42	2.15	0.22	0.08	5.97	4.50	0.73	0.13	0.229	-	77±33	1.53

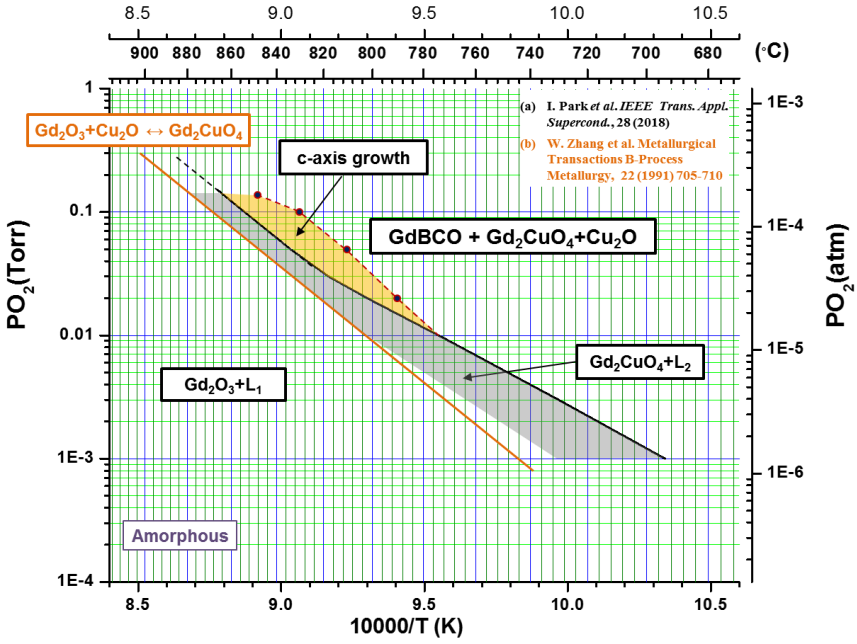

Fig 4. 1. The stability phase diagram of GdBCO for the nominal composition of Gd:Ba:Cu = 1:1:2.5 in low oxygen pressures from ref. [25] (yellow shadow: biaxially growth condition region)

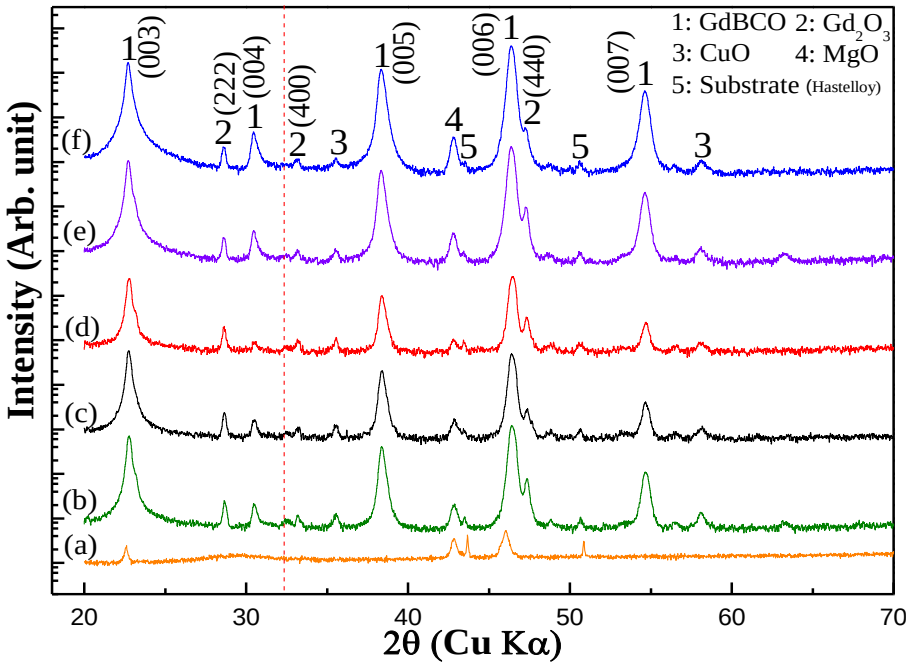

Fig. 4. 2. Theta-2theta (θ-2θ) scans of samples. (a) Amorphous precursor and GdBCO CCs samples grown at 860 ºC in 150 mTorr oxygen pressure with various growth temperatures of (b) 820, (c) 830, (d) 840, (e) 850, and (f) 860 ºC in 30 mTorr oxygen pressure.

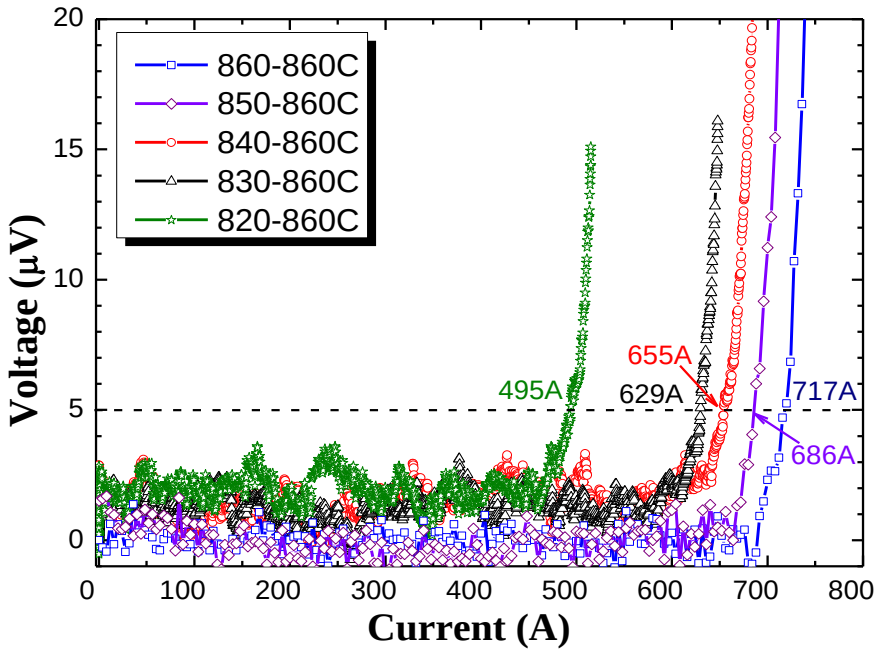

Fig. 4. 3. I-V curves of GdBCO CCs. Evaluated I_c values for the tape width of 12mm are indicated after fabrication process regime of 30-150 mTorr.

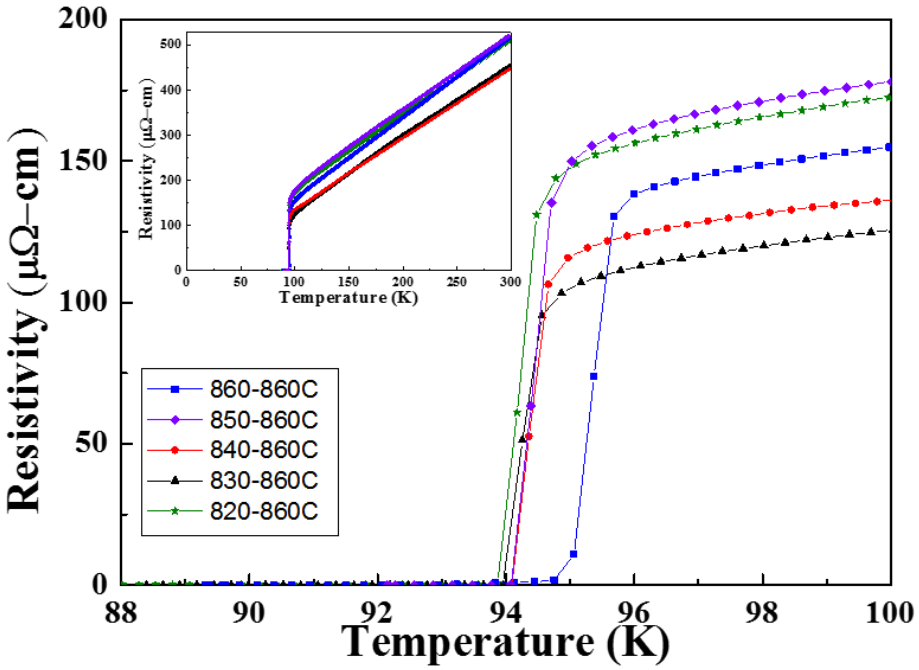

Fig. 4.4. Resistivity versus temperature for GdBCO CC after fabrication process regime of 30-150 mTorr.

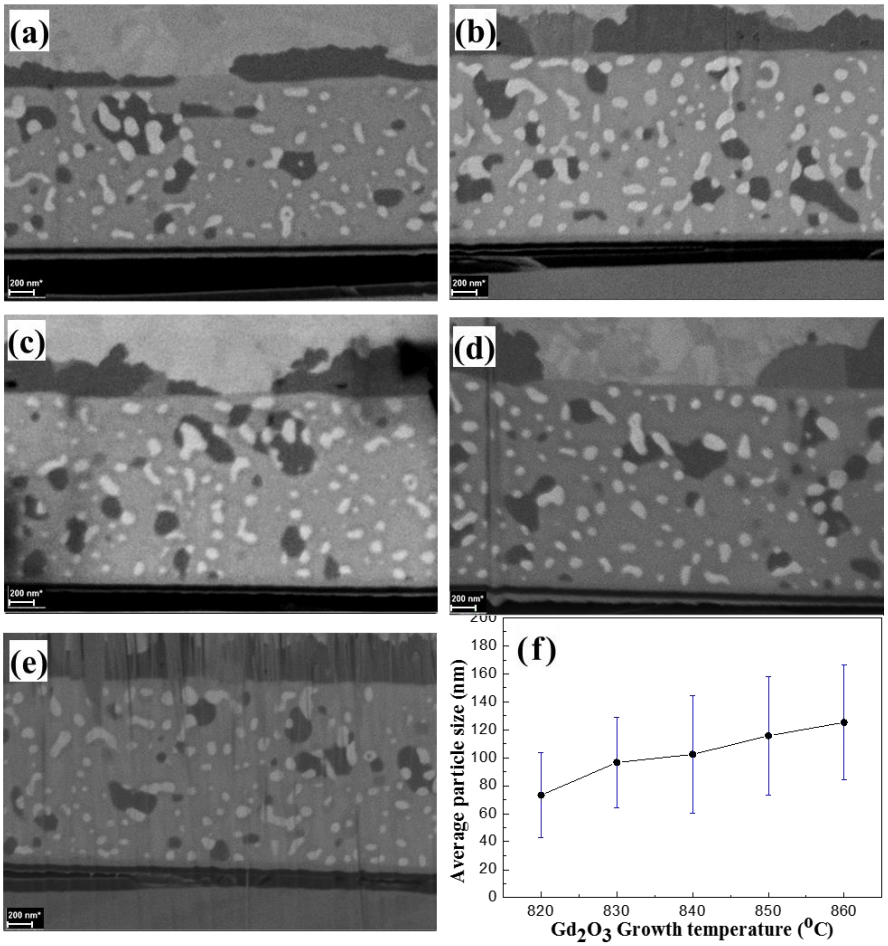

Fig. 4. 5. Cross-sectional FE-SEM micrographs of samples using BSE detector with Gd_2O_3 growth temperature at (a) 860, (b) 850, (c) 840, (d) 830, and (e) 820 ºC, and (f) the plot of Gd_2O_3 growth temperature versus average particle size

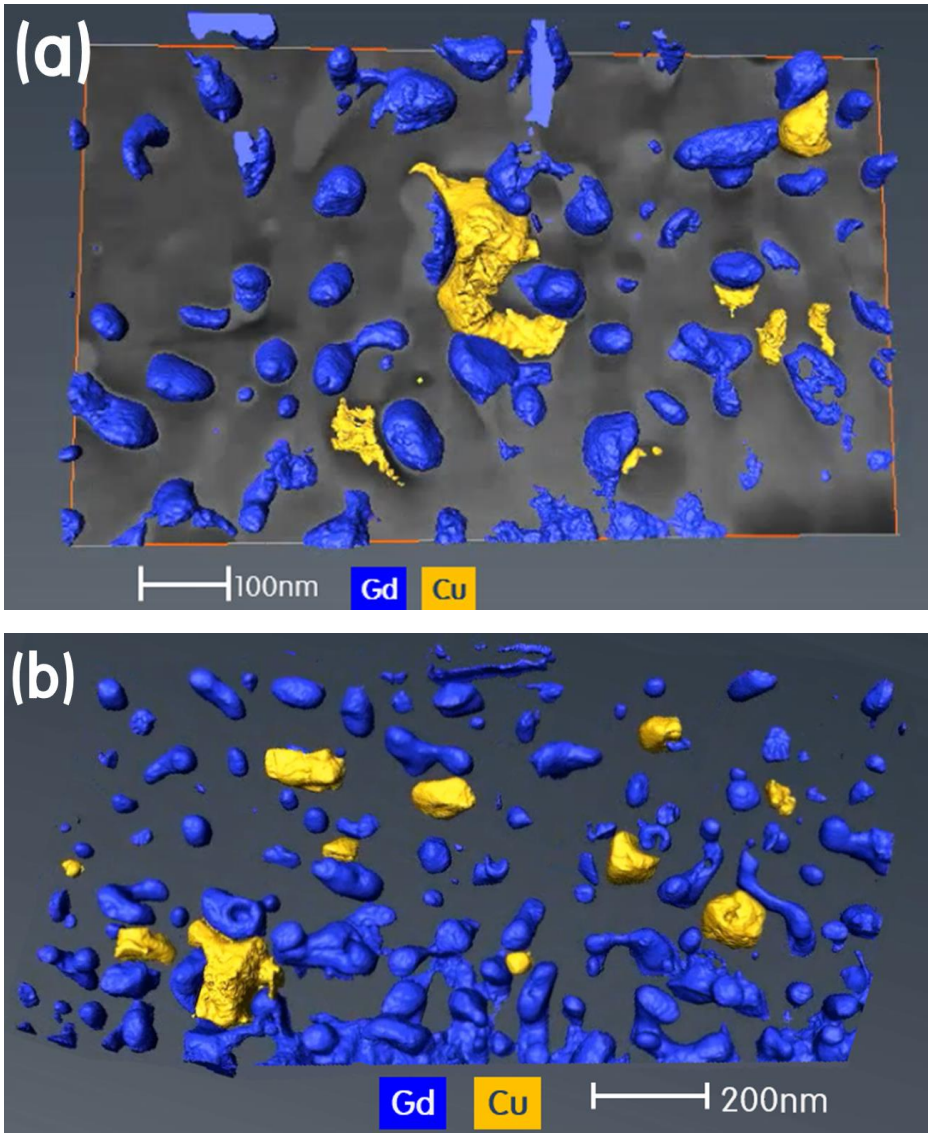

Fig. 4.6 volume rendered views of 3D reconstructed tomographic of the sample 820-860C the set of 30-150 mTorr

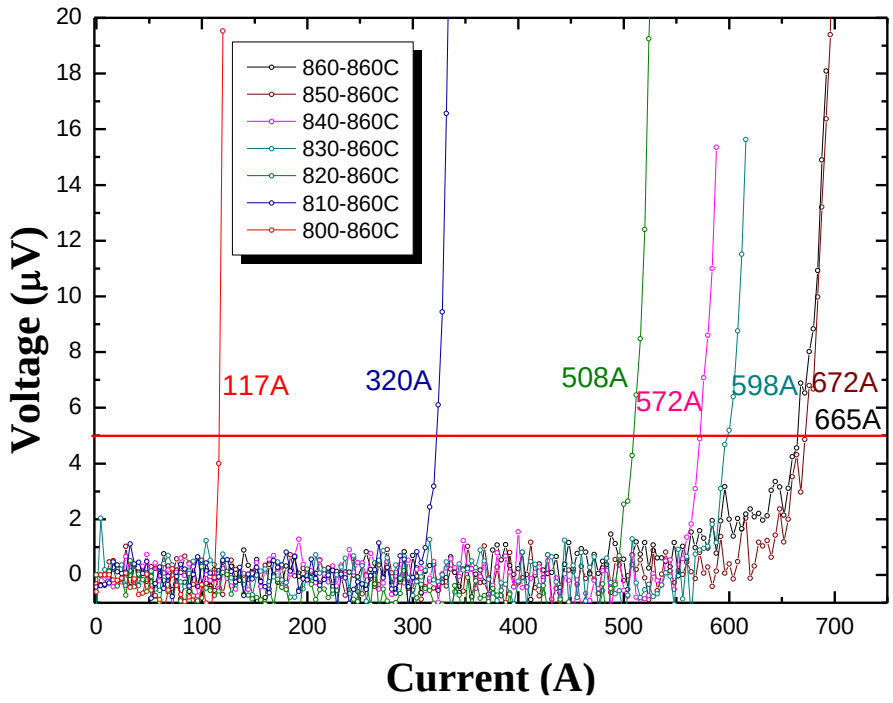

Fig. 4.7. I-V curves of GdBCO CCs. Evaluated I_c values for the tape width of 12mm are indicated after fabrication process regime of 20-150 mTorr

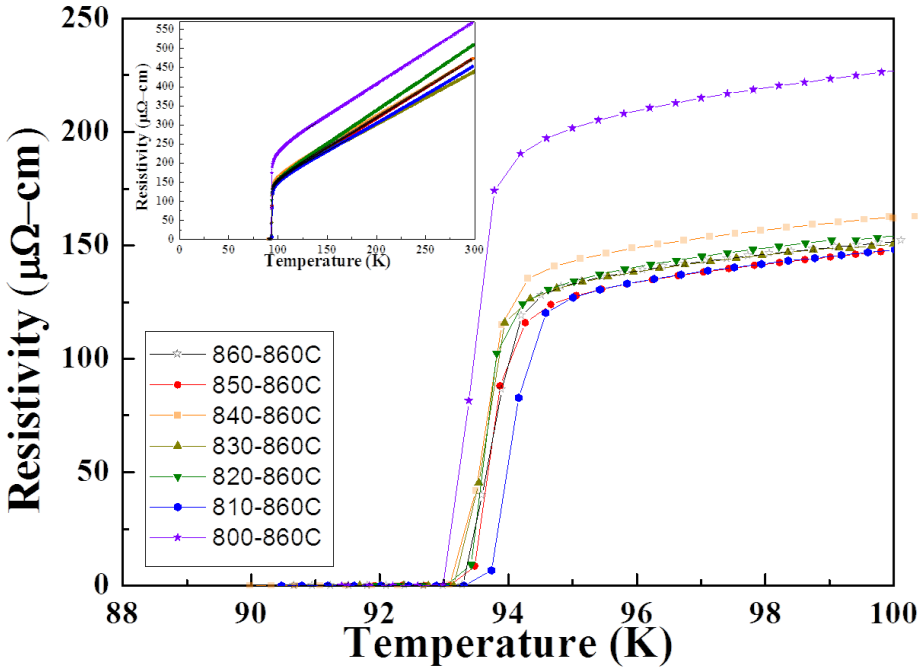

Fig. 4.8. Resistivity versus temperature for GdBCO CCs after fabrication process regime of 20-150 mTorr.

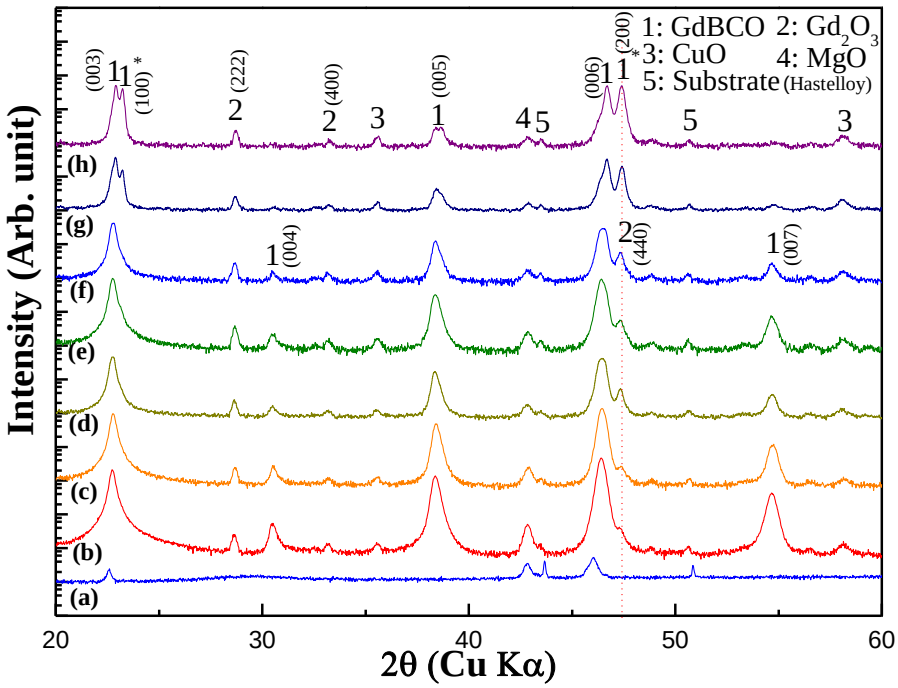

Fig. 4.9 Theta-2theta (θ-2θ) scans of samples. (a) Amorphous precursor and GdBCO CCs samples grown at 860 ºC in 150 mTorr oxygen pressure with various growth temperatures of (b) 860, (c) 850, (d) 840, (e) 830, (f) 820, (g) 810, and (h) 800 ºC in 20 mTorr oxygen pressure.

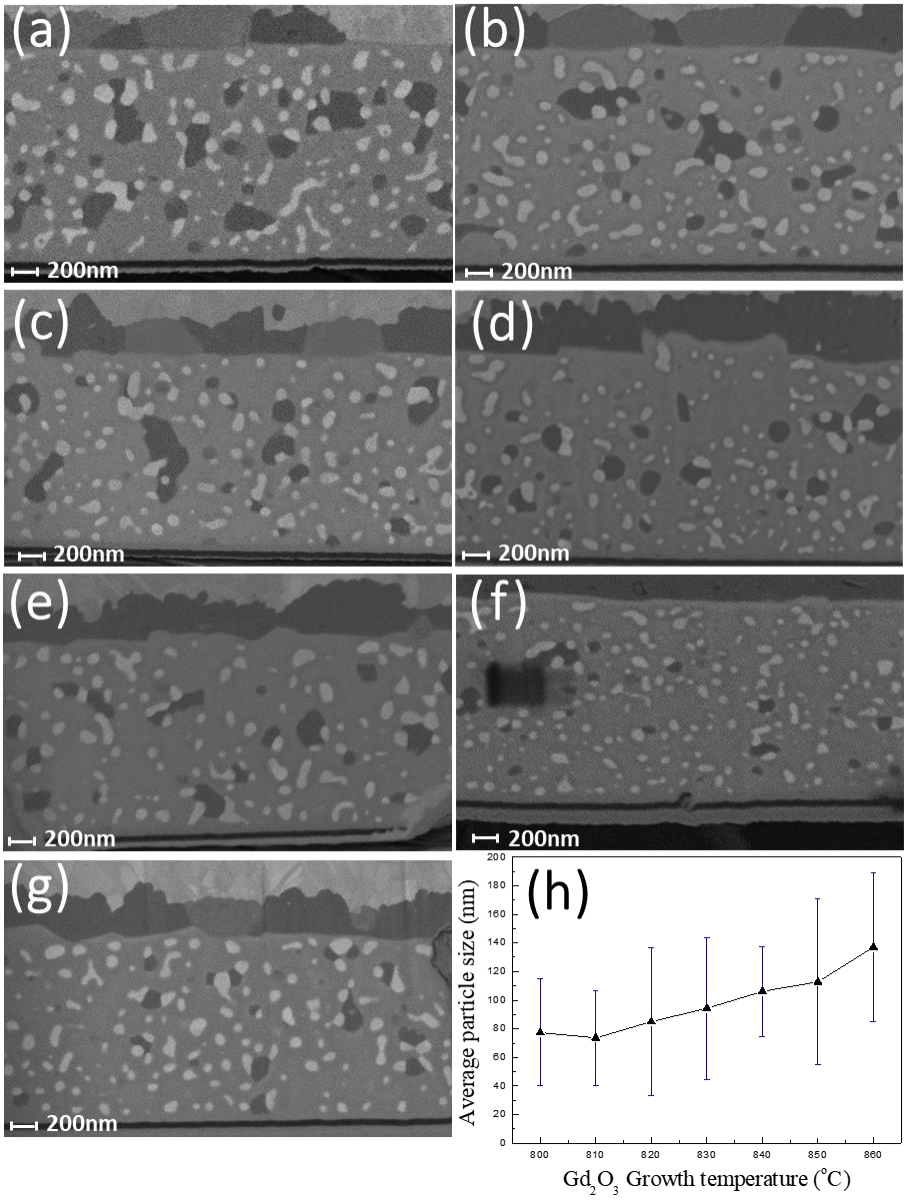

Fig. 4.10. Cross-sectional FE-SEM micrographs of samples using BSE detector with Gd_2O_3 growth temperature at (a) 860, (b) 850, (c) 840, (d) 830, (e) 820, (f) 810, and (g) 800 ºC, and (h) the plot of Gd_2O_3 growth temperature versus average particle size.

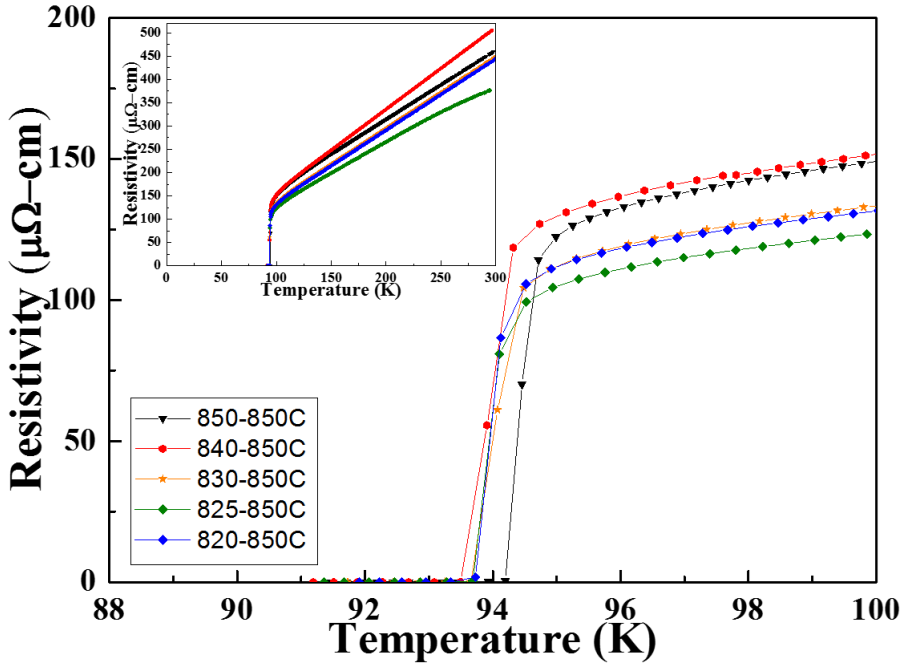

Fig. 4.11. Resistivity versus temperature for GdBCO CCs after fabrication process regime of 30-100 mTorr.

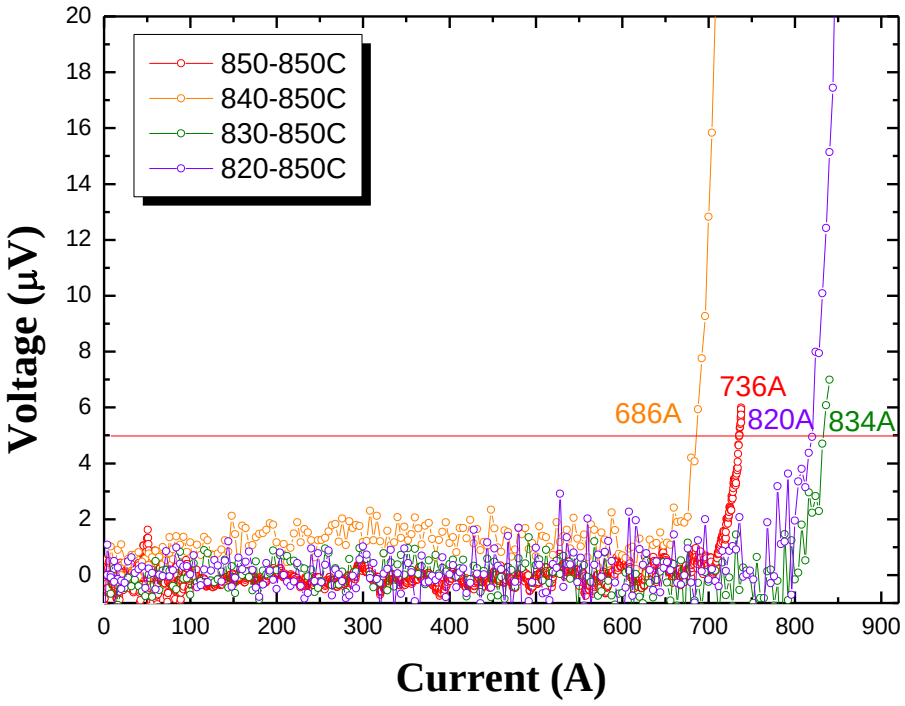

Fig. 4.12. I-V curves of GdBCO CCs. Evaluated Ic values for the tape width of 12mm are indicated after fabrication process regime of 30-100 mTorr.

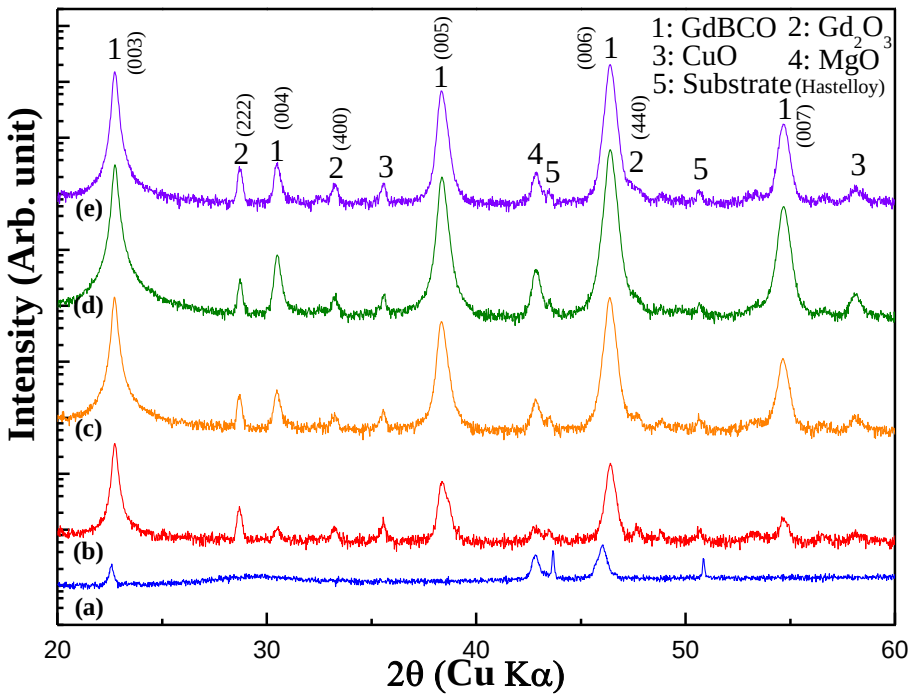

Fig. 4.13. Theta-2theta (θ-2θ) scans of samples. (a) Amorphous precursor and GdBCO CCs samples grown at 850 ºC in 100 mTorr oxygen pressure with various growth temperatures of (b) 850, (c) 840, (d) 830, and (e) 820 ºC in 30 mTorr oxygen pressure.

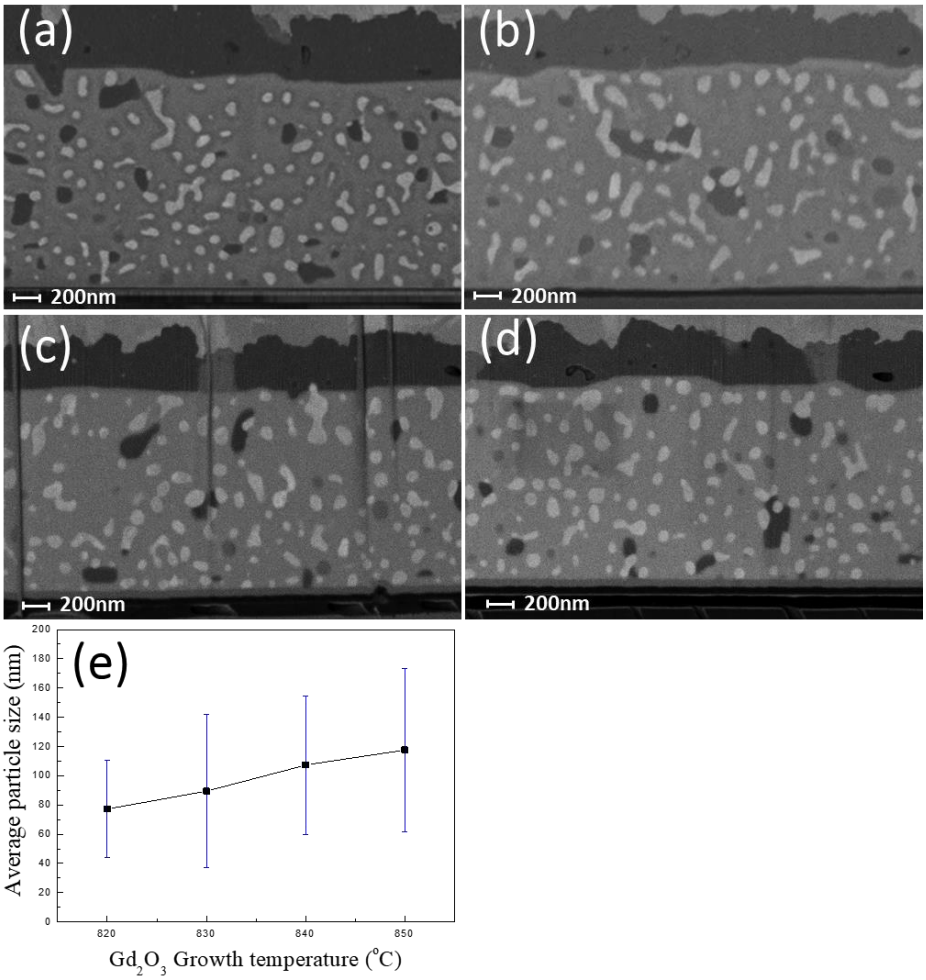

Fig. 4.14. Cross-sectional FE-SEM micrographs of samples using BSE detector with Gd_2O_3 growth temperature at (a) 850, (b) 840, (c) 830, and (d) 820 ºC, and (e) the plot of Gd_2O_3 growth temperature versus average particle size.

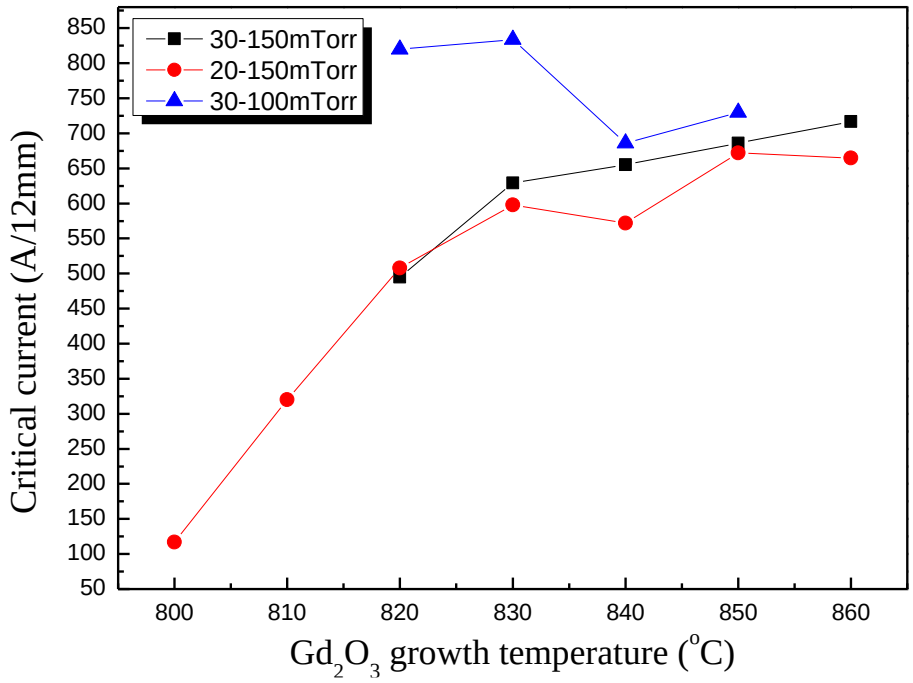

Fig. 4.15. self-field I_c values as a function of Gd_2O_3 growth temperature

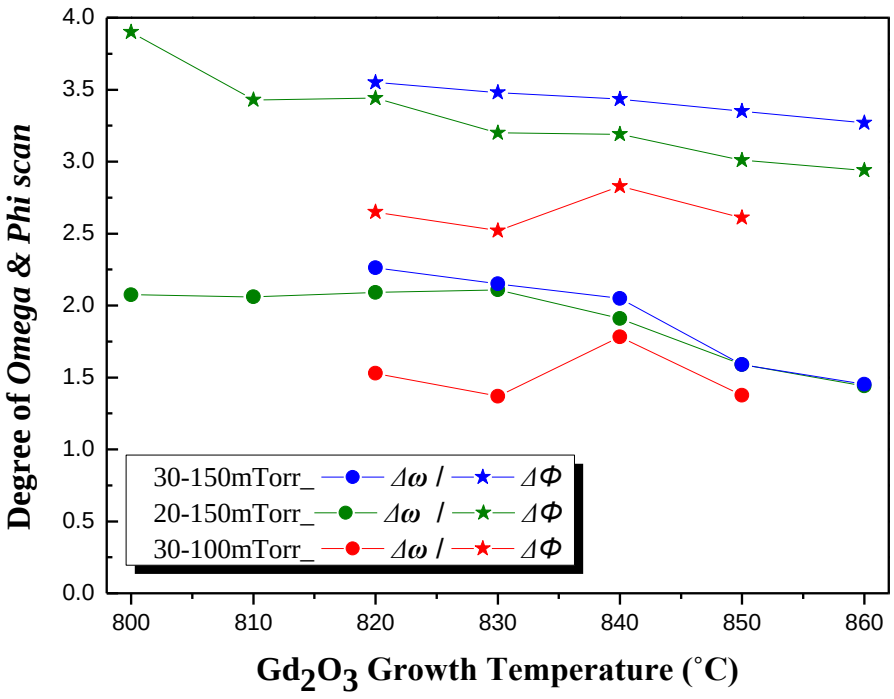

Fig. 4.16. In-plane texture (Δφ) and out-of-plane texture (Δω) of GdBCO CCs as a function of the Gd_2O_3 growth temperature.

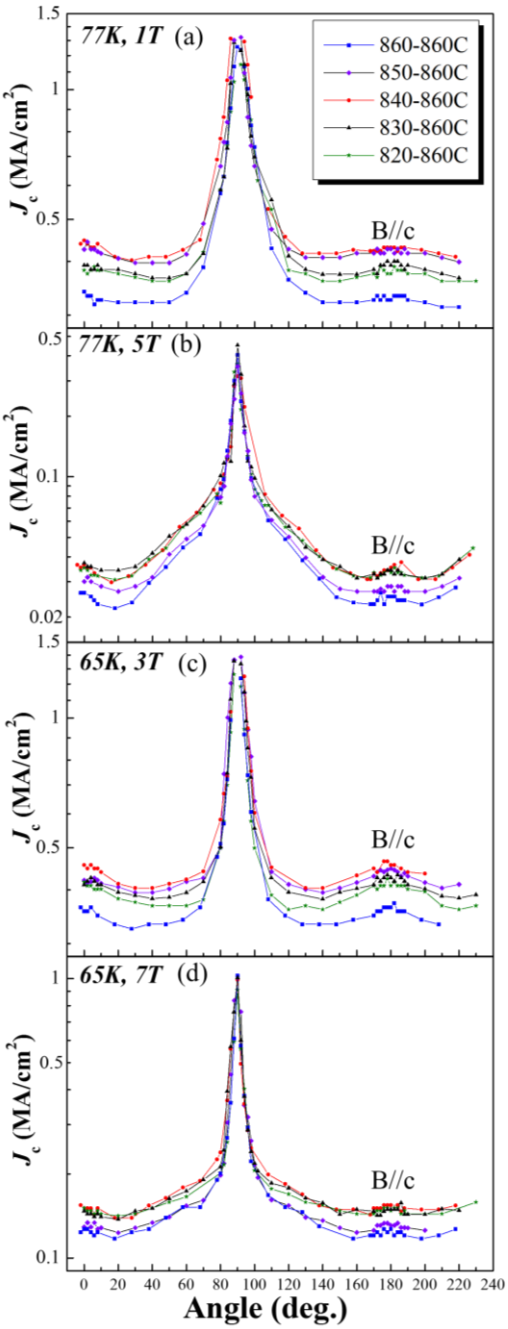

Fig. 4. 17. The angular dependency of in-field J_c values for GdBCO CCs samples at 77 K in (a) 1 and (b) 5 T, at 65 K in (c) 3 and (d) 7 T.

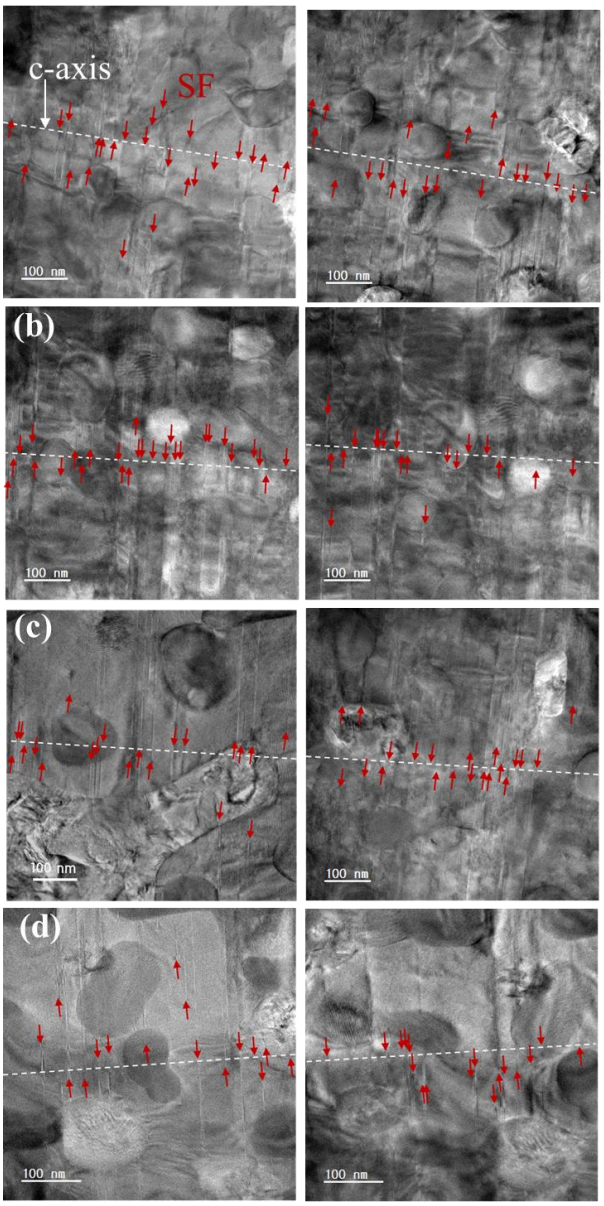

Fig. 4. 18. Cross-sectional TEM micrographs of sample 860-860C, 840-860C, 820-860C, and 830-850C are shown in (a), (b), (c) and (d), respectively. For each sample, two different parts were observed. The SFs and c-axis are indicated by red arrows and a white dotted line, respectively.

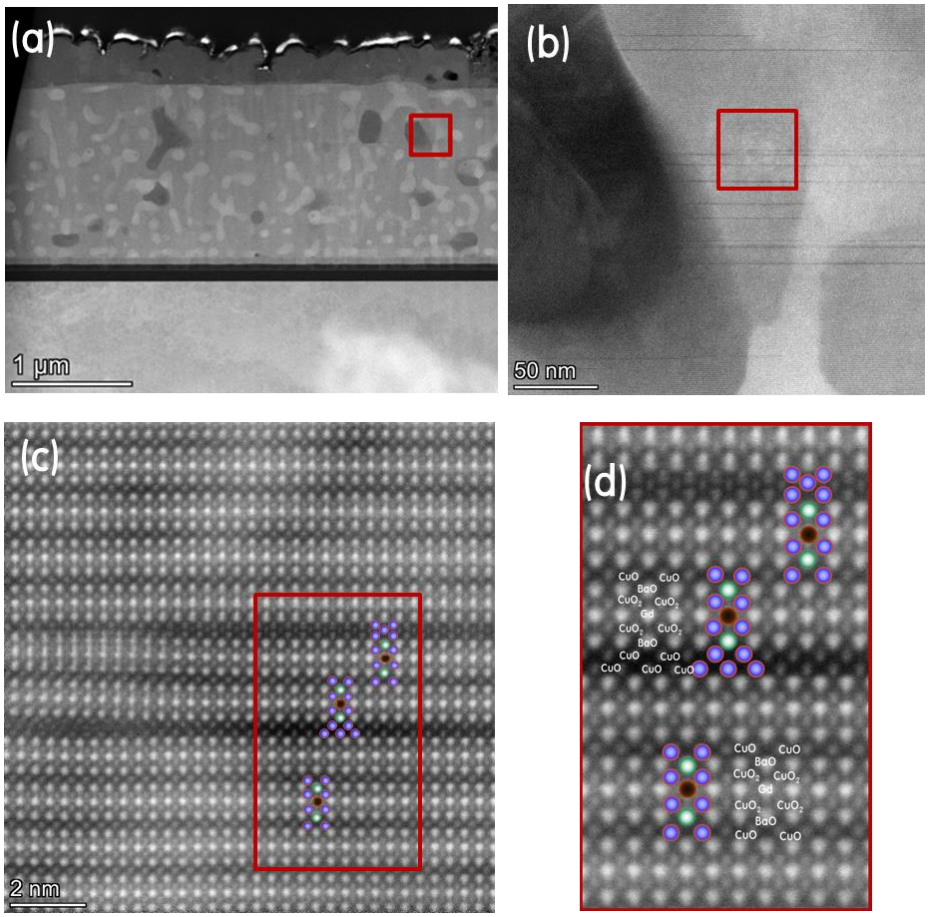

Fig. 4. 19. Cross-sectional TEM micrographs of sample 830-850C are shown in (a). (b), (c), and (d) are sequentially magnified HAADF micrographs of the red box area. The Gd, Ba, and Cu elements are indicated by black-, green-, and purple-colored symbols, respectively.

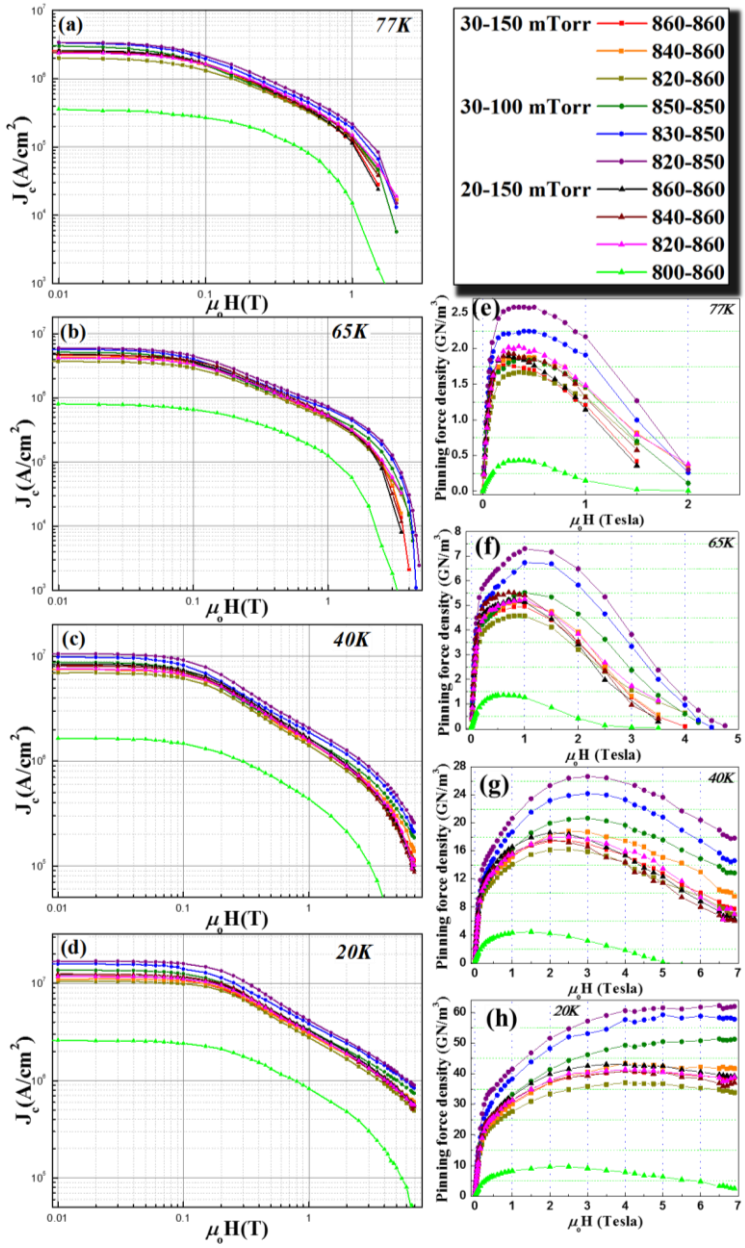

Fig. 4.20. Field dependence of magnetic J_c at (a) 77, (b) 65, (c) 40, and (d) 20 K for H//c, and the pinning force density ($F_p = J_c \times B$) values for B//c at (e) 77, (f) 65, (g) 40, (h) 20 K as a function of the magnetic field.

Chapter 5. Conclusion

In order to improve in-field J_c properties of GdBCO CC by the RCE-DR process, we conducted our research with a systematic approach as follows. First, the stability phase diagram of GdBCO was accurately constructed for the nominal composition of Gd: Ba: Cu = 1:1:2.5, Then, the growth conditions of c-axis aligned biaxially textured GdBCO film were investigated. Finally, on the basis of this information, the key processing parameters for the growth of both Gd_2O_3 particles and GdBCO film were selected to be controlled for the fabrication of a high-performance GdBCO CC by the RCE-DR process.

For the nominal composition of Gd:Ba:Cu = 1:1:2.5, which is normally used for the fabrication of GdBCO CC by RCE-DR, the GdBCO phase stability line, corresponding to the upper stability boundary of GdBCO, could be accurately determined by analyzing specimens which experienced a reeel-to-reel fast cooling after they were held at various high temperatures - PO_2 conditions. any different. Compared with the stability line of GdBCO for the nominal composition of Gd:Ba:Cu = 1:2:3, the GdBCO stability boundary is remarkably shifted to lower temperature region for this composition. Moreover, with decreasing temperature in a given PO_2, it is clear that GdBCO is formed by the following reactions of $Gd_2O_3 + L_1 \rightarrow Gd_2CuO_4 + L_2 \rightarrow GdBCO + Gd_2CuO_4 + Cu_2O$, which is also quite different from the peritectic recombination reaction of $Gd_2O_3 + L_1 \rightarrow GdBCO$ or $Gd163 + L_3 \rightarrow GdBCO$ for the nominal composition of Gd:Ba:Cu = 1:2:3. Considering this comprehensively, the

stability phase diagram for the nominal composition of Gd: Ba: Cu = 1:1:2.5 in the low oxygen pressures are carefully determined.

Next, since the c-axis aligned biaxially tetured GdBCO microstructure is essential for the fabrication of high-performance GdBCO CC, we tried to identify its growth conditions on the stability phase diagram of GdBCO previously constructed. As a result, the appropriate growth conditions are found to exist below the temperature of upper stability boundary at a given PO_2 and 774 ℃ (PO_2 = 10 mTorr), 789.5 ± 2.5 ℃ (PO_2 = 20 mTorr), 809.5 ± 2.5 ℃ (PO_2 = 50 mTorr), 831.5 ± 2.5 ℃ (PO_2 = 100 mTorr), and 848.5 ± 2.5 ℃ (PO_2 = 150 mTorr), respectively.

Finally, in order to improve the in-field J_c properties of GdBCO CC by RCE-DR, we tried to refine the Gd_2O_3 secondary-phase particles trapped in the GdBCO superconducting matrix. When the oxygen partial pressure decreased the growth temperature of Gd_2O_3 from 860 to 800 ℃ at 20 and 30 mTorr, the average particle size of Gd_2O_3 gradually decreased from a maximum of 137 ± 52 to a minimum of 73 ± 31 nm. As the average particle size of Gd_2O_3 was refined, the self-field J_c without an external magnetic field decreased sequentially, while the in-field $J_{c,min}$ value with an external magnetic field increased at first and then decreased again. In the magnetic J_c-B curves of the overall samples, samples prepared at various temperatures of oxygen partial pressure of 30 mTorr for Gd_2O_3 and 100 mTorr for GdBCO were overall higher than samples prepared under other conditions. The self-field J_c values were principally affected by in-plane and out-of-plane textures. Whereas in-field J_c values were snesative to the SF density and the average particle size of Gd_2O_3,

indicating that both the stacking fault and interfacial pinning are effective flux pinning sites. The highest performance GdBCO CCs were obtainable from the following: transport self-field J_c at 77K is 4.82 MA/cm^2 for the sample 830-850C of 30-100 mTorr, in-field J_c for B//c at 77K and 1T is 0.22 MA/cm^2, and $F_{p,max}$ is 2.6 GN/cm^3 at 77K and 0.4T for the sample 820-850C of 30-100 mTorr.

In conclusion, our sysetimatic approach to improve in-field J_c properties of GdBCO CC by the RCE-DR process turned out to be very useful, implying that the stability phase diagram of GdBCO and also the growth conditions of c-axis aligned biaxially textured GdBCO film, experimentally determed for the nominal composition of Gd: Ba: Cu = 1:1:2.5, are accurate. Although in-feld J_c properties of GdBCO CC could be significantly improved by refining Gd_2O_3 particles and also by varying the growth condition of GdBCO film in this study, the processing condition has not been fully optimized yet, and thus further improvement may be possible.

초 록

1987년 액체질소(77K) 보다 임계온도(T_c)가 높은 $YBa_2Cu_3O_{7-d}$ (YBCO)와 $REBa_2Cu_3O_{7-d}$ (REBCO, RE: 희토류 원소)가 발견된 이후 2세대 고온 초전도체(HTS)), CC(coated conductor)라고 불리는 REBCO 화합물은 많은 연구그룹에서 광범위하게 연구되었으며, 금속-유기 화학 기상 증착법(MOCVD), 펄스레이저 증착법(PLD), 금속-유기 증착법(MOD) 및 반응성 동시증발 증착법 (RCE-DR) 과 같은 다양한 REBCO 초전도 선재 제조공정이 성공적으로 개발되었다. 높은 통전 용량으로 인해 REBCO CC는 케이블, 한류기, 변압기, 초전도 자석 등과 같은 전력 응용기기에 적합한 것으로 알려져 있지만, 자장하에서의 더 높은 전류를 통전 시키는 고성능 고온초전도 선재를 위해서는 자장하에서의 임계전류 밀도(J_c)의 추가적인 향상이 필수적이다. REBCO CC 제조를 위해 개발된 공정 중에서 RCE-DR 공정은 높은 박막 성장률과 높은 생산량으로 인해 가장 비용적으로 효율적인 프로세스로 알려져 있다. RCE-DR 공정에 의해 제조 된 GdBCO CC의 자장하의 임계전류 밀도 특성은 다른 프로세스에 의해 제조된 REBCO CC의 특성보다 상대적으로 낮은 경향이 있기 때문에, 본 연구에서는 GdBCO의 상안정성 및 RCE-DR 공정으로 제조된 GdBCO CC의 고성능화에 대해서 연구하였다.

먼저, REBCO 박막은 낮은 산소 분위기에서 제조되기 때문에 낮은 산소 분압에서 REBCO의 상 안정성은 다양한 제조 방법에서 공정 매개 변수를 최적화하기 위한 기본 지침으로 중요한 역할을

합니다. RCE-DR 공정에서는 Gd : Ba : Cu = 1 : 1 : 2.5의 공칭 조성을 이용하기 때문에 RCE-DR 공정을 통해 고성능 GdBCO CC를 제조하기 위해서는 아직까지 보고되지않은 Gd : Ba : Cu = 1 : 1 : 2.5의 공칭 조성의 GdBCO의 상안정성을 정확하게 규명하는 것이 중요하다. GdBCO 화합물과 안정상의 위상 안정성은 1–150 mTorr의 낮은 산소 압력 (PO_2)에서 Gd : Ba : Cu = 1 : 1 : 2.5의 공칭 조성에 대해 연구되었다. 그 결과, Gd : Ba : Cu = 1 : 2 : 3의 공칭 조성에 비해, Gd : Ba : Cu = 1 : 1 : 2.5의 조성에 대한 GdBCO의 상경계가 낮은 온도 영역으로 이동하는 것으로 확인되었다. 또한, 주어진 산소 분압에서 온도가 증가함에 따라 Gd123, Gd_2CuO_4, Cu_2O의 3 상 평형이 GdBCO 상 경계보다 높은 온도에서 처음에는 Gd_2CuO_4와 액체 사이의 2 상 평형으로 바뀐 후, Gd_2O_3와 액체 사이의 2 상 평형으로 바뀌는 것을 발견하였다. 이를 토대로, Gd : Ba : Cu = 1 : 1 : 2.5의 조성에 대한 GdBCO의 상안정도를 정확히 규명할 수 있었다.

다음으로 규명된 Gd:Ba:Cu = 1:1:2.5의 조성에 대한 GdBCO 상안정도를 기반으로 10-150 mTorr의 산소분압영역에서 상경계 온도기준으로 undercooling 온도가 증가시키며 c-axis 정렬된 이축배향된 GdBCO의 성장영역을 조사하였으며, 이 영역은 50, 100 및 150 mTorr의 산소분압에서 약 20 ℃의 undercooling 온도임을 확인하였다. 또한, 10 mTorr 이하의 산소분압영역에서는 c-axis 와 a-axis 성장이 상경계 온도 바로 아래에서 함께 일어나기 때문에 이축배향된 GdBCO CC 제조가 10 mTorr 이하에서는 불가능하다. 결론적으로 RCE-DR공정으로 이축배향된 GdBCO CC 제조를 위해서는 GdBCO의 성장 조건을 규명된 상안정도에서 c-axis 성장

영역에 배치하여야만 한다.

끝으로, RCE-DR에 의해 제작된 GdBCO CC의 초전도 GdBCO 매트릭스는 일반적으로 평균 입자 크기가 ~120 nm인 다소 큰 Gd_2O_3 입자를 포함하고 있어, 이는 4 K에서 19T와 같은 높은 필드에서 임계전류 밀도 값을 감소시키는 원인이 될 수 있다. 이에 RCE-DR에 의해 GdBCO CC의 자장 하의 임계전류 밀도 특성을 향상하기 위해 GdBCO 초전도 매트릭스에 존재하는 Gd_2O_3 2차상 입자를 refine 하고자 했다.

이를 위해 GdBCO CC의 제조공정조건은 규명된 Gd:Ba:Cu = 1:1:2.5 조성의 GdBCO 상안정도 및 이축배향성을 갖는 GdBCO 성장 영역을 기반으로 신중하게 결정되었으며, GdBCO 초전도 매트릭스에 trap이 되는 Gd_2O_3 입자는 각각 100 및 150 mTorr 산소 분압에서 850 및 860 °C의 동일한 성장 조건에서 GdBCO 박막이 성장되기 전에 액상에서 Gd_2O_3의 핵 생성 및 성장 온도를 제어하여 refine 되었다. 산소 분압이 20 및 30 mTorr에서 Gd_2O_3의 성장 온도의 감소에 따라 Gd_2O_3의 평균 입자 크기는 최대 137 ± 52에서 최소 73 ± 31 nm로 점진적으로 감소했다. 30-150 mTorr 와 20-150 mTorr의 조건에서 GdBCO를 성장 시켰을 경우, Gd_2O_3의 평균 입자 크기를 refine하면 외부 자기장을 가해 주지 않는 self-field 임계전류 밀도가 Gd_2O_3의 성장온도에 따라 순차적으로 감소하였고, 30-100 mTorr의 조건에서는 다른 경향을 보였는데 이는 GdBCO matrix의 in-plain과 out-of-plain이 지배적으로 영향을 미치는 것으로 확인되었다.

전반적인 샘플들의 magnetic J_c-B curve를 볼 때, 성장 조건이 Gd_2O_3는 30 mTorr, GdBCO는 100 mTorr 의 산소 분압의 다양한

온도에서 제조한 샘플이 상대적으로 다른 조건에서 제조한 샘플들에 비해 전체적으로 높게 나왔으며, 자장하의 최소 임계전류 밀도 값의 변동은 주로 SF 밀도의 변화 뿐만아니라 Gd_2O_3의 성장 온도를 낮추면서 refine 된 Gd_2O_3 입자에 의한 interfacial pinning 또는 GdBCO subgrain의 입자 경계에 의한 pinning에 의한 영향으로 사료된다. 추가적으로 상대적으로 저자기장에서는 SF 밀도가 지배적이지만, 상대적으로 고자기장에서는 interfacial pinning이 지배적으로 pinning center 역할을 한다. 가장 높은 특성을 가지는 GdBCO 초전도 선재는 다음과 같이 특성을 나타내었다. 77K에서 self-field J_c값은 4.82 MA/cm^2, 자장하에서 J_c값은 77K, 1T, B//c에서 0.22 MA/cm^2, 그리고 최대 pinning force density ($F_{p,max}$) 값은 77K, 0.4T에서 2.6 GN/cm^{3}을 나타내었다.

주요어: $GdBa_2Cu_3O_{7-\delta}$ (REBCO) films, 상 안정성, 반응성 동시증발 증착법 (RCE-DR), 코팅 도체(coated conductors (CCs)), Gd_2O_3, 정제(refinement), 자속 고정점, 임계전류밀도 (J_c), 자속 고정 힘 밀도 (F_p)

학 번: 2015-20819